The Onset of Vaporization in ^{197}Au + ^{197}Au Collisions

by

Wen-Chien Hsi

A DISSERTATION

Submitted to

Michigan State University

in partial fulfillment of the requirements

for the degree of

DOCTOR OF PHILOSOPHY

Department of Physics and Astronomy

1995

ABSTRACT

The Onset of Vaporization in $^{197}Au + ^{197}Au$ Collisions

by

Wen Chien Hsi

Two bulk phase transitions exist in nuclear matter. At temperatures of the order of a few MeV up to a critical temperature of about 17 MeV, infinite neutral nuclear matter supports a mixed phase consisting of Fermi liquid droplets in coexistence with a nucleonic gas. At significantly higher temperatures of the order of 150 MeV, calculations within the standard model predict a deconfinement phase transition from hadronic matter to a quark-gluon plasma.

One of the four major current thrusts in nuclear physics is the extraction of information about these basic phase transitions from nuclear collisions. Temperatures and densities relevant to the liquid gas phase transition can be momentarily attained in nuclear collisions at incident energies of E/A = 35 - 400 MeV. To search for the liquid-gas phase transition in a large system where signals of phase transitions are expected to be sharper, multifragment disintegrations in $^{197}Au + ^{197}Au$ collisions were investigated in this dissertation at incident energies of E/A = 100, 250 and 400 MeV. These measurements clearly indicate that the yields of intermediate mass fragments (IMF's; $3 \leq Z \leq 30$) decrease significantly with the incident energy in central collisions, consistent with the onset of nuclear vaporization.

These measurements were performed with an experimental array of considerable complexity, capable of providing considerable information about the dynamics of the collision. Measurements performed in this dissertation indicate the presence of a collective radial flow for central collisions that contain of the order of a third to a half of

the total incident kinetic energy, thereby decreasing the energy available for thermal excitation. Measurements of the kinetic energy spectra also provide information about the mechanisms of energy deposition in peripheral collisions. Both fragment yields and energy spectra were compared to molecular dynamics calculations developed to predict these observations. These comparisons reveal significant shortcomings in these dynamical models.

ACKNOWLEDGMENTS

I would like to express my thanks to my advisor, Professor William Lynch, for his invaluable supervision over my research. His ability to cut to the core of a problem has made my work fruitful and enlightening. His advise at each time step of my research period has been always critical and appropriate. Betty Tsang, Graham Peaslee, Thomas Glasmacher and Korand Gelbke have given their friendship as well as invaluable instructing during the data analysis of my thesis. Professor Betty Tsang has especially contributed a lot to this thesis during the data analysis and revising my thesis, as well as sitting on my guidance committee. S.D. Mahanti, Scatt Pratt, Wayne Repko and Michael Thoennessen gave a careful reading of this work and also served on my guidance committee.

When I began my education in experimental nuclear physics, Dave Bowman, Graham Peaslee and Remualdo de Souza took the time to share their knowledge with me. It was very pleasant to work with Dr. Graham Peaslee. I greatly appreciate his help and suggestions on preparing the two experiments performed in Europe, and the fruitful discussions in the following data analysis. I also have greatly benefited from Dr Dave Bowman and Dr Remualdo de Souza teaching me about data acquisition and experimental skills. I also appreciated the friendship and the contributions from Thomas Glasmacher, Carlos Montoya, Carsten Schwarz and Betty Tsang during the data analysis, I would like to thank G. Peilert and W.A. Frideman for their valuable simulations of the IMF emissions.

My fellow graduate students have offered much support. I appreciate the help from Mike Lisa during my thesis experiment at GSI, Germany. I also had many valuable discussions with Larry Phair about techniques applied in data analysis. The other graduate students in my research our group have helped me very much. Mei-Jui Haung, Yeongduk Kim, Fan Zhu, Damian Handzy, James Dinius and Cornelius Willams have shared their knowledge and friendship with me, making my work much easier than it would have been without them. I would also like to acknowledge Esawar Ramakrishnan

for the enjoyable experience of studying nuclear physics with him during the summer school of 1993. Afshin Azhari, Shigeru Yokoyama, John Kelly, Eugener Gualtiteri and others have also helped to make my experience enjoyable and instructive.

It has been a great pleasure working with the excellent NSCL staff. Jack Ottarson was extremely helpful for the upgraded Miniball/Miniwall design. John Yurkon, Dennies Swan and Jim Vincent have solved countless hardware related problems in upgrading the Miniball/Miniwall project. I also appreciate our machine shop for doing all the manufacturing required for the upgraded project. I am also thankful for other people not mentioned here who have helped me.

I sincerely thank my family in Taiwan, R.O.C.; my parents, bothers and sisters for their encouragement and support. I also thank my in-laws in Chicago for sharing happiness and helping to build my self-confidence to live in a new environment. Finally, I am indebted to my wife, Li Yung, for her love and patience during my graduate studies. I appreciate my daughter Jane for bringing more joy and happiness to my family.

Table of Contents

List of Tables

List of Figures

Chapter 1

Introduction

1.1 Overview

The nucleon-nucleon interaction is strongly repulsive at distances less than 0.4 fm, attractive at distances of about 1 fm, and vanishes exponentially at larger distances. While the distance scales of the nucleon-nucleon interaction are considerably smaller than those of molecular interactions, these characteristics, short-range repulsion and mid-range attraction, are also found in the molecular Lennard-Jones potential [Lenn 31, Slat 75]. Thus it comes as no surprise that infinite nuclear matter exhibits a liquid-gas phase transition.

Infinite nuclear matter is a theoretical construct that finds its closest physical realization within a neutron star. Nearly all experimental constraints upon the properties of nuclear matter, however, have been derived from experimental measurements of binding energies [Waps 77, Myer 82], radii [Vrie 87] and compressibilities [Siem 79], etc. of finite nuclei. Temperatures and densities relevant to the liquid-gas phase transition can be attained momentarily in central nucleus-nucleus collisions at energies of E/A = 35-400 MeV. The investigation of such collisions offers the best opportunities for experimentally determining the properties of this bulk phase transition.

Within the region of liquid-gas coexistence, thermodynamical properties of nuclear matter are strongly reflected in the relative abundance of fragments [Lync 87]; therefore, the study of fragment observables in multifragment disintegrations is essential to investigations of the liquid-gas phase transition. Initial investigations of fragment observables consisted of inclusive measurements [Finn 82, Hirs 84, Buaj 85, Cser 86, Lync 87, Troc 89] and were unable to address many of the important issues. Since the latter part of the last decade, a number of new multifragment detection arrays that are capable of exclusive measurements have come into operation [Bade 82, West 85, deSo 90, Gobb 93], and the information about multifragmentation has grown enormously [Boug 87,

Doss 87, Boug 89, Blum 91, deSo 91, Kim 89, Bowm 91, Phai 93, Sang 92, Alar 92, Ogil 91, Hube 92].

This dissertation work began at a stage of great discovery in this field. Measurements [Boug 87, Doss 87] immediately prior to those discussed here had shown for the first time that multifragmentation was feasible for central collisions of heavy ions at intermediate energies [deSo 91, Kim 89, Bowm 91, Phai 93] and for peripheral collisions at considerably higher energies [Ogil 91, Hube 92]. It became a high priority to determine the range of experimental conditions for which this new phenomenon was manifested. Excitation functions for the Kr + Au [Peas 94] and Au + Au [Tsan 93] systems were initiated spanning a wide range of incident energies and requiring experiments at three different facilities for their completion. This dissertation work consists of studies of Au + Au collisions performed at E/A = 100, 250, and 400 MeV using heavy ion (Schwerionen) Synchrotron (SIS) facility of the Gesellschaft für Schwerionenforschung (GSI) at Darmstadt Germany.

1.2 Theoretical Models for Multifragmentation

As many of the experimental observations place significant constraints upon theoretical interpretations of multifragmentation, it is relevant to provide some brief descriptions of current theoretical models [Frie 90, Peil 92, Baue 85, Dani 88, Stöc 86] of this phenomenon. These models can be categorized in a variety of ways. Here, we choose two broad categories: 1) dynamical models that follow the non-equilibrium transport of energy, mass and momentum throughout the nuclear collision, and 2) statistical models which calculate the probabilities of various experimental observations using some form of statistical weight.

Dynamical models

While considerable effort is being directed towards the development of quantum transport theory, the description of fluctuations leading to fragment production is an unsolved problem. Here we only describe some of the presently used approximate

techniques. For the description of phenomena less sensitive to fluctuations at incident energies of E/A ≥ 20 MeV, considerable success has been achieved in descriptions based upon the Boltzmann Uehling Uhlenbeck (BUU) equation [Nord 28, Uehl 33] which describes the time evolution of the Wigner transform of single particle density matrix $f(\vec{r}, \vec{p}.t)$ as follows:

$$\frac{\partial f}{\partial t} + \frac{\vec{p}}{m} \cdot \frac{\partial f}{\partial \vec{r}} - \nabla U \frac{\partial f}{\partial \vec{p}} = I \tag{1.1}$$

$$= \int \frac{d^3\vec{p}' d^3\vec{p}_1 d^3\vec{p}_1'}{(2\pi)^6} \cdot \sigma |\vec{v} - \vec{v}_1| [f_1' f' (1-f_1')(1-f') - f_1 f (1-f_1)(1-f)] \delta(\vec{p} + \vec{p}_1 - \vec{p}' - \vec{p}_1')$$

Here, U is the nuclear mean field potential which may depend upon both the position $\vec{r}$ and momentum $\vec{p}$ of the particle. For momentum independent potentials, local Skyrme interactions with two- and three-body components are commonly used. The right-side collision integral of a binary collision depends upon the relative velocity $\vec{v} - \vec{v}_1$ between the two nucleons, and includes a cross section σ for nucleon-nucleon scattering via the residual interaction (which may differ from the corresponding free space value), as well as the occupancy and Pauli blocking factors, f and (1-f), respectively.

To solve the VUU/BUU equation, nucleons are represented as a sum of point-like test particles

$$f(\vec{r}_i, \vec{p}_i, t) = \sum_{i=1}^{\tilde{N},A} \delta(\vec{r}_i - \vec{r}_{i0}) \delta(\vec{p}_i - \vec{p}_{i0}), \tag{1.2}$$

where A is the number of nucleons and $\tilde{N}$ is the number of test particles per nucleon. Each test particle is propagated throughout the nucleus-nucleus collision using Hamilton's equations of motion [Mari 70]. Solutions of Eq. 1.1 provide a description of the time dependence of the single particle phase space density [Huan 63]. While fluctuations may be produced by collisions described by the R.H.S. of Eq. 1.1 in some simulations and may result in the production of some fragments, such fluctuations only reflect numerical instabilities which should be negligible for accurate solutions of Eq. 1.1. Efforts at extending Eq. 1.1 to higher order in the BBGKY hierarchy [Bogo 62] by including an additional fluctuating collision integral I on the R.H.S. of Eq. 1.1 [Dane 91, Batk 92] are

still in their infancy. Thus Eq. 1.1 is mainly used to establish initial conditions such as the excitation energy, density or collective expansion velocity. It cannot describe fragment production.

Because the time evolution of the density matrix approaches that of a classical A-body system at high temperature, molecular dynamics has been used to describe A-body fluctuations and correlations during nuclear collisions [Peil 92, Aich 88]. Some difficulties occur due to the explicit lack of quantum mechanical effects, such as the Pauli exclusion principle in such models [Boal 88]. In an attempt to address such limitations, some models represent each nucleon by a Gaussian "wave packet". In the Quantum Molecular Dynamics (QMD) model of ref. [Peil 89 & 92], this takes the form

$$f_i(\vec{r},\vec{p},t) = [\frac{1}{\pi\hbar}]^3 e^{-[\vec{p}-\vec{p}_{0i}(t)]^2 L^2/\hbar^2} e^{-[\vec{r}-\vec{r}_{0i}(t)]^2/L^2} \tag{1.3}$$

where the $\vec{p}_{0i}$ and $\vec{r}_{0i}$ are the centroids of wave packet of the i^{th} particles and L is a width parameter of the wave packet. A Pauli potential, which acts as a repulsive potential in phase space, is used to simulate the Pauli exclusion principle [Dors 88].

$$U_{Pau} = \frac{1}{2} V_{Pau}^0 \left[\frac{\hbar}{q_0 p_0}\right]^2 \exp\left\{-\frac{r_{ij}^2}{2q_0^2} - \frac{p_{ij}^2}{2p_0^2}\right\} \delta_{\tau_i\tau_j}\delta_{\sigma_i\sigma_j} \tag{1.4}$$

Here the σ_i and τ_i are the third components of the spin and isospin of nucleon i. The inclusion of a Pauli potential in such molecular dynamics approaches allows for well-defined fermionic ground states [Peil 92] and thereby permits accurate estimation of the excitation energies of the emitted fragments. The nuclear system is then described by a Hamiltonian of the form:

$$H_{tot}^{FG} = \sum_i \frac{p_i^2}{2m} + U_{pau} + U_0 \tag{1.5}$$

where U_0 is a potential which may include two- and three-body Skyrme potentials as well as Coulomb, Yukawa and symmetry potential related terms. The time evolution of the system is obtained by solution of Hamilton's equations. A similar approach is also taken within the Quasi-Particle Dynamics (QPD) model of ref. [Boal 88 a&b].

Promising approaches, such as Femion Molecular Dynamics [Feld 90] and Antisymmetrized Molecular Dynamics [Hori 91, Bauh 85] are now being developed which like time-dependent Hartree-Fock, and satisfy the Pauli principle by considering the time evolution of Slater determinant wave functions. Unfortunately, calculations of systems containing of the order of 400 nucleons are not currently feasible in these approaches and therefore will not be considered further in this dissertation.

Statistical Models

In a nuclear collisions after the initial pre-equilibrium cascade, one is frequently left with large highly excited fragments and reaction residues. In a complete dynamics theory, the decay of these residues should be adequately described, but might require inordinate amounts of computer time. Presently, none of the available dynamics models can reproduce the decay rates predicted by statistical models. In the case of the BUU equation, this is understandable as the fluctuations relevant to cluster production are not included in the theory. In the case of the QMD and QPD molecular dynamics models, the inclusion of the Pauli potential does not alter the fact that specific heats of the systems described by these calculations are essentially classical and therefore exceed the specific heat of an equivalent quantum mechanical system composed of Fermions [Bere 92]. Thus, for fixed total excitation energy, the kinetic energy per degree of freedom is less for these molecular dynamics models than for real nuclear systems and consequently, fragments do not so frequently surmount the Coulomb barrier.

There is, therefore, a need for a better description of the longer time scale decays of excited fragments and heavy residues. A variety of statistical fragmentation models have been developed. One may classify such models according to whether the final states result from the solution of a statistical rate equation, as is the case of the Hauser-Feshbach [Mekj 77, Gran 86, Boal 83] or fission [Morr 78, More 75] theories of the compound nucleus, or by assuming static equilibrium of the fragmenting system. Models which assume static equilibrium can be further distinguished as to whether the statistical weights are calculated according to phase space assumptions, as in the case of multiparticle phase space models [Gros 82, Bond 85, Fai 82] and liquid-gas equilibrium models [Frie 83, Cser 86, Lync 87],

or from purely geometric considerations, as in the case of site or bond percolation theory [Baur 85]. In this dissertation, two of these statistical models were used [Tsan 93]; the Expanding Evaporating Source (EES) model of Ref. [Frie 90] and the Statistical Multifragmentation Model (SMM) of Ref. [Bond 85 a&b] and [Botv 87]; these will be described in the following.

The SMM model [Botv 87] has the advantage of being an efficient Monte Carlo event generator that produces multifragment final states with statistical weights that are similar to the weights incorporated in the Copenhagen [Bond 85 a&b] or Berlin [Gros 90] multiparticle phase space models. All three approaches have the central goal of producing a set of possible multifragment final states that conserve the total energy, momentum, particle number, and charge. The relative probability of each specific decay configuration is assumed to be proportional to its corresponding phase space volume. When the predictions of these models are calculated solely as a function of the excitation energy, there are some differences in the assumed freeze out configurations. In the original approach of the Copenhagen model, for example, the density of the breakup configuration is allowed to vary with excitation energy [Bond 85 a&b], while in the SMM approach, the density is held fixed at $\rho_o/6$ [Botv 90, Bond 94], similar to the philosophy of the Berlin multifragmentation model [Gros 90].

In addition to the phase space corresponding to the transitional motion of the various particles, the internal phase space of the excited nuclear fragments is calculated via empirical level density formulae [Myer 82]. The multiparticle phase space is sampled in the SMM model by an algorithm described in ref. [Rand 81, Bond 82] and a breakup configuration, consisting of free nucleons plus stable and excited fragments, is Monte Carlo chosen for each event. These excited fragments are then allowed to decay until all fragments are particle stable.

The underlying assumptions of such multiparticle phase space models are: 1) that local equilibrium is maintained during the expansion of the system until a very low freeze-out density is reached, and 2) that the breakup is sufficiently rapid that the system can not globally re-equilibrate between decays. The first assumption is problematic and its validity has yet to be adequately tested; the neglect of nuclear interactions between the various

particles at freeze-out in these models has the consequence that none of them can be used to explore critical phenomena. The validity of the second timescale assumption about multifragment decays can be clearly tested via measurements of fragment-fragment correlation functions [Kim 92]. It is clear that there are cases where this assumption is invalid, e.g., at low excitation energies where compound nuclei have been extensively studied [Fox 93]. There, hot nuclei decay sequentially, emitting one particle after another, a process that has been successfully described by statistical rate equation approaches like the Weisskopf or Hauser-Feshbach theories [Weis 37].

The Weisskopf and Hauser-Feshbach compound nuclear rate equation techniques have been generalized to describe the emission of complex fragments from hot nuclei [Frie 83]. The basic rates incorporated in such models may be trivially calculated by assuming a detailed balance between the emission of a particular particle species and its hypothetical re-absorption which would occur if the hot nucleus was in thermal equilibrium with hot gas of the emitted species in which it was embedded [Frie 89]. Hot and highly charged nuclei are not hydrodynamically stable at temperatures in excess of 5 MeV, however. Therefore, in the EES model of ref. Frie 90, simultaneous expansion and fragment emission are considered.

These statistical models have been tested in a variety of contexts. Both multiparticle phase space models, such as the SMM and the evaporative EES model, predict a rapid rise in the fragment multiplicities when the systems expand to sub-nuclear densities [Frei 90]. In the case of the SMM model, calculations display the rapid onset of multifragmentation as the temperature of the system rises above 5-6 MeV; this rise is attributed to the onset of a "cracking" phase transition [Boal 85b, Bovt 90]. A rapid rise in fragment multiplicities and fragmentation at temperatures of about 5 MeV is also predicted by the EES model when the system expands to a density less that $0.4\rho_o$ [Frie 90]. The occurrence of this common feature in both models is a reflection of the underlying thermodynamic instability of a homogeneous thermally excited system at a sub-nuclear density which gives rise to the liquid-gas phase transition [Siem 83]. There are detailed differences between the predictions of these models that are most pronounced

when the predicted energies, momenta and correlations of emitted fragments for the various models are compared [Bowm 93].

1.3 Experimental Status Prior to the Dissertation Measurement

Multifragment emission has now been explored in a variety of nuclear systems [deSo 93, Phai 93, Tsan 93, Peal 94]. Large fragment multiplicities are observed in central collisions of complex nuclei which exceed the predictions of statistical compound nuclear decay at normal density. The multiplicities, however, may be described by SMM and EES models which assume the disintegration occurs at subnormal density. The fragment multiplicities also exceed those predicted by the molecular dynamics models.

Estimates of the time scales for fragmentation in $^{36}Ar + ^{197}Au$ collisions [Fox 93], Kr + Au collisions [Baug 93], $^{197}Au + ^{197}Au$ collisions [Kämp 93], and $^{129}Xe + ^{197}Au$ collisions [Bowm 93], have been obtained by analyzing the Coulomb final state interactions between fragments. These extracted timescale decrease with incident energy. Time scales less than 100 fm/c = 3.3×10^{-22} seconds are typically observed in such experiments, consistent with a bulk disintegration and much less than the time required for the system to decay stepwise, equilibrating between each successive step. This and the observation of large fragment multiplicities are necessary conditions for the existence of a liquid-gas phase transition, but considerably more detailed information is needed. It is especially important to explore how these nuclear systems evolve from liquid to gas with excitation energy. Variations in excitation energy can be achieved either by varying the incident energy for central collisions or by varying the impact parameter for peripheral collisions at high incident energies.

Prior to this dissertation work, there existed only one excitation function for multifragmentation in the literature [deSo 91]. This previous study was performed for the $^{36}Ar + ^{197}Au$ system at E/A = 35-110 MeV [deSo 91]. It revealed that the fragment multiplicities in central collisions increase with incident energy over the range of energies measured. At significantly higher incident energies E/A = 600 MeV, other measurements were performed [Ogil 91, Hube 91] with a ^{197}Au beam which suggested that the fragment multiplicities are smaller in central than in peripheral collisions. These latter high incident

energy measurements were performed with a device with a relatively small efficiency for the detection of particles emitted in central collisions [Hube 91].

As indicated previously, comparisons of fragment multiplicities to QMD and QPD molecular dynamics calculations [deSo 91, Bowm 91] indicated that such calculations generally underpredicte the observed fragment multiplicities. Molecular dynamics predict that these fragment multiplicities should increase strongly with incident energy and reach a maximum at incident energies of the order of 100 A MeV. At energies of E/A = 200 MeV, a successful description of the fragment observables was in fact achieved with the QMD model for central Au + Au collisions [Peil 89]. Beyond E/A≈100 MeV, however, decreasing fragment multiplicities are expected on the general grounds that the fragments which are produced will likely be so highly excited that they will disintegrate into nucleons [Ogil 91]. This general consideration is also reflected in various calculations [Frie 90, Peil 92]; specific predictions for this decrease are provided by molecular dynamics models [Peil 92]. There is considerable interest in determining the incident energy dependence of the onset of nuclear vaporization and whether this energy dependence can be reproduced by molecular dynamics models.

Complimentary information may be obtained by examining the impact parameter dependence of multifragmentation at relatively high incident energies [Hube 92, Ogil 91, Kean 94, Wang 95]. Here, the onset of vaporization occurs as a function of impact parameter reflecting the impact parameter dependent excitation energy deposition into the reaction residues [Tsan 93, Ogil 91]. Both the sizes and the excitation energies of the residues vary with impact parameter complicating the interpretation of such data, however.

From previous studies [Phai 92], a quantitative understanding of the impact parameter and incident energy dependence of multifragmentation is now achieved. Despite these promising indications, information about the time evolution of the system in the (ρ,T) plane for bulk disintegration is necessary to proceed with the accurate extraction of thermodynamic quantities from such collisions, and to discern non-equilibrium and dynamical effects. With respect to the latter issue, it is particularly important to determine the relative importance of collective expansion to thermal excitation for the

multifragmentation process. This issue was also carefully investigated in this dissertation work. Estimates of the energy contained in collective motion were obtained [Jeon 94], and the role of this collective expansion upon the fragmentation process was explored [Hsi 94, Kund 95].

1.4 Outline of This Thesis

This thesis is organized as follows: Details of the experimentally designed procedures are described in Chapter 2. The experimental analysis is described in Chapter 3. The resulting experimental data, including the energy dependence of the fragment emission and the extraction of the energy of collective expansion, are described in Chapter 4. A summary is given in Chapter 5.

Chapter 2

Experimental Set-Up

The experiment was performed at the heavy ion Synchrotron (SIS) facility of Gesellschaft für Schwerionenforschung (GSI) at Darmstadt. Au projectiles with incident energies of E/A = 100, 250 and 400 MeV bombarded Au targets of various thicknesses. The experimental set-up included the Miniball/Miniwall phoswich array, Catania Si-CsI hodoscope array and Aladin spectrometer as shown in Fig. 2.1. Together, these detector arrays provided a coverage of more than 95% of 4π for detecting fragments with $Z \geq 2$. At polar angles of $14.5° \leq \theta_{lab} \leq 160°$, charged particles were detected in 215 plastic-scintillator-CsI(Tl) phoswich detectors of the Miniball/Miniwall arrays. Fragments ($2 \leq Z \leq 79$) moving with velocities around the beam rapidity were detected by the Aladin spectrometer [Aldi 89]. This spectrometer covered $|\theta_{lab}| \leq 10°$ in the horizontal (bend) plane and $|\theta_{lab}| \leq 5°$ in the vertical plane. Due to the dynamic range of the magnetic field used in this experiment, hydrogen particles were partially deflected out of the Time of Flight (ToF) wall acceptance. Since the detection efficiency of Z = 1 particle is not well defined in this spectrometer, Z = 1 particles emitted forward with $\theta_{lab} \leq 10°$ were not included in the data analysis. Charged particles emitted to angles between the Aladin spectrometer and the Miniball/Miniwall array were detected by the 84 elements Si-CsI(Tl) hodoscope array.

The main focus of this thesis is on the data obtained with the Miniball/Miniwall array which covered more than one half of the total solid angles in the center of mass frame. Therefore, only a brief description of the techniques relevant to the Aladin spectrometer and the Catania hodoscope will be described in this thesis. Further details of the Aladin spectrometer can be found in Refs. [Aldi 89] and [Kund 94]. The original Miniball array is described first in this chapter. Then, the upgrades to Miniball/Miniwall array and the Catania hodoscope and Aladin spectrometer are described. Finally, details of the data acquisition electronics of the Miniball/Miniwall are given in the final section.

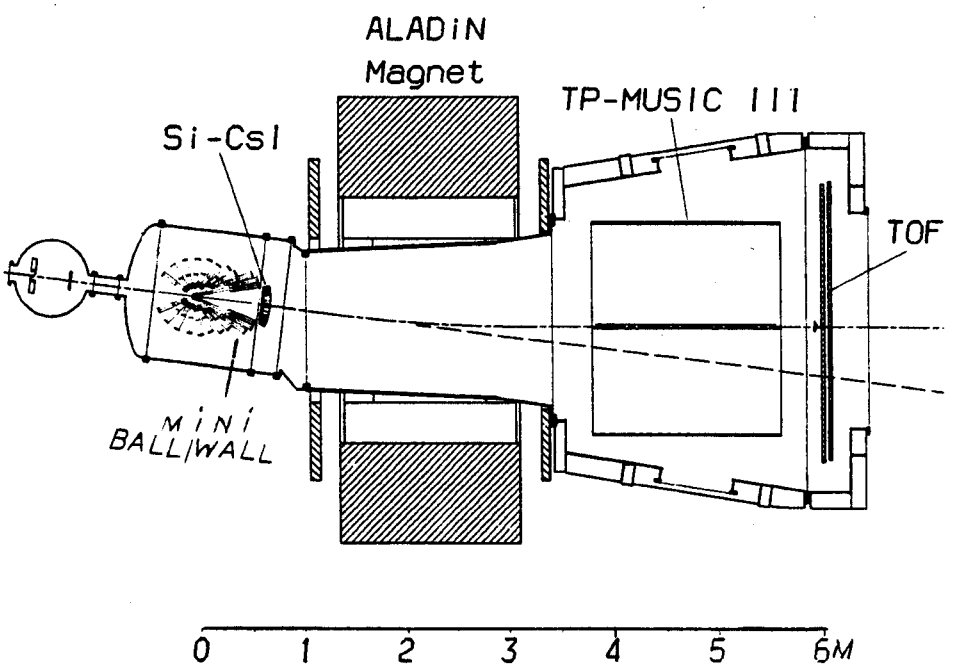

Figure 2.1 The schematic drawing of the experimental set-up. This experimental apparatus includes the Miniball/Miniwall array, the Catania Si-CsI hodoscope array and the Aladin spectrometer. The TP-MUSIC chamber and TOF wall are two main components of the Aladin spectrometer.

2.1 Original MSU Miniball Array

The original configuration of the Miniball is listed in Table 2.1 and a half-plane section of upgraded Miniball is plotted in Figure 2.2. This array consists of 11 independent rings coaxial about the beam axis. For ease of assembly and servicing, the individual rings are mounted on separate base plates which slide on two precision rails. For a given ring, the detectors are identical in shape and have the same polar angle with respect to the beam axis. Each phoswich detector of this array is composed of a thin 4 mg/cm^2 (or 40 μm) plastic scintillator foil, prepared from Bicron BC-498X scintillator solution, and a 2 cm CsI(Tl) scintillator crystal.

A schematic plot of the detector design is given in Figure 2.3. The front and back faces of the CsI(Tl) crystal were polished and the crystal was glued with optical cement (Bicron BC 600) to a flat light guide made of ultra-violet transparent (UVT) Plexiglass. The light guide was glued to a second cylindrical piece of UVT Plexiglas which, in turn, was glued to the front window of the photo-multiplier (PM) tube. The PM tube and the cylindrical light-guide were enclosed inside by a cylindrical μ-metal shield (not shown in Figure 2.3). The front face of the detector was covered by an aluminized mylar foil (0.15 mg/cm^2 mylar and 0.12 mg/cm^2 aluminum) to keep the detection assembly light-tight and also to suppress low energy secondary electrons form hitting the plastic scintillator. The fast scintillator of foil was used for charge particle identification; the thickness of foils (40 μm) were minimized to reduce particle detection thresholds. These low detection thresholds are particularly important for detecting intermediate mass fragments.

Since the angular distribution of emitted particles in heavy-ion collisions is strongly forward peaked [Kim 92], the solid angles of the forward detectors needed to be smaller than those of the backward detectors. Variations in solid angle were achieved largely by placing detectors at different distances from the target while keeping their sizes approximately constant. The crystals of Miniball detectors were tapered so that the front and back surfaces have the same solid angle with respect to the center of the target. The curved surfaces corresponding to the constant polar angle were approximated by planar surfaces. The absorption of light from the plastic scintillator by the CsI(Tl) crystal constrained the maximum useful thickness of the crystal. Under this constraint, a 2 cm

Table 2.1 Coverage in solid angle, polar angles, azimuthal angles and the distance from the front face of CsI crystal to the target (d) for individual detectors of the upgraded Miniball/Miniwall array. The Miniwall rings are labeled 1-2. The 3'-11 are the rings of upgraded Miniball. The first three rings of the original Miniball array are also listed in the parenthesis.

Ring	Detector	$\Delta\Omega$ (msr)	θ (degree)	$\Delta\theta$ (degree)	$\Delta\phi$ (degree)	d (mm)
1	24	5.30	16.6	4.14	15.0	305.2
	(12)	(12.3)	(12.5)	(7.0)	(30.0)	(260)
2	24	10.36	21.9	6.15	15.0	312.5
	(16)	(14.7)	(19.5)	(7.0)	(22.5)	(220)
3'	28	11.02	28.0	6.0	12.86	280
	(24)	(18.5)	(27.0)	(8.0)	(18.0)	(180)
4	24	22.9	35.5	9.0	15.0	160
5	24	30.8	45.0	10.	15.0	140
6	20	64.8	57.5	15.	18.0	90
7	20	74.0	72.5	15,	18.0	90
8	18(-1)	113.3	90.0	20.	20.0	70
9	14	135.1	110.0	20.	25.7	70
10	12	128.3	130.0	20.	30.0	70
11	8	125.7	150.0	20.	45.0	70

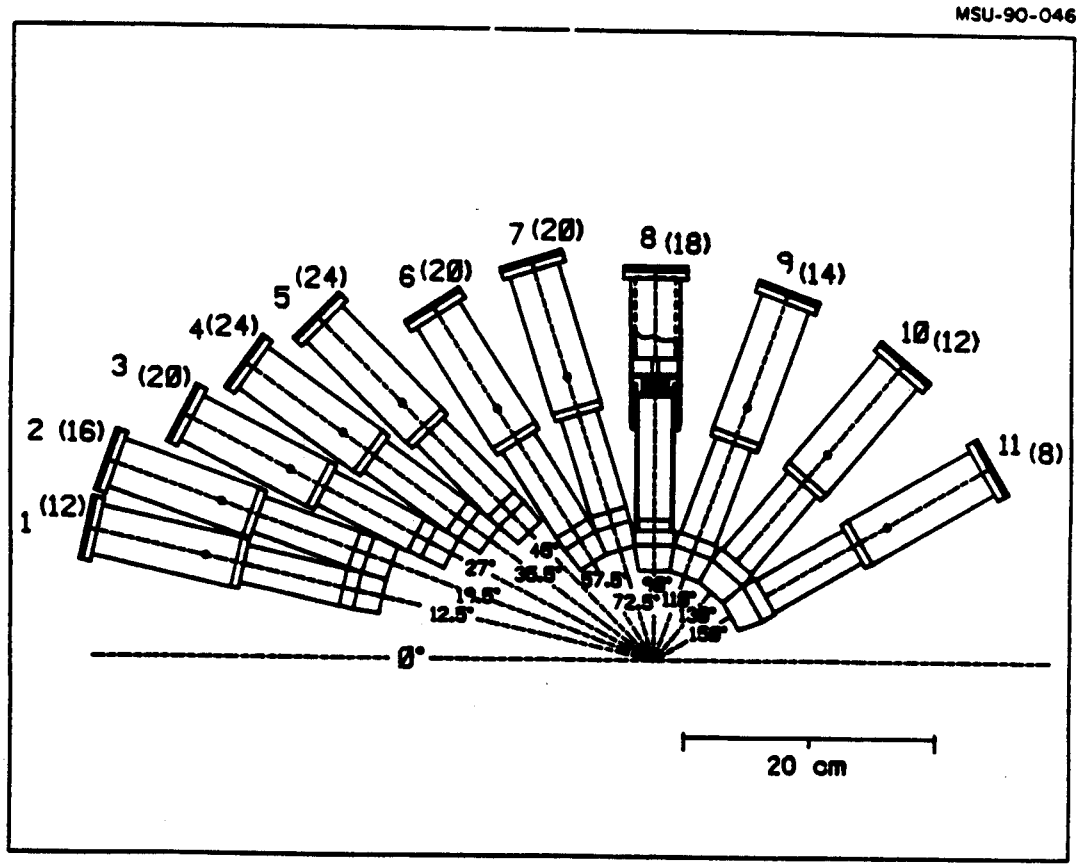

Figure 2.2 Half-plane section of the original Miniball array. Number of detectors per ring are given in parentheses. The polar angles for the centers of detectors are indicated. The dashed horizontal line indicates the beam axis.

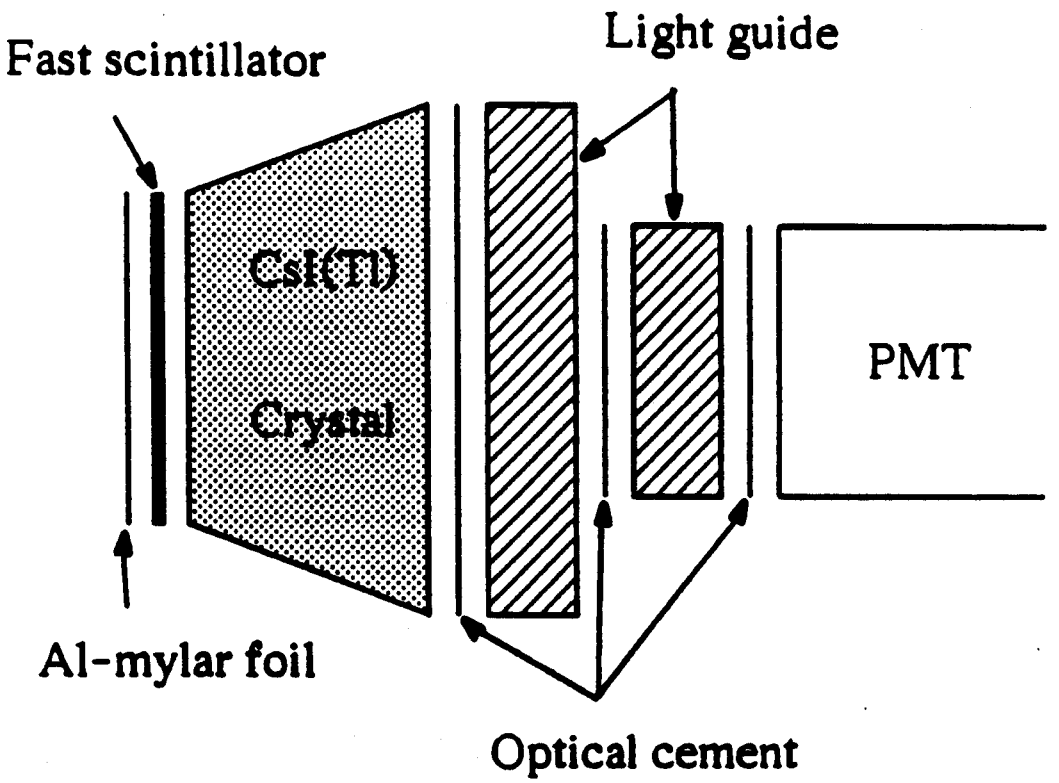

Figure 2.3 Schematic diagram of individual detector elements.

thicknesses of the crystals were chosen to obtain a dynamic range suitable for intermediate energy heavy-ion collisions and also to limit the effect of light absorption.

The 10-stage PM tube (Burle industries model C830622E) was chosen for its good timing characteristics (τ_R~2.3 ns), its large nominal gain (~10^7), and its good linearity for large signals ($I_{peak} \approx 30$ mA). Since the detection array was operated in vacuum, an active divider was designed to minimize the heat generation. A schematic diagram of the active divider is given in Figure 2.4. The values of the resistors in the original divider are listed in parenthesis. The voltage steps are shaped in order to maintain large voltage drops on the final amplification stages, because that minimizes the influence of space charge dependent gain shifts that occur for large peak currents of order $I_{peak} \approx 30$ mA. The choice of an active base allowed for a higher degree of gain stability under count rate fluctuations. The current supporting the dynode voltages runs through the resistors for the first seven voltage stages and then principally through the transistors on the last four voltage stages when the tube is quiescent. This allows for large currents to resupply the dynodes without the large heat dissipation one would experience with a passive base. The resistors on the last four stages provide reference voltages about which the voltages on D7-D10 are stabilized., The large capacitors at the final stages provided additional stability against sagging under large pulses in the phototube.

The CsI(Tl) crystals used in the Miniball array were selected to have good uniformity of scintillation response. In a test of large cylindrical crystals [Gong 88, Gong 90], possible non-uniformities of the scintillator due to non-uniformities in the thallium doping of the CsI(Tl) crystal were measured with a collimated 661 KeV γ-ray source. Since the range of electrons [Knol 79] excited by the photoelectric absorption of these γ-rays is comparable to the sizes of these small volume Miniball crystals, the γ-ray method is not well suited to testing Miniball detector uniformities. Instead, the non-uniformity of the scintillation efficiency was measured by scanning the crystals in vacuum with a collimated 8.75 MeV ^{228}Th α-source. This procedure takes advantage of the fact that α particles are more sensitive to Thallium doping and that the short range of the alpha particles allows for tests of local variations in the doping concentration [Birk 64, Mana 62]. To avoid edge effects, regions within about 2 mm of the sides of the crystals were not scanned. For

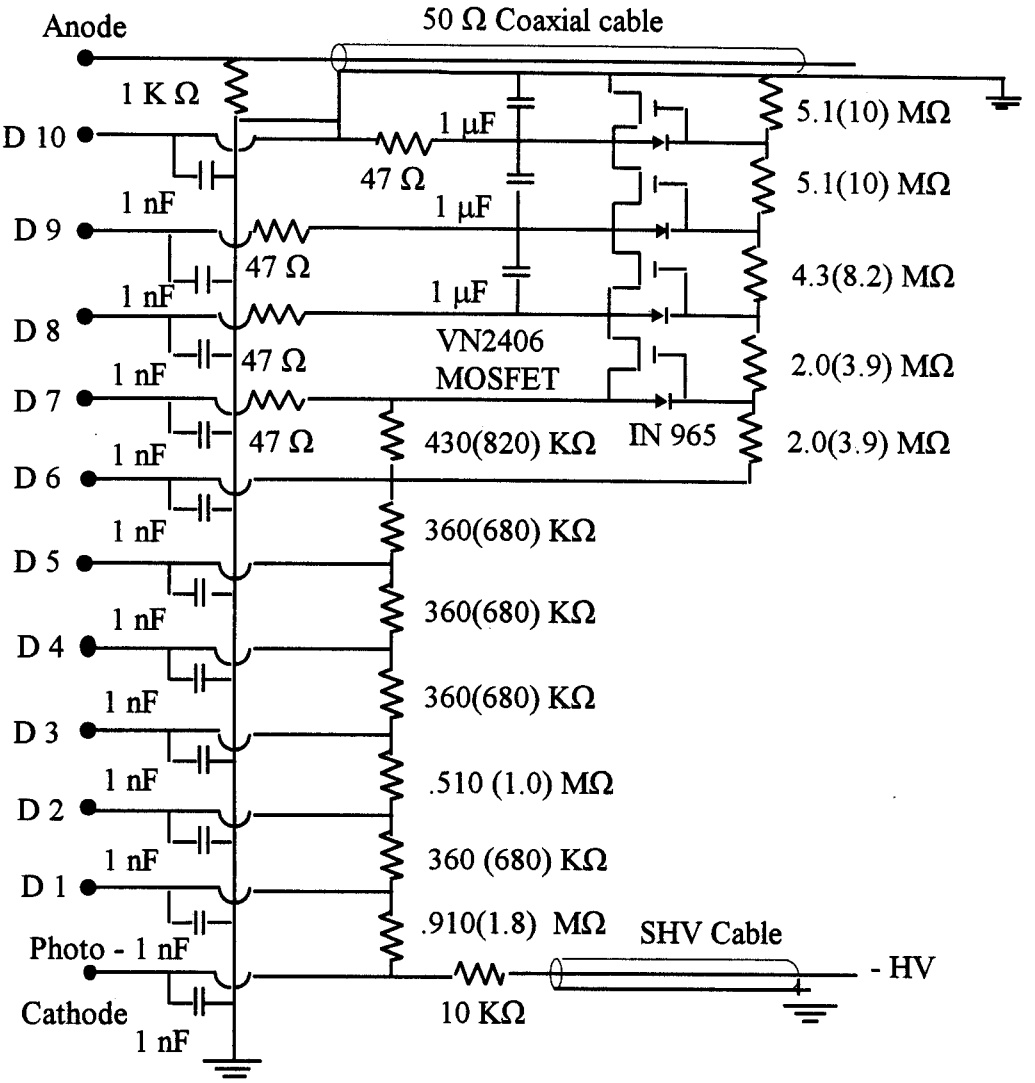

Figure 2.4 Schematic diagram of the upgraded active voltage divider used for Rings 9, 10 and 11 of the Miniball array. The value of resistors for the original divider are listed in parenthesis.

acceptance in the array, a uniformity of scintillation response better than 3% to the α particles was required. The pre-selected crystals were then machined into their final shapes and scanned a second time, requiring uniformity of response within 2.5%. More details of the quality control tests can be found in Ref. [deSo 90].

The detection principle of the Miniball detectors is based on the plastic-CsI(Tl) phoswich technique. The anode signal from the PM tube has the shape shown schematically in Fig. 2.5. It reflects signal components from the scintillation of the plastic foil (fast) and the CsI crystal (slow and tail). (The amplitude of the signal can be individually adjusted for each detector by a computerized adjustment of the voltage on the PM tube.) These signals were integrated with the three time gates indicated at the bottom of Figure 2.5, corresponding to the various scintillation components. The fast and slow signals are combined to determine the charge of the detected particles. The slow and tail signals are combined to determine the mass of the hydrogen and helium isotopes. The energy of the detected particles was extracted from the amplitude of the signal within the slow gate. Further details of these particle identification and energy calibration techniques are discussed in the next chapter.

2.2 Upgraded Miniball/Miniwall Arrays

The geometry of the original Miniball array was designed to address the problems of accurately measuring multiplicity and angular distributions in asymmetric $^{36}Ar + ^{197}Au$ collisions [Kim 92, deSo 91, Phai 92]. The original Miniball array contained 187 phoswich detectors to cover the angular domain $9° \leq \theta_{lab} \leq 160°$. However, heavy symmetrical systems, such as Au+Au, result in higher multiplicities and problems with double hits. For such heavy systems, modifications in the Miniball at $\theta_{lab} \leq 30°$ were required to address these problems. Thus, 48 detectors, covering $9° \leq \theta_{lab} \leq 31°$ of the first three rings in the original Miniball array were replaced in this dissertation work by 48 detectors of the Miniwall array at $14.5° \leq \theta_{lab} \leq 25°$, 28 detectors of an improved third ring of the Miniball array at $25° \leq \theta_{lab} \leq 31°$, and by 84-elements of the Catania hodoscope and the Aladin spectrometer at $\theta_{lab} \leq 14.5°$. It would have been useful to upgrade Rings 4

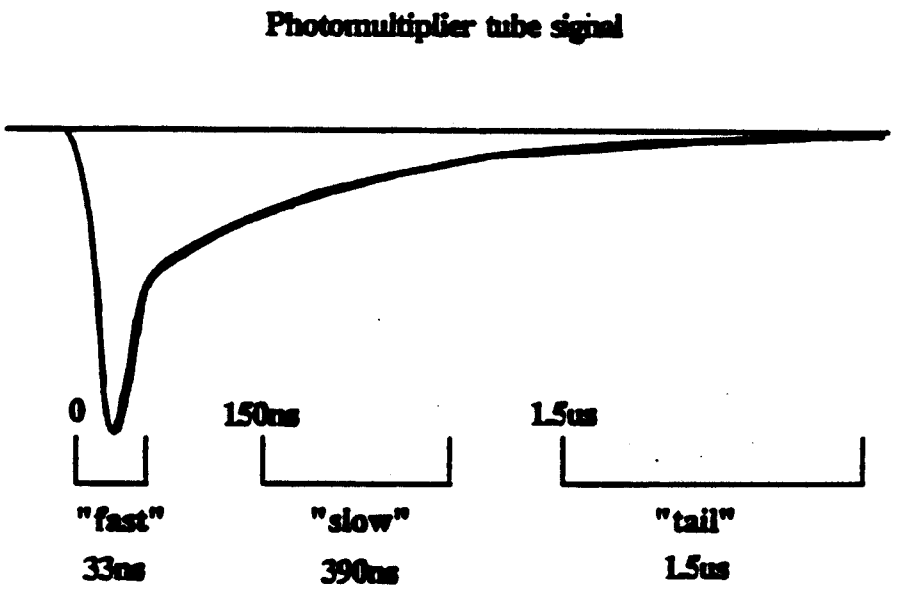

Figure 2.5 Timing and widths of the fast, slow and tail gates.

and 5 of the Miniball, but the double hit probabilities were not so significant, and there were insufficient resources to replace the detectors in these rings.

Upgrade of Miniball Array

The final configuration of the Miniball/Miniwall array is listed in Table 2.1 and a half-plane section of the upgraded Miniball/Miniwall is plotted in Figure 2.6. Rings 1 and 2 of the upgraded array are part of the Miniwall array built at Washington University (St. Louis), described in detail in the next section. To improve the detection efficiency at the forward angles and to match ring 4 of the Miniball to the Miniwall, a new forward ring 3' of the Miniball, containing 28 detectors, was built. These detectors were located at a longer distance (280 mm) from the target, significantly reducing the solid angle and double hit probability relative to that for the original array. For comparison, the configuration for the first three original Miniball rings is also listed in parenthesis in Table 2.1.

Some technical improvements were employed in constructing these new detectors. In the original Miniball detectors, one observed occasional sparking between the external high voltage field shaping electrode and the μ-metal magnetic shield which surrounded the entire PM tube assembly and was held at ground potential. To suppress such problems, the gap between these two surfaces was filled with epoxy. Unfortunately, there were voids in this epoxy layer that became depleted of air after several days of operating in vacuum and subsequently became a weak point in the insulation where sparking could occur. To reduce this problem, the epoxy layer was degassed under vacuum while it was curing. This and some additional refinements in the gluing procedure resulted in a completely stable operation under vacuum.

A second improvement was made to the Rings 9, 10 and 11 of the Miniball detectors to handle higher counting rates. In heavy ion bombardment, secondary electrons, X-rays and to a lesser extent γ-rays are emitted more copiously at all angles than in the case of light ion bombardment. Since solid angles of the backward detectors are larger than those at forward angles by a factor of 10-20, the electron, X-ray and γ-ray counting rates in these backward detectors are far bigger than the rates in the forward detectors. At high beam intensities, these high counting rates can cause the bases of the PM tubes for

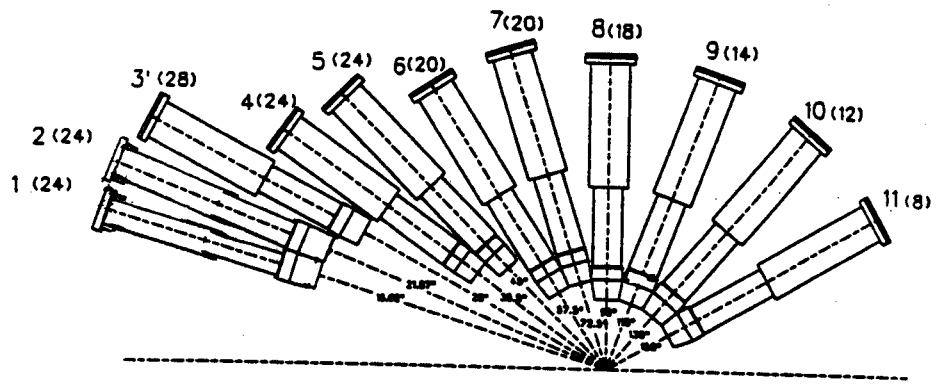

Figure 2.6 Half-plane section of the upgraded Miniball/Miniwall array. The rings of the Miniwall are labeled with 1-2 and rings 3'-11 label the individual rings for Miniball.. The number of detectors per ring are given in parentheses. The polar angles for the centers of detectors are indicated. The dashed horizontal line indicates the beam axis.

these detectors to become over-loaded. The overloaded detectors will have a worse charge particle resolution, and the bases can shut off when the currents in the PM tubes are sufficiently large. Some reduction in sensitivity to the electrons can be achieved by covering the detectors with absorber foils (typically of an Pb-Sn alloy with 5 mg/cm^2 aerial density). Even with covered foils, at times the tube currents at the back angles can be too high, requiring reductions in the beam intensity and a resulting loss of data. This can prevent investigations of issues for which high statistics are required. One example of such an investigation can be found in Ref. [Zhu 92].

To increase the count rate capability of these backward detectors, new bases were constructed for the detectors in rings 9-11 to handle higher count rates. The original bases did not always precisely display the same failure mode. Nevertheless, an increased count rate stability will result when the D.C current passing through the resistor network of the bases considerably exceeds any fluctuations in the load caused by a fluctuating count rate [Gupt 67]. Thus the tube stabilities were increased by decreasing the resistance in the passive divider networks by about a factor of two, as shown in Fig. 2.4.

To test these modifications, the variation of the pulse height [Mich 65] of a typical Miniball detector was studied as a function of the counting rate of the detected γ-rays from a $_{27}Co^{60}$ source. A drawing of the setup and the associated electronics used for this purpose is shown in the Fig. 2.7. The detector was put in a light-tight chamber. The Co^{60} source could slide towards and away from the detector, thus allowing changes in the counting rate due to changes in the γ-ray flux at the detector. The counting rates were read out by a scalar. The signal of the PM tube was amplified and read out by a multichannel-analyzer (MCA). Two 1.174 and 1.332 MeV γ-rays are emitted in a $(4^+ \rightarrow 2^+ \rightarrow 0^+)$ cascade in the excited $_{28}Ni^{60}$, which is the product of the β decay of Co^{60}. The γ-ray energy spectra reveal two photopeaks at these two energies and a Compton scattering continuum. The shifts of both peaks were examined to reveal any count-rate dependencies of the PM tube gain.

To simplify the comparison between the modified and original Miniball voltage dividers, the two dividers used the same PM tube coupled to the same CsI crystal. The same high voltage was also applied to the PM tube for each divider (base). Under this

condition, the performances of the dividers could be compared by considering the count rate dependent shifts in the peaks in the γ-ray spectra, reflecting a gain change in the PM tube due to alterations in the voltages supplied by its base (divider). The γ-ray photopeak pulse height divided by a reference pulse heights obtained at 25 counts/sec are plotted in Fig. 2.8 as a function of the counting rate for the two bases. The corresponding distances between the source and detector were labeled at the top of Fig. 2.8. Large shifts in the peaks measured with the original divider occurred when the counting rate was greater than 300 counts/sec. Large shifts in the peaks measured with the modified divider did not occur until the count rate exceeded 900 counts/sec, indicating a significantly higher count rate capability with the new base.

Miniwall Detection Array

The Miniwall detector array was built by L.G. Sobotka et. al. at Washington University in St. Louis. The array consists of 6 rings, a total of 128 detectors, spanning from $\theta_{lab} = 3.3°$ to 25.0°. In this experiment, only the two backward rings covering angles ranging from $\theta_{lab} = 16.6°$ to 25.0° were used. The rings are labeled as rings 1 and 2 in Fig. 2.6. Similar to the Miniball, each detector contained a fast plastic foil (~8. mg/cm^2) and a 3 cm long CsI(Tl) crystal. The crystal was coupled by a light guide to a PM tube (Hamamatsu model R647). For these tubes, a passive voltage divider was used, requiring significant cooling of the array. The PM tubes with similar gains were used for neighboring detectors so that the same high voltage was applied in parallel. This method reduced the number of high voltage channels, but had the disadvantage that the gains of individual detectors could not be individually adjusted by applying different voltages. Similar to the Miniball, three different time gates; the fast, slow and tail, were applied on the signal out of the PM tube. The mechanical configuration of the Miniwall was very compact with all the detectors attached to the same plate. A cooling line was mounted around the edge of the plate to keep the temperature of the PM tubes constant during the experiment.

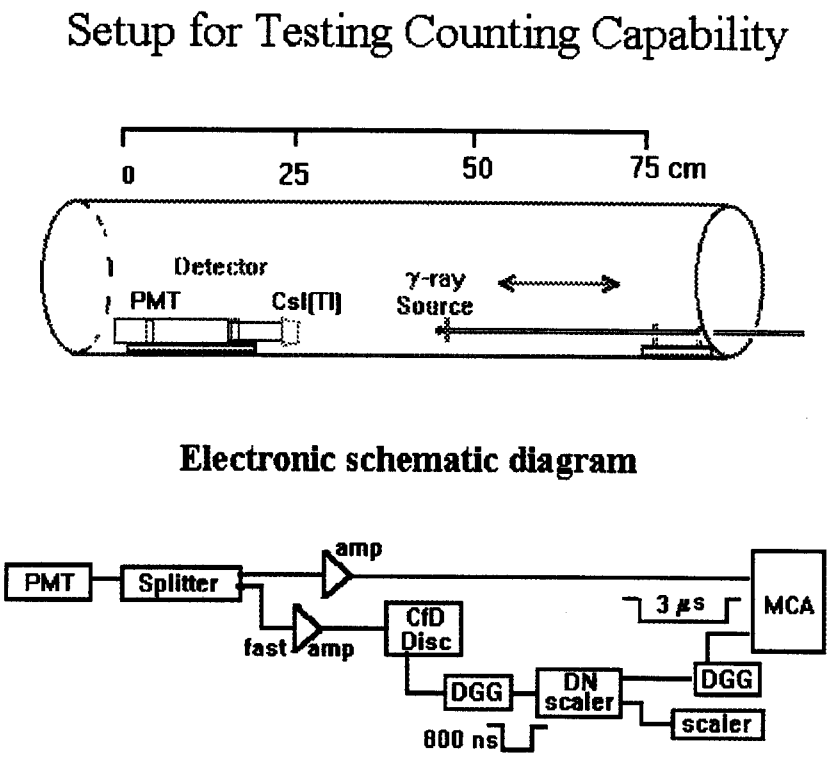

Figure 2.7 The set-up for testing the counting capability of the PM tube with different voltage dividers is shown. The electronic diagram also is drawn in here. The Co^{60} was moved to vary the intensity of γ-rays hitting the detector and to allow one to monitor the shifts of the peaks with a multi-channel-analyzer (MCA). The counting rate was read out by a scalar as a function of source intensity and the distance between the source and the detector. The down scalar was inserted to ensure negligible MCA dead time.

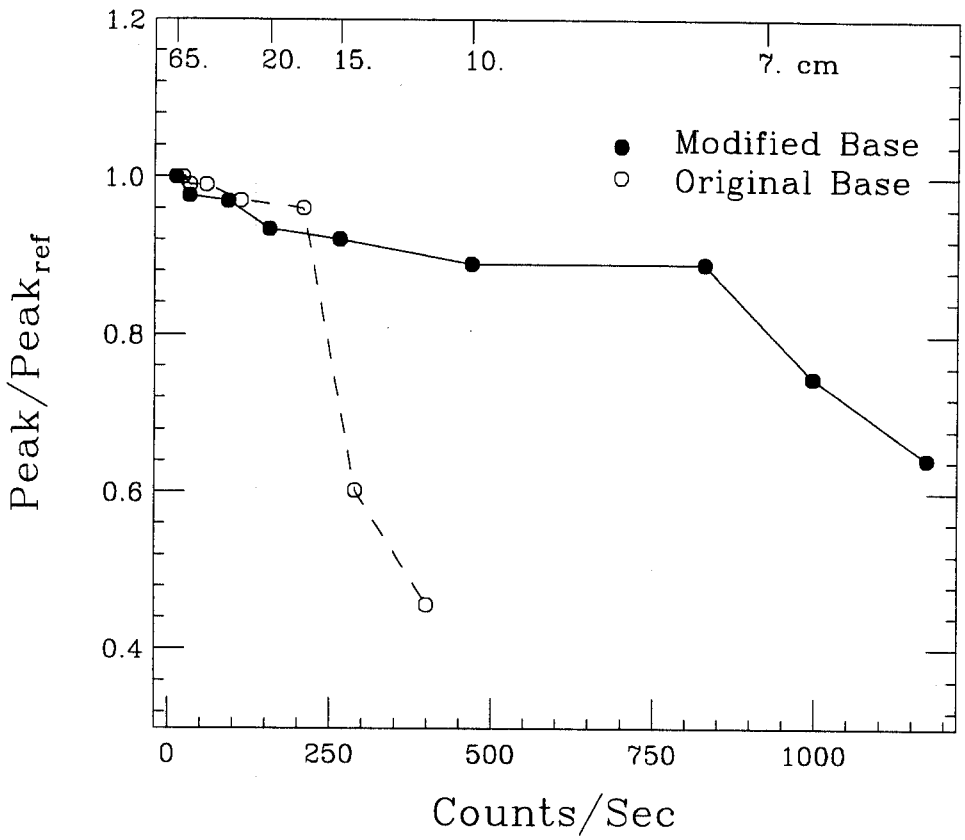

Figure 2.8 The relate magnitudes of the γ-ray peaks are plotted as a function of the counting rate for the two different voltage dividers. The distance between the source and detector is indicated at the top of this Figure.

2.3 Catania Si-CsI Hodoscope

The Catania Si-CsI hodoscope array contains 84 Si-CsI telescopes, arranged as shown in Fig. 2.9. The polar and azimuthal angles for the centers of these detectors are listed in Table 2.2. Each detector telescope consists of a 300 μm thick Si detector backed by a 6 cm thick CsI(Tl) crystal. The signal of each CsI(Tl) detector was read out by a pin-diode. The size of the front face is approximately 30 x 30 mm^2. Each Si detector had a dead region 1 mm wide along the edges of the detectors. At polar angles greater than 14.5°, the telescopes were blocked by the Miniwall array, as discussed in the previous section. Software gates were set to avoid the double counting of particles that punched through the Miniwall into the partially covered Cantania array. Signals from the array were amplified by preamplifiers inside the scattering chamber and further amplified by computer controlled shaping amplifiers before being digitized by a Fast Bus charge integrating ADC. Information from the Catania array for each event was written on tape along with the data from the Miniball/Miniwall and Aladin spectrometers. Further details of the mechanical and detector designs can be found in refs. [Kund 94, Lind 93].

2.4 Aladin Spectrometer

The Aladin spectrometer consists of three main components: a larger bore dipole magnet, a multiple-sampling ionization chamber (TP-MUSIC), and the time-of-flight wall (ToF). In the data discussed in this dissertation, the beam intensity was chosen to be too large for the TP-MUSIC to function, and so data was obtained only with the ToF Wall. The ToF wall is a layered structure consisting of two arrays of 96 plastic scintillators arranged with one array in front of the other. Each plastic scintillator is 1100 x 25 mm^2 in its frontal area with a thickness of 10 mm. Signals from each scintillator were readout by two PM tubes, one at each end of the 1.1 m long scintillator. The signal from each PM tube was discriminated to obtain a timing signal, and the time and amplitude of each pulse were digitized in Fast Bus modules and written on tape along with the rest of the information from each event. Further details of the design were described in Refs. [Aldi 89, Lind 93].

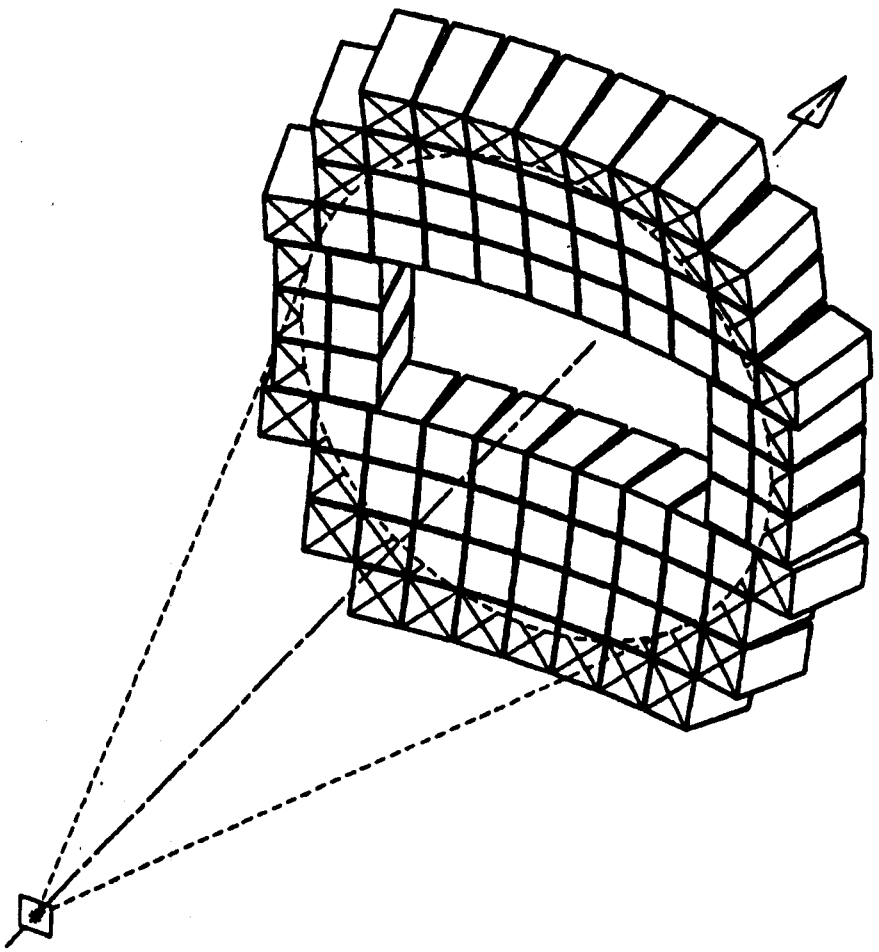

Figure 2.9 Three dimensional geometric diagram of the Catania hodoscope array.

Table 2.2 The centroid of the polar and azimuthal angles of the Catania detector are listed.

The polar angles of these detectors:

		17.8	16.2	15.1	14.8	15.4	16.1	17.6		
	17.4	15.1	13.4	12.3	11.8	12.2	13.3	14.9	17.2	
	15.2	12.8	10.8	9.3	8.9	9.4	10.9	12.6	15.2	
16.6	13.5	10.8	8.3	6.4	5.6	6.4	8.3	10.6	13.3	16.1
13.5	10.9								11.1	13.9
13.3	10.9								10.8	13.6
13.5	10.9								11.1	13.9
16.2	13.2	10.6	8.1	6.3	5.5	6.2	8.1	10.4	12.9	15.7
	14.8	12.5	10.5	9.1	8.6	9.1	10.6	12.3	14.8	
	17.4	14.8	13.1	12.0	11.5	12.0	13.0	14.5	16.8	
		17.3	15.8	14.8	14.5	15.0	15.7	17.1		

The azimuthal angles of these detectors:

		122.0	112.8	101.9	90.7	79.3	68.1	59.0		
	135.4	127.8	118.1	105.6	91.3	76.6	62.9	52.8	44.3	
	143.1	135.3	124.6	109.5	90.6	71.2	55.6	47.7	36.9	
158.4	153.8	147.8	136.3	118.0	90.9	63.8	44.1	32.3	25.9	21.6
169.0	166.3								13.7	11.0
180.0	180.0								0.0	0.0
191.0	193.7								346.3	348.3
201.6	206.2	212.2	223.7	242.0	269.1	296.2	315.9	327.7	334.1	338.4
	216.9	224.7	235.4	250.5	269.4	288.8	304.4	315.3	323.1	
	224.6	232.6	241.9	254.4	268.7	283.4	297.1	307.2	315.7	
		238.0	247.2	258.1	269.3	280.7	291.9	301.0		

2.5 Data Acquisition Electronics

Fig. 2.10 shows a block diagram of the electronic set-up used for the Miniball array in this experiment. The shape of the anode current from the PM tube, shown in Fig. 2.5, was split via passive splitters into "fast", " slow", "tail" and "trigger" branches with relative amplitudes $I_{fast} : I_{slow} : I_{tail} : I_{trig} \approx 0.82: 0.04: 0.04: 0.10$ for the currents. The gate widths for the fast, slow and tail are also shown in the bottom of Fig. 2.5. During the readout of FERA's (Fast Encoding and Readout ADC), integer*2 words for fast, slow, tail, and time are written to the tape for the detectors that have trigger signals above the threshold. Since high energy fragments were emitted abundantly into the forward angles in Au+Au reactions, the splitter ratios for slow and tail signals of rings 3'- 5 were reduced by a factor of two to keep the signals within the dynamic range of the FERA, ADC.

Signals from the Miniwall detectors were processed by different electronics. Fig. 2.11 shows the electronics block diagram for the Miniwall array [Stra 90]. The anode signal from each PM tube was amplified by a fast variable gain amplifier before the signal was split into the "fast", " slow" and "tail" parts. The logic signal came from the second output of the amplifier. Similar to the Miniball detectors, the fast, slow, tail and time signals were written to tape for all detectors that had trigger signals above the discriminator thresholds.

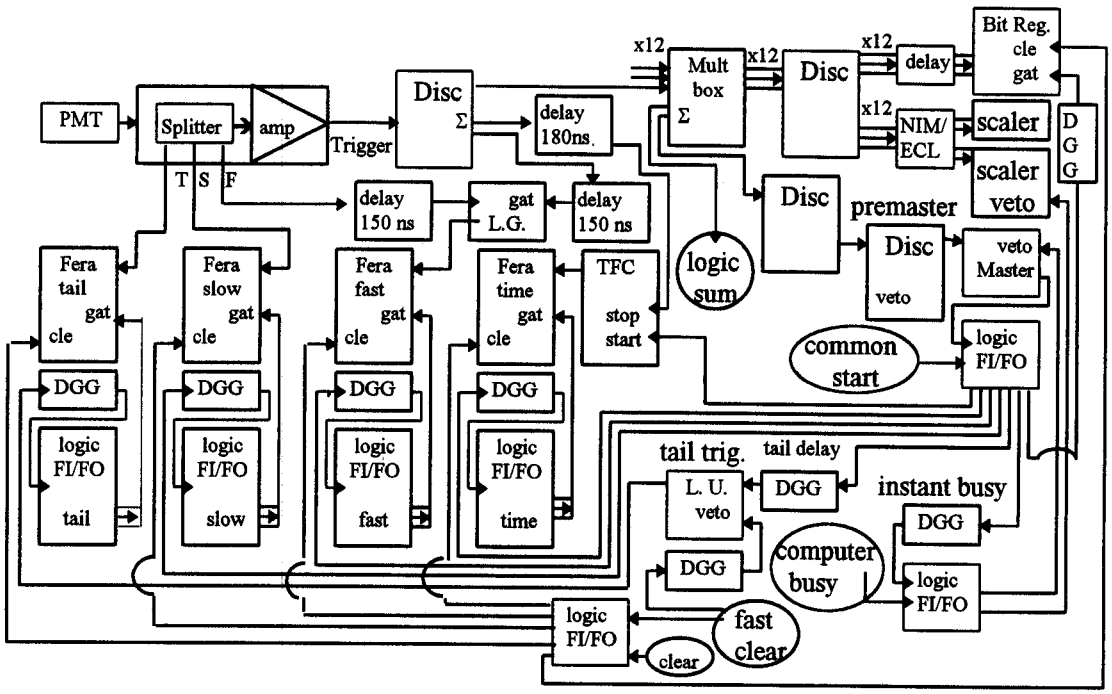

Figure 2.10 Schematic electronics diagram of the data acquisition of the electronics for the Miniball array alone. The Disc, Split., DGG, Fera, Amp., L.U. and FI/FO present Discriminator, splitter, delay and gate generator, Fera ADC, amplifier, logical unit and the fan in/fan out models respectively.

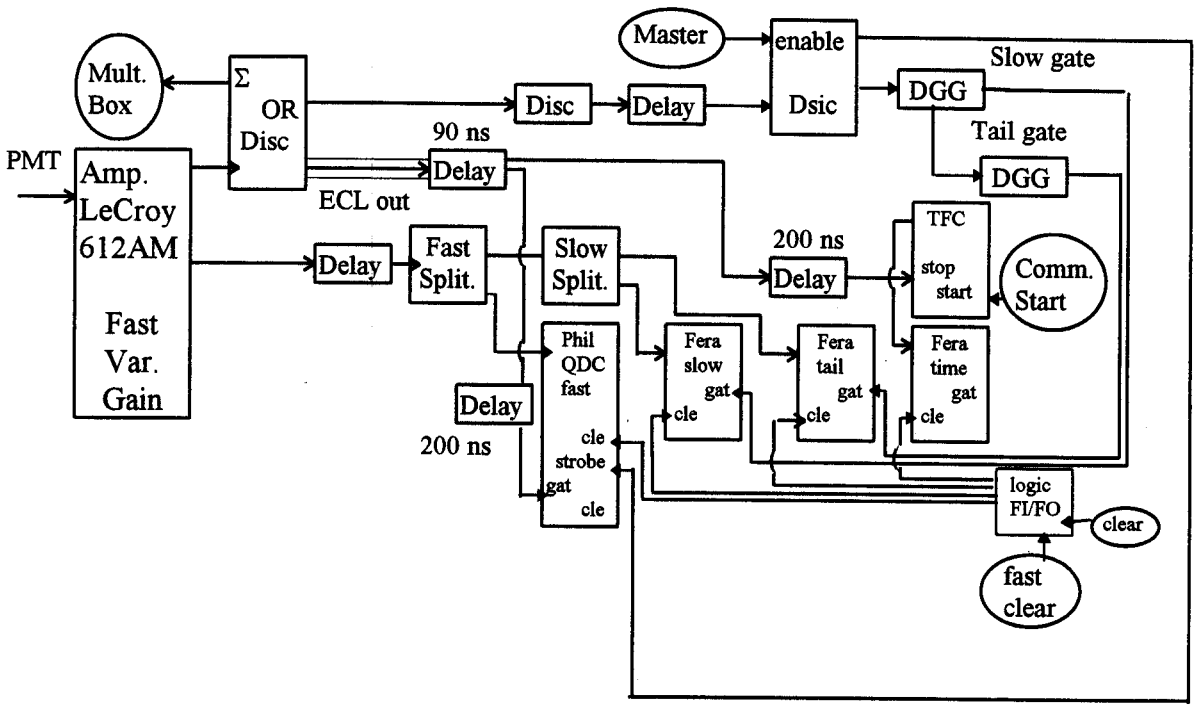

Figure 2.11 Schematic electronics diagram of the data acquisition of the electronics for the Miniwall array alone. The Phis QDC is the Phillips QDC model.

Chapter 3

Data Analysis

In general, each device in this experiment uses a different detection principle to resolve the charge, mass and energy of the detected particle. To extract this information from the raw data, different particle identification procedures and energy calibrations were used for each device. Details of the particle identification and the energy calibration for the Miniball/Miniwall will be described first in following two subsections. The energy calibration of the Catania hodoscope was recently done by the Catania group [Raci 95]. Since the energies of the particles detected in the Catania hodoscope were not used in the following data analyses, only the particle identification principle of this device is briefly described in this thesis. This is followed by a description of the particle identification, and the energy and angular determination techniques used for the ToF wall of the Aladin spectrometer.

3.1 Particle Identification of the Miniball/Miniwall

For each detector of the Miniball/Miniwall, the "fast", "slow", "tail" and "time" signals were recorded in the raw data, as described in Chapter 2. By plotting the fast versus slow components of the signal, clear element identification can be obtained [deSo 90]. By using the tail versus slow spectra, the isotopes of hydrogen and helium can be separated [deSo 90, Kim 91]. A total of 300,000 events were collected in the Au + Au collisions at E/A = 100, 250 and 400 MeV. Due to a lack of statistics, the drawing of the charge particle gates became very difficult, especially for the higher charges. The response of each detector was therefore mapped from scintillation response functions for the same detectors obtained in high statistics measurements at lower energies. To provide guidance for this procedure, we chose two experiments, the Saturne experiment and the NSCL-91014 experiment. Both experiments were designed to study Kr + Au collisions from E/A = 35 to 400 MeV, and included the same set of Miniball/Miniwall detectors used

in the present setup. NSCL-91014 collected a total of 60,000,000 events, while 5,000,000 events were collected in the Saturne experiment.

Charge Identification

Figure 3.1 shows the fast versus slow spectrum for the fifth detector of ring 3' (detector 3'-5) in the NSCL-91014 experiment. To facilitate drawing the charged particle gates, these charge lines were linearized as shown in Figure 3.2a. The final charge gates were drawn on these linearized spectra. To reduce the number of charge gates set in the fast versus slow spectra, the detectors used in the experiment were classified into several groups with similar detector response. Within each group, the detector with the best charge resolution was chosen as the reference. The two-dimensional fast versus slow spectrum of each detector within a group is scaled to match the spectrum of its reference detector. The proton-punch-through point of the "slow" signal of each detector was first scaled to the one on the reference spectrum to provide the scaling factor for the slow component. Since the "fast" signal is very sensitive to the temperature dependent scintillation efficiency of the plastic foil and the thallium doping of the CsI crystal, the alpha particle line of each detector was separately fitted to the reference alpha line with individual "slope" and "off-set" parameters for the fast component.

After the two dimensional fits were obtained, the "fast" versus "slow" spectra of individual detectors had shapes similar to the reference spectra. Ideally, the particle identification lines of all the charged particles would sit in the same positions as those in the reference spectra and could be optimally linearized with the same parameters. In practice, this proved to not be so simple. Nevertheless, charge gates could be easily set on the linearized spectra for the high statistics measurements, and mapped to the low statistics spectra of the Au + Au measurements presented here. Fig. 3.2b shows the corresponding low statistics linearized spectra for the GSI measurement. With the procedure described above and guided by the spectra with high statistics, charge gates up to Z = 6 were set on the low statistics GSI data. Beyond Z = 6, extrapolations could be used to obtain the charge gates, but in general, the quality of the energy spectra for these

heavier particles was quite poor. Therefore, the energy information with Z > 6 was not used in this analyses which are described later.

Most of the Miniball detectors had the particle identification lines drawn by the above procedure. This procedure was also used for Miniwall detectors which had crystals with similar doping as the bulk of the Miniball detectors. However, for CsI crystals in the Miniball that were produced by Bicron Corporation, the doping concentration was different. Such crystals were generally used in rings beyond $\theta_{lab} = 90°$. Charge resolution for these Bicron-like detectors cannot be achieved via gates on the fast versus slow spectra, but require gates on the fast versus tail spectra. In general only charge gates up to Z = 4 were set for these detectors. Due to a mistake in the electronics setup, charge resolution was achieved only up to Z = 4 in the Miniwall at E/A = 400 MeV; this problem was corrected for the measurements at E/A = 250 and 100 MeV.

Isotope Separation of Hydrogen and Helium

The pulse shape discrimination of CsI(Tl) crystals allows the isotope separation of hydrogen and helium particles. The procedure described here was first developed by Y.D. Kim [Kim 91]. Due to the high abundances of hydrogen and helium particles, spectra in the present experiment were sufficient to set the gates. Figure 3.3 shows the tail versus slow spectra for detector 3'-5. From this spectra, p, d and t isotopes of Z = 1 particles and ^{3}He and alpha isotopes of Z = 2 particles were quite difficult to separate. Using the upper and lower limit lines which encompass the area of the spectrum (see Fig. 3.4) with counts, we construct the following parameters:

$$Tail_r = Tail + \delta \qquad (3.1)$$

where δ is a random number between -.5 and .5 which is added o remove digitization from the displayed spectra. We also define

$$Tail_1 = Line_1\,(slow) \qquad (3.2)$$

$$Tail_2 = Line_2\,(slow) \qquad (3.3)$$

where $Line_1$ and $Line_2$ are used to designate to the upper and lower lines respectively which are parameterized as a function of the slow signal;

$$\Delta_{max} = Tail_1 - Tail_2 \qquad (3.4)$$

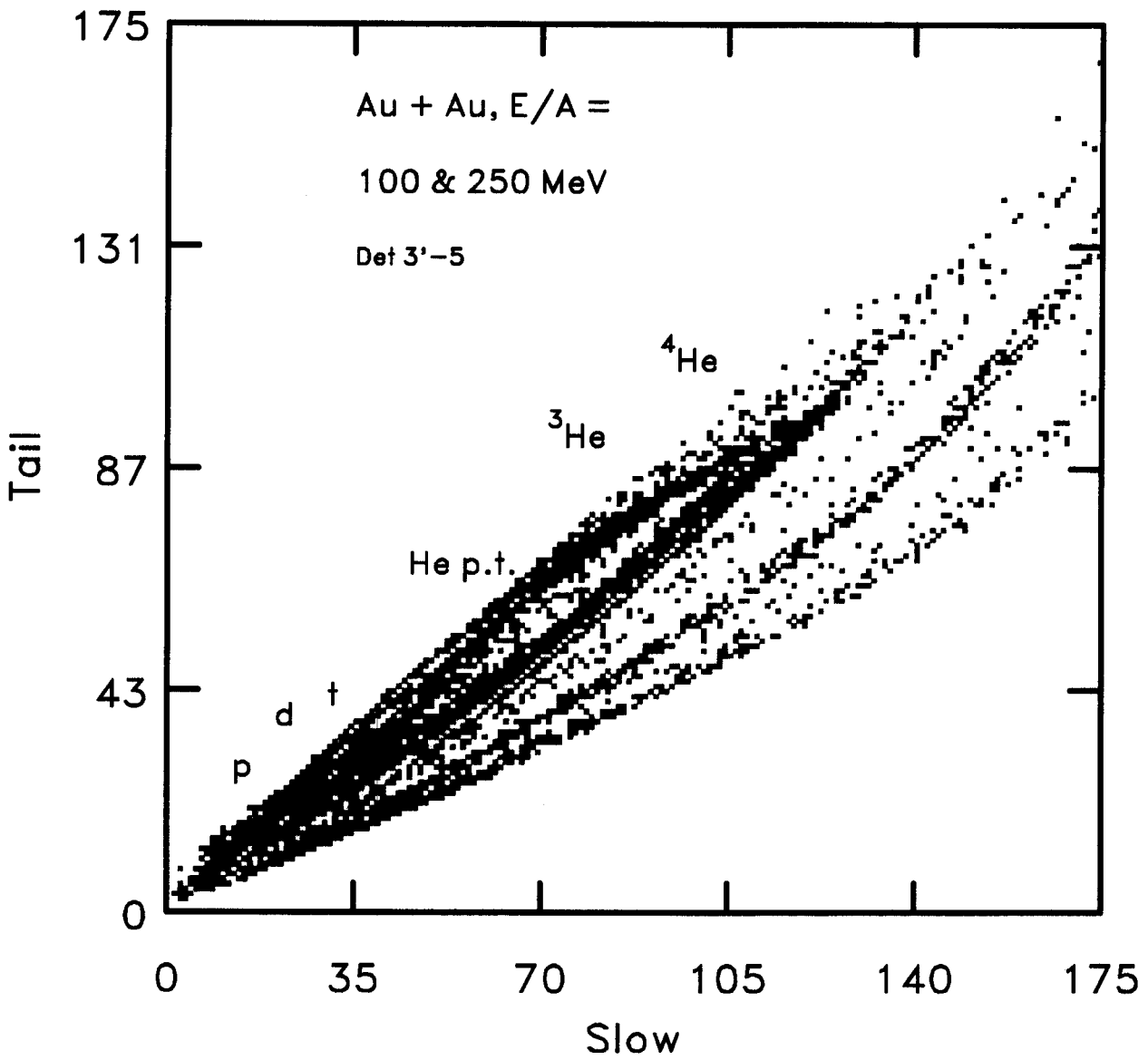

Figure 3.3 The tail versus slow spectrum for detector 3'-5 generated by combining all the runs of Au + Au collisions at E/A= 100 MeV/A and 250 MeV obtained in this experiment

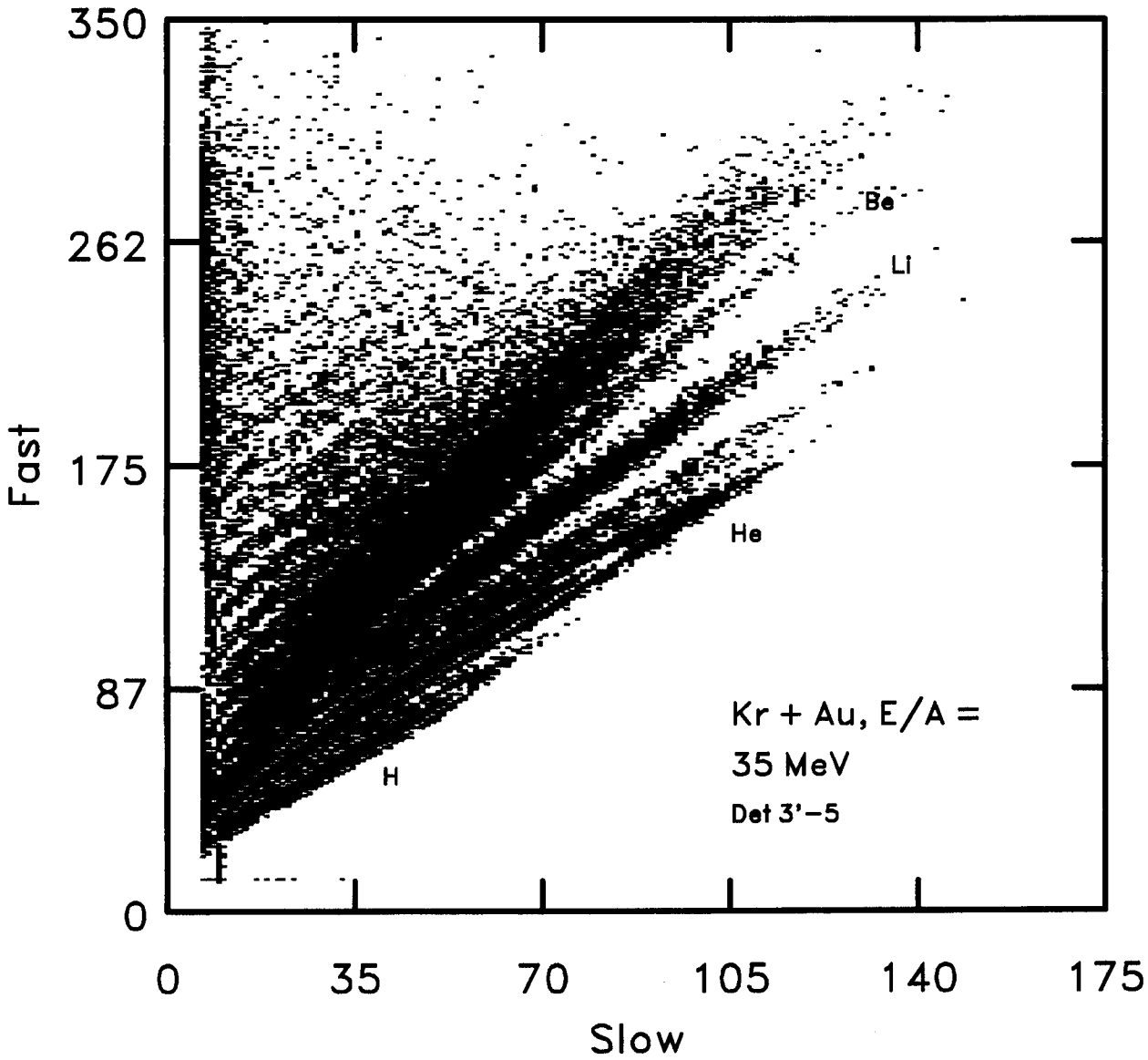

Figure 3.1 Fast versus slow spectrum with high statistics for detector 3'-5 (ring 3', position 5) obtained for Kr + Au collisions at E/A = 35 MeV.

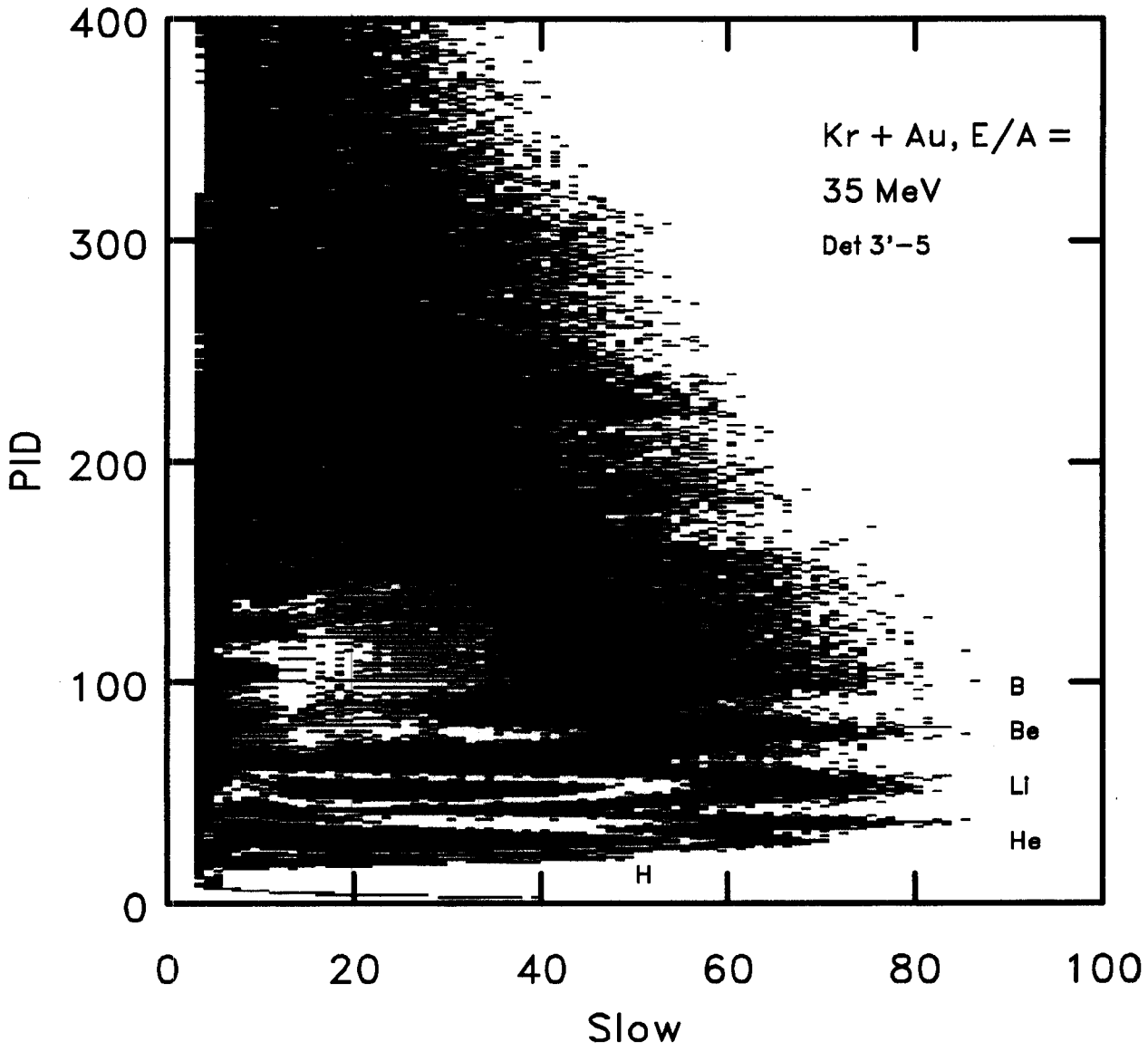

Figure 3.2a The linearized particle-identification (PID) spectrum of Fig 3.1. The charge gates were set such high statistics spectra during the data analysis and mapped to the low statistics data of figure 3.2b.

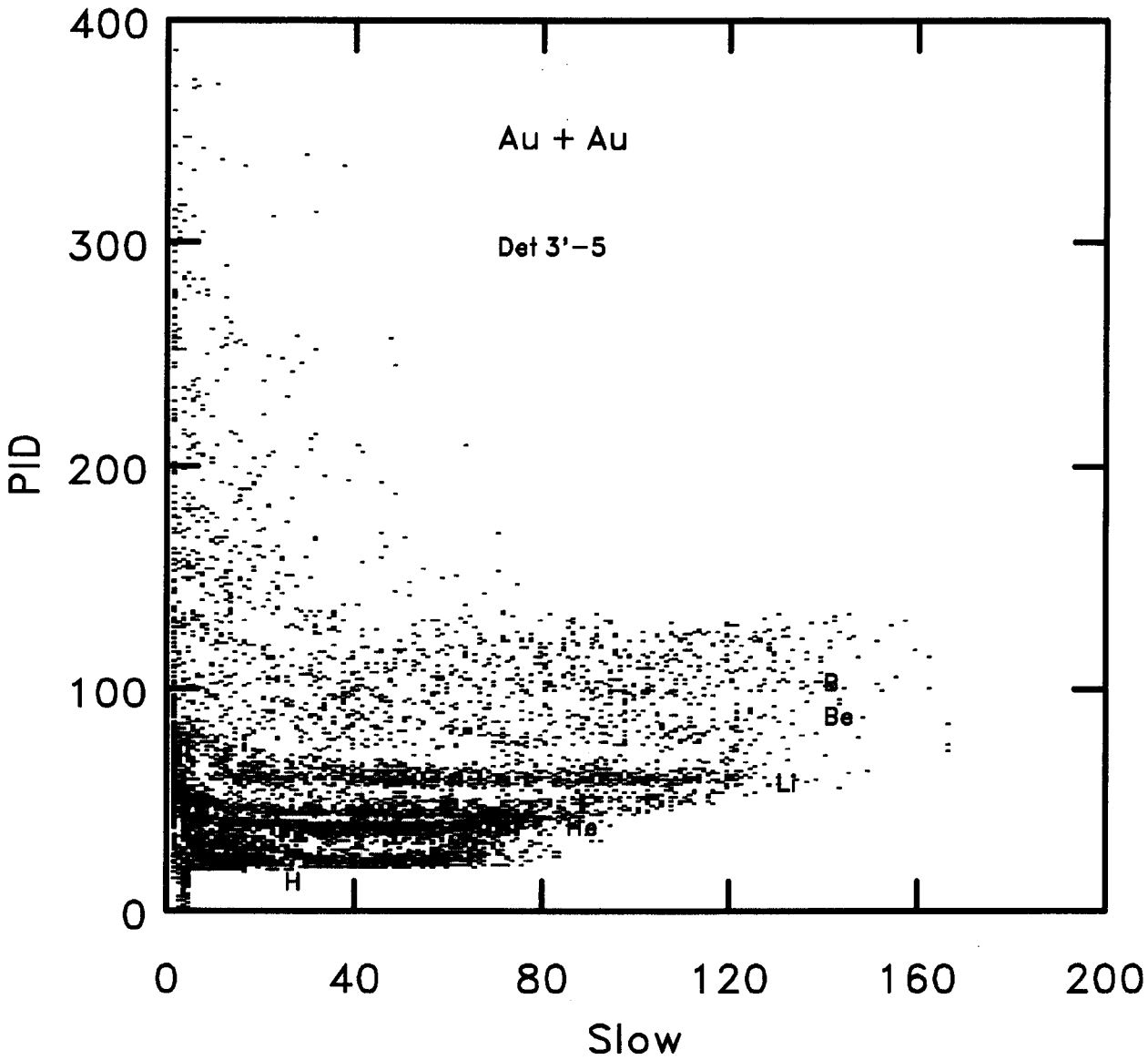

Figure 3.2b Linearized two-dimensional PID-slow spectrum obtained in the low statistics Au + Au measurement. Due to the lack of statistics, charge gates were set on the high statistics spectra shown in Fig.3.2a and mapped into the low statistics data shown here.

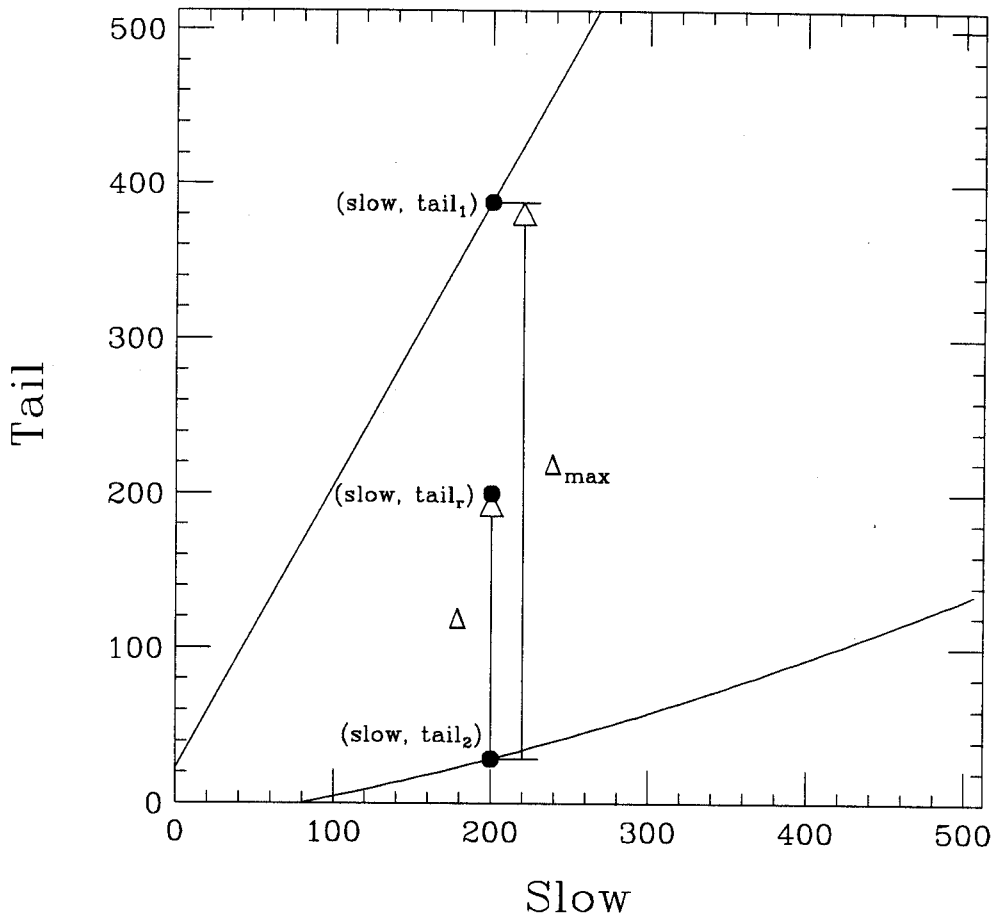

Figure 3.4 Schematic tail versus slow plot describes variables used in the construction of the PDT function.

$$\Delta = \text{Tail} - \text{Tail}_l \quad (3.5)$$

and a new parameter is defined as

$$\text{PDT} = 512 * (\Delta / \Delta_{max}) \quad (3.6)$$

Figure 3.4 illustrates the procedure used to maximize the dynamic range in the spectra in order to achieve the optimal isotope separation. The new slow channel is equal to the raw slow channel /4 + 15. An extra 15 channels were added to ensure that all particles lie within the range of the new spectra. As shown in Fig. 3.5, there is a clear separation between the Z = 3 and the light charged particles at high energies. At low energies, all particles merge in the tail versus slow spectra and must be identified through the charge identification method using the linearized PID versus slow spectra described above.

All isotopes of the hydrogen and helium particles were separated up to the punch through points. At higher energies, the punch through lines from the helium particles merge with the hydrogen punch through lines on the left side of the figure. The electronic discriminator levels were set high during the experiment to suppress low energy electrons. These discriminator settings also strongly suppress the low energy hydrogen particles leading to a sharp cutoff of the p, d, and t particle identification lines as shown in Figure 3.5. These isotope separation procedures were also applied to the Miniwall detectors.

3.2 Energy Calibration for Miniball Detectors

Since the response function of CsI(Tl) scintillation depends strongly on the atomic number, its energy and to a less extent on the mass of detected ions, several calibration measurements [Stor 58, Quin 59, Alar 86, Gong 88, Souz 90, Kim 91, Colo 92] have been performed by directly bombarding CsI(Tl) crystals with various light and heavy charged particles of known energies. These measurements indicate that the non-linearity of the light-output of the CsI(Tl) crystals becomes greater at lower energies and with higher atomic numbers of the detected particles. Above 10 MeV/A, the light output of scintillation increases more or less linearly with the energy deposition. Previous calibrations the Miniball detectors [Kim 91, Phai 93] using the elastically scattered particles have parameterized the scintillation light output **L** as

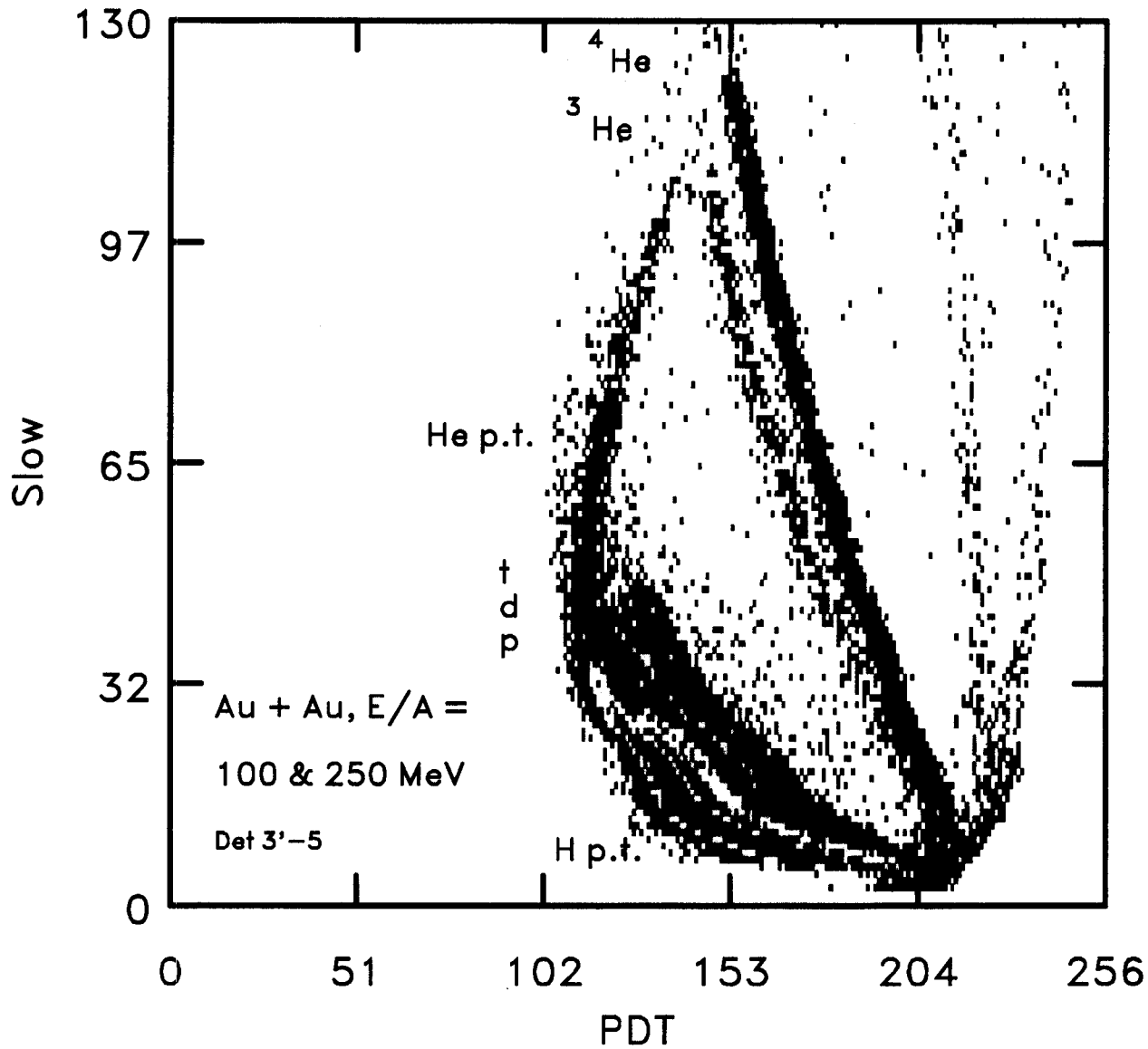

Figure 3.5 The plot shows the PDT versus slow spectrum of detector 3'-5. Good isotope separation of proton, deuteron, triton, ^{3}He and alpha is achieved.

$$L(E,Z)=\alpha(Z)E+\beta(Z)\left[e^{-\gamma(Z)E}-1.\right] \qquad (3.7)$$

where α, β and γ are charge dependent, adjustable parameters. Here, E denotes the energy deposited in the CsI crystal [Kim 91]. This functional form is consistent with previous measurements [Quin 59, Colo 92, Valt 90]. It reproduces most of the nonlinear behavior of the CsI(Tl) light output in the low energy region and the roughly linear behavior at higher energies up to E/A ~ 25 MeV.

Additional calibration points can be obtained from charged particles that punch through the 2 cm long CsI(Tl) crystal, since the energy loss for known fragments in the crystal can be calculated. A close examination of these additional high energy data points obtained at GSI and Saturne revealed that they could not be described by equation 3.7. Indeed, Eq. 3.7 overpredicts the light output by 20 ± 5% for α-particles that punch through the CsI crystal due to a saturation effect described below. Detailed examination reveals that this discrepancy correlates with the PM tube gain of the individual detectors. As there was no active amplifier in the electronics for the slow signal, the proton punch-through channel provides a measure of the PM tube gain. Correction for this gain dependent effect required a readjustment of the energy calibration procedure described below.

Correction for Saturation Effects

The nonlinear "saturation" of the energy-light relation at high energies (E/A > 30 MeV) reflects a saturation of the PM tube gain. As mentioned in Section 2.2, several factors affect the tube gain for large signals. First, the electron distribution from a large signal can significantly reduce the electron field between the last 2 dynodes, thereby reducing the amplification on D10 and the subsequent anode signal. Moreover, the charge on the capacitors in the last dynode stages can be depleted by the pulse train, thereby reducing the tube gain by lowering the voltage drops between the amplification stages, leading to reduced signal amplitude. In order to calibrate this nonlinear behavior of a large signal, we bombarded low intensity ^{6}Li, ^{12}C and ^{18}O beams directly into 10 different

Miniball detectors at incident energies ranging from E/A = 22 to 80 MeV. Figure 3.6 shows the fractional deviation of the observed light output from the light output predicted by Eq. 3.7 using calibration constants determined from lower energy signals. Here, the light output is expressed as a function of the measured QDC (charge-digit-converter) channel. The fractional deviation is defined as

$$f(ch\#) = \frac{ch\#_{norm} - L(E,Z)}{(E,Z)} \tag{3.8}$$

here ch# is the measured QDC channel for a particle with charge Z and the energy E in a particular detector. The $Ch\#_{norm}$ is the same data point renormalized by a linear transformation consistent with the measured pedestal, and one that puts the proton punch through point in channel 240.37 so that it can be compared to a light output function L(E,Z) which has been renormalized in the same fashion. In order to convert CH# into the tube gain, the measured QDC channel was corrected to take into account any differences in the splitter ratios discussed in Section 2.5. For ^{12}C fragments, the saturation effect was parameterized by the straight line shown in the upper panel of Figure 3.6. The same fit also approximates the ^{6}Li data (shown in the bottom panel of Fig. 3.6) By combining calibrations obtained in previous Miniball experiments [Kim 91, Peas 94], a similar description of the saturation effects for ^{4}He, ^{6}Li, ^{10}B, ^{12}C, ^{12}N, ^{16}O and ^{20}Ne ions was achieved.

Since the fractional deviation varies roughly linearly with the measured QDC channel, i.e., to the amount of light passing through the PM tube, one can obtain the model-dependent corrected channel by rewriting Eq. 3.8 into a different form:

$$f(ch\#) = \frac{ch\#_{norm} - ch\#_{corrected}}{ch\#_{corrected}}. \tag{3.9}$$

Then, one can write the corrected channel as

$$ch\#_{corrected} = \frac{ch\#_{norm}}{1 + f(ch\#)}. \tag{3.10}$$

Since $f(ch\#) = f_c \bullet ch\#$ and f_c is assumed to be independent of the charge and the energy of the detected particles, Eq. 3.10 can be written as

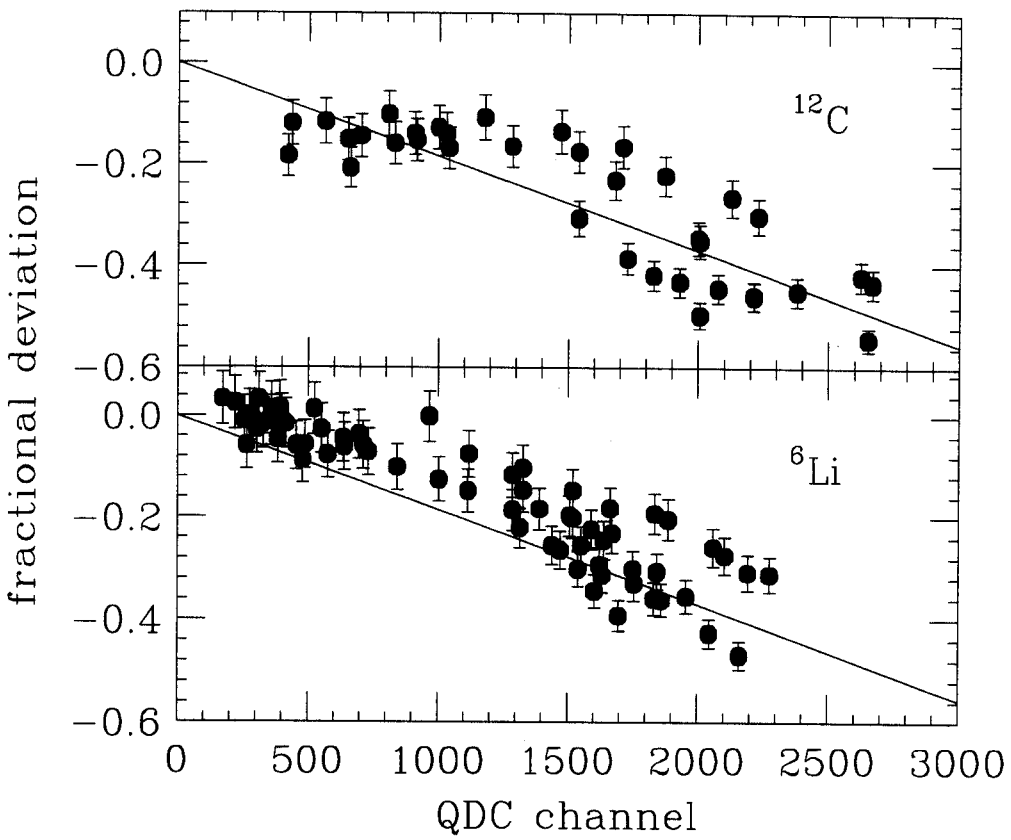

Figure 3.6 Fractional deviations of the light output of Miniball detectors as defined in equation 3.9, as a function of the normalized QDC channel. The upper (lower) panel shows the results for ^{12}C(^{6}Li) fragments, respectively.

$$ch\#_{corrected} = \frac{ch\#_{norm}}{1 + f_c \bullet ch\#} \tag{3.11}$$

The spreading of the data points from 10 different Miniball detectors is of the order 10-15 % as indicated in Fig. 3.6. The origin of this spread is unknown, but may be related to the accuracy of some of the electronic components used in the PM voltage divider, or the differences in the doping of individual crystals, or the internal tolerances of some of the PM tubes. It represents a systematic error associated with using a universal correction without specific modifications for the unique characteristics of each Miniball detector.

To demonstrate this correction effect, we compare the corrected and uncorrected light outputs of a specific detector for ^{4}He and ^{12}C fragments. As seen from Fig. 3.7, this correction becomes more important where there is a higher amount of light passing through the PM tube, i.e., for larger QDC channels. While the 250 MeV ^{12}C data points are only corrected by about 10 %, the correction for the 300 MeV ^{4}He data points is on the order of 30-40 %.

The parameters α, β and γ in Eq. 3.7 are charge dependent. Following the method proposed by Colonna et al. [Colo 92], we parameterize this charge dependence as follows:

$$\alpha(z) = a_1 + a_2 \bullet e^{-a_3 Z},$$

$$\beta(z) = b_1 - b_2 \bullet e^{-b_3 Z}, \quad \text{and} \tag{3.12}$$

$$\gamma(z) = c_1 + c_2 \bullet e^{-c_3 Z}$$

The fractional saturation constant f_c in Eq. 3.11 was also treated as a fit parameter in the overall calibration. The α, β and γ parameters for light particles ($Z \leq 2$) cannot be fitted well by the smooth function and are treated as three additional parameters. A total of 13 parameters have been fitted by a χ^2 minimization procedure using all of the existing Miniball calibration data. All data points have been appropriately normalized to correct for differences in the splitter ratios. The values of a_i, b_i and c_i are listed in Table 3.1 for fragments with Z/A = 0.5.

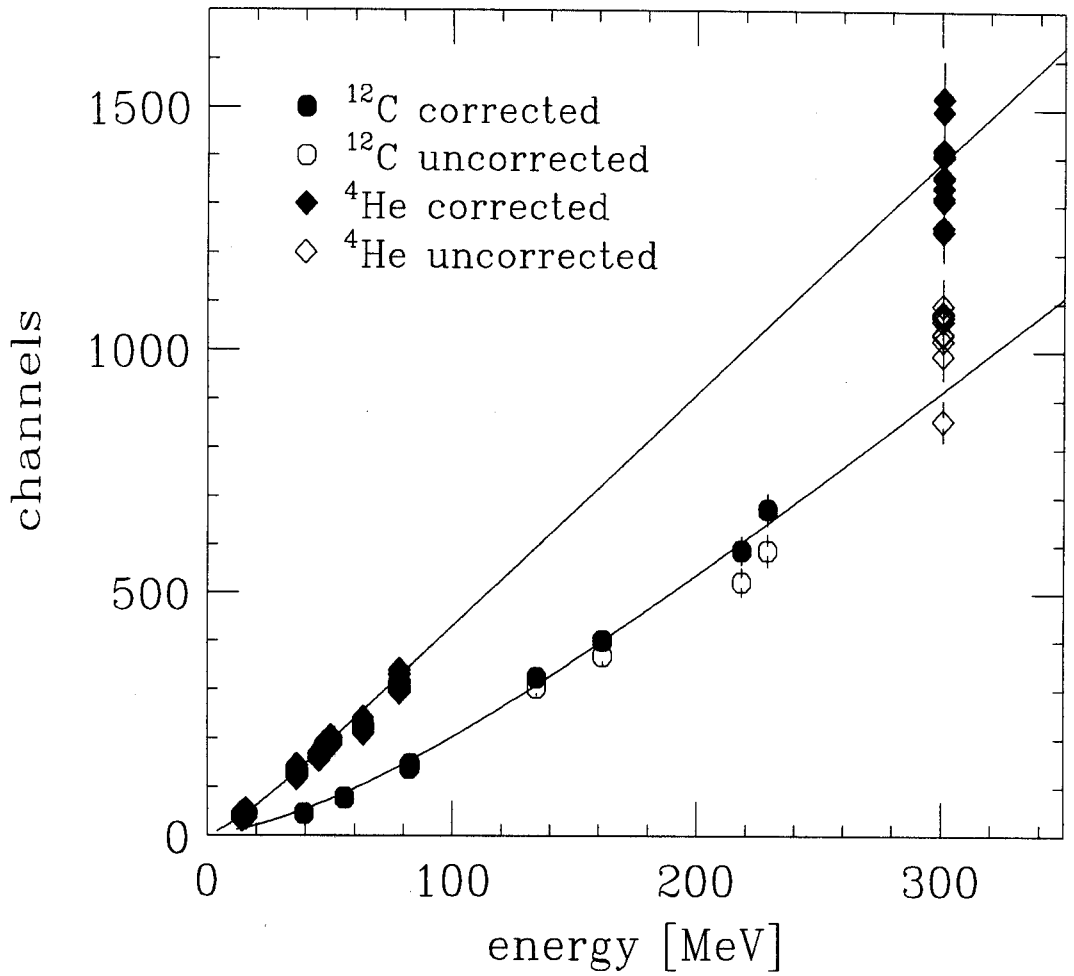

Figure 3.7 Calibration curve for ^{4}He and ^{12}C fragments (solid points) including the saturation corrections. The open symbols show the uncorrected data points.

Table 3.1 The values of a_i, b_i and c_i in the set of functions (Eq. 3.12) for energy calibrations

$\chi^2/n = 3.27$	i=1	i=2	i=3
a_i	0.4142	4.995	7.824E-2
b_i	299.7	5.039E-3	1.967E-4
c_i	1.339E-2	5.925E-3	3.846

In order to compare this data to previous calibration curves, the curves and data were normalized to place the 200 MeV ^{12}C point at channel 511. The fit to the saturation correction factor in Eq. 3.11 for the Miniball detectors yielded $f_c = 1.7 \times 10^{-4}$.

An additional constraint is applied to the fit that keeps the calibration curves for different charges from crossing. For clarity, multiple data points for the same energy and fragment charge were averaged to create Fig. 3.7; the spread of the calibration data is indicated by the error bars. For energies larger than 30 MeV per nucleon, the calibration is accurate to 10-15% and this accuracy improved to 5-10% at lower energies. The insert of Fig. 3.8 shows the fit for various fragments more clearly at lower energies. While most of the fragments follow the predicted systematic trends, both ^{6}Li and ^{10}B particles (the crosses) seem to deviate from the calculated curves. As this data has been taken from various experiments and analyzed by different people at different times, a more comprehensive set of data for these two elements, taken under more controlled circumstances, would be desirable to understand the observed deviation and to establish a systematic trend.

Even though the Miniball array contains CsI crystals from different manufacturers, all CsI detectors have a similar light output. The final energy calibration for a specific detector has a 10-15% uncertainty for particles with energies above E/A = 30 MeV. The

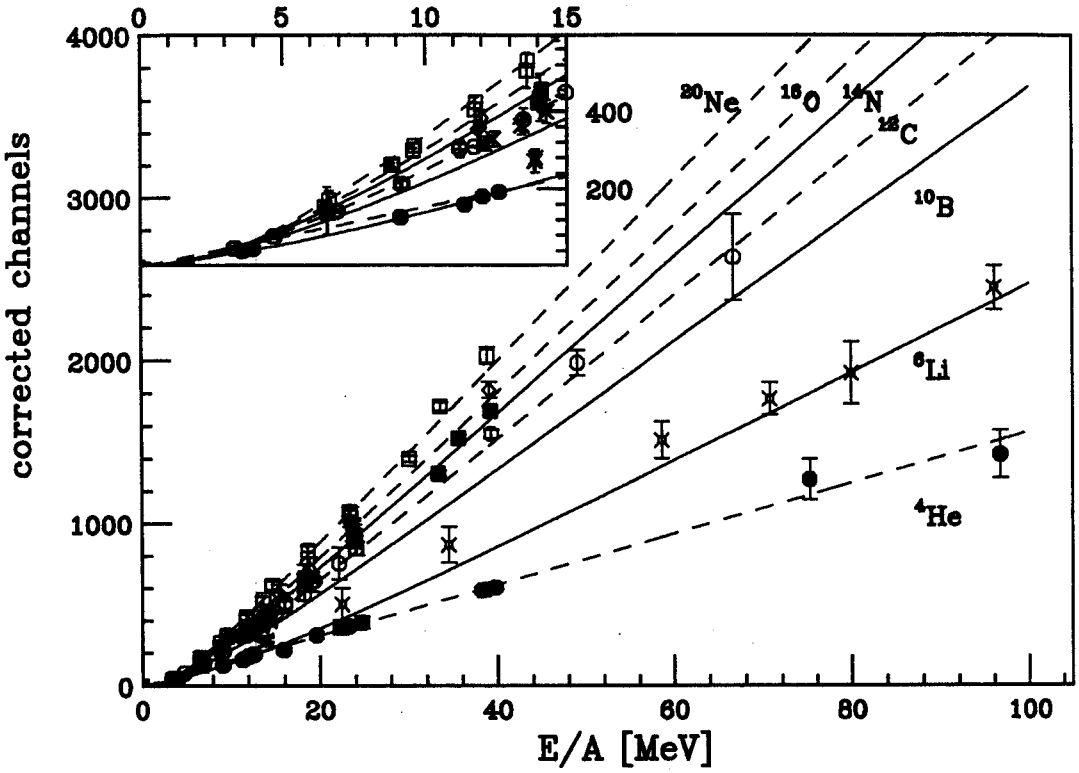

Figure 3.8 Calibration data for ^{4}He (solid circles), ^{6}Li (open fancy crosses), ^{10}B (crosses), ^{12}C (open circles), ^{14}N (solid squares), ^{16}O (open diamonds) and ^{20}Ne (open squares). The lines are fits to the data (solid lines for odd charge elements and dashed lines for even charge elements).

effect of the fluctuations between the calibrations of different detectors are reduced when the data for the different detectors in a ring are combined to obtain the energy spectra.

3.3 Particle Identification of Catania Hodoscope

Each telescope in the hodoscope consists of a 300 μm Silicon detector backed by a 6 cm long CsI(Tl) crystal. The signal of each Silicon detector is proportional to the energy loss in that detector and is designated as "DE". The signal from the CsI(Tl) is correspondingly designated as "E". The charge lines in the DE-E two-dimensional spectra are approximate hyperbolae, as shown in Fig. 3.9, in accordance with the energy loss predictions of the Bethe-Bloch Equation [Goul 69, Knol 79]. While the operation of Silicon CsI(Tl) energy loss telescopes is in principle straightforward, non-linearities in the electronics and some difficulties in calibration prevented the full utilization of this device. Therefore, it was simply used to determine the number of intermediate mass fragments emitted into the angular range subtended by the Catania hodoscope.

Since the punch though energies in the 6 cm CsI crystals of the Catania Hodoscope are around 200 to 250 MeV/A for intermediate mass fragments, a lot of IMFs emitted at incident energy of E/A = 400 MeV have energies higher than 200 MeV/A. Such energetic IMFs can punch through the detectors and be indistinguishable from lighter charged particles that also punch through these detectors. This is illustrated in Fig. 3.10. Therefore, sufficiently energetic punch-through Lithium and Beryllium fragments could not be separated from punch-through Helium particles, leading to an additional upper threshold for detecting these IMFs. The cut used in the analysis for suppressing light particles is shown as the line in Fig. 3.10. It removes punch through particles and also suppress double hits by the α particles. The effective upper thresholds per nucleon for the IMFs introduced by this procedure is approximately $E_{cut}/A \sim 180. + 80.x(Z-3)^2$ Mev where the Z is the charge of detected particle. To simulate the number of emitted IMFs via theoretical calculation, these punch-through energy cutoffs were also included in the filter routines for the experimental acceptance.

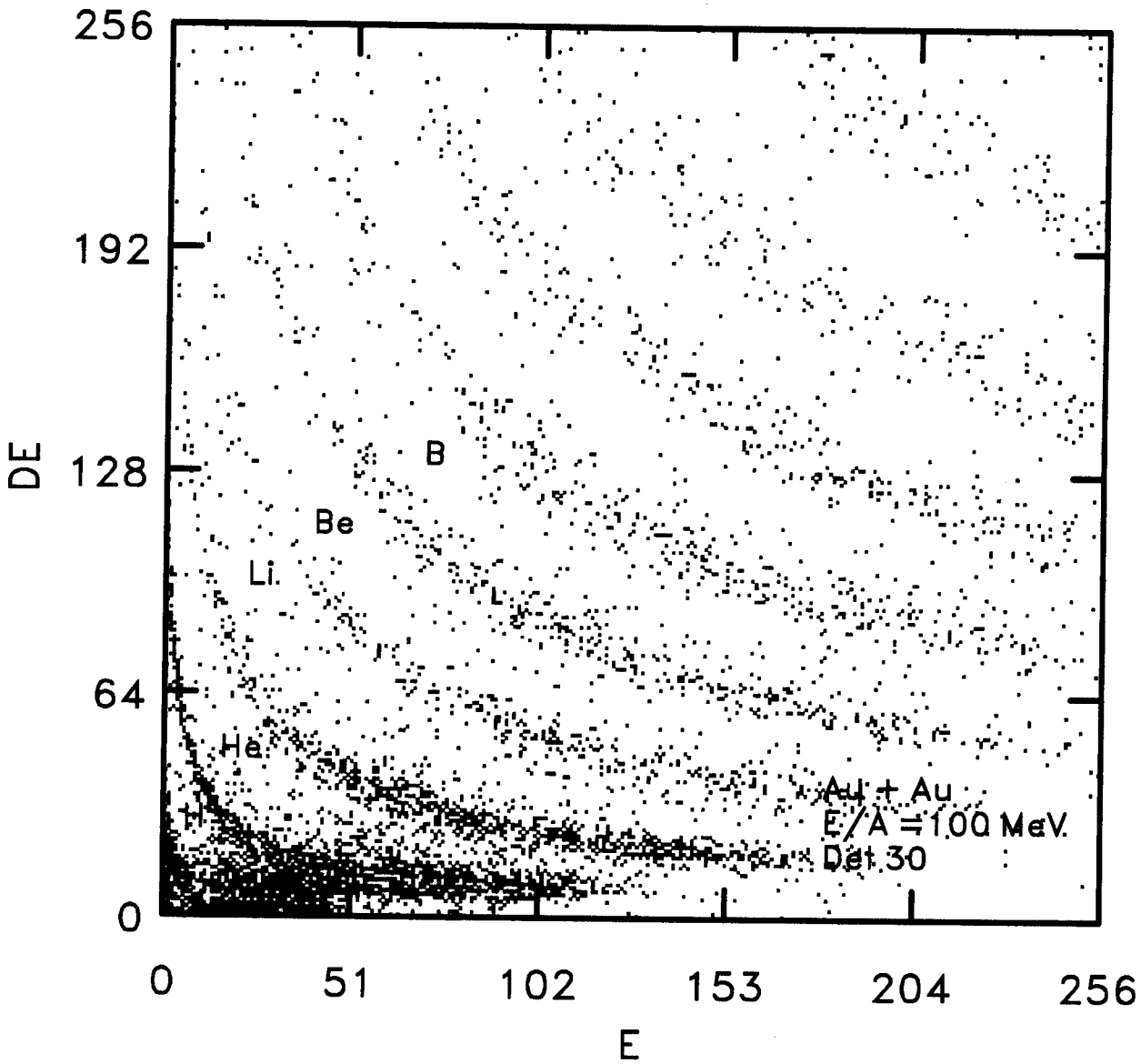

Figure 3.9 DE (signal of Si) versus E (signal of CsI) for the Catania hodoscope is plotted for detector 30 at E/A = 100 MeV collisions.

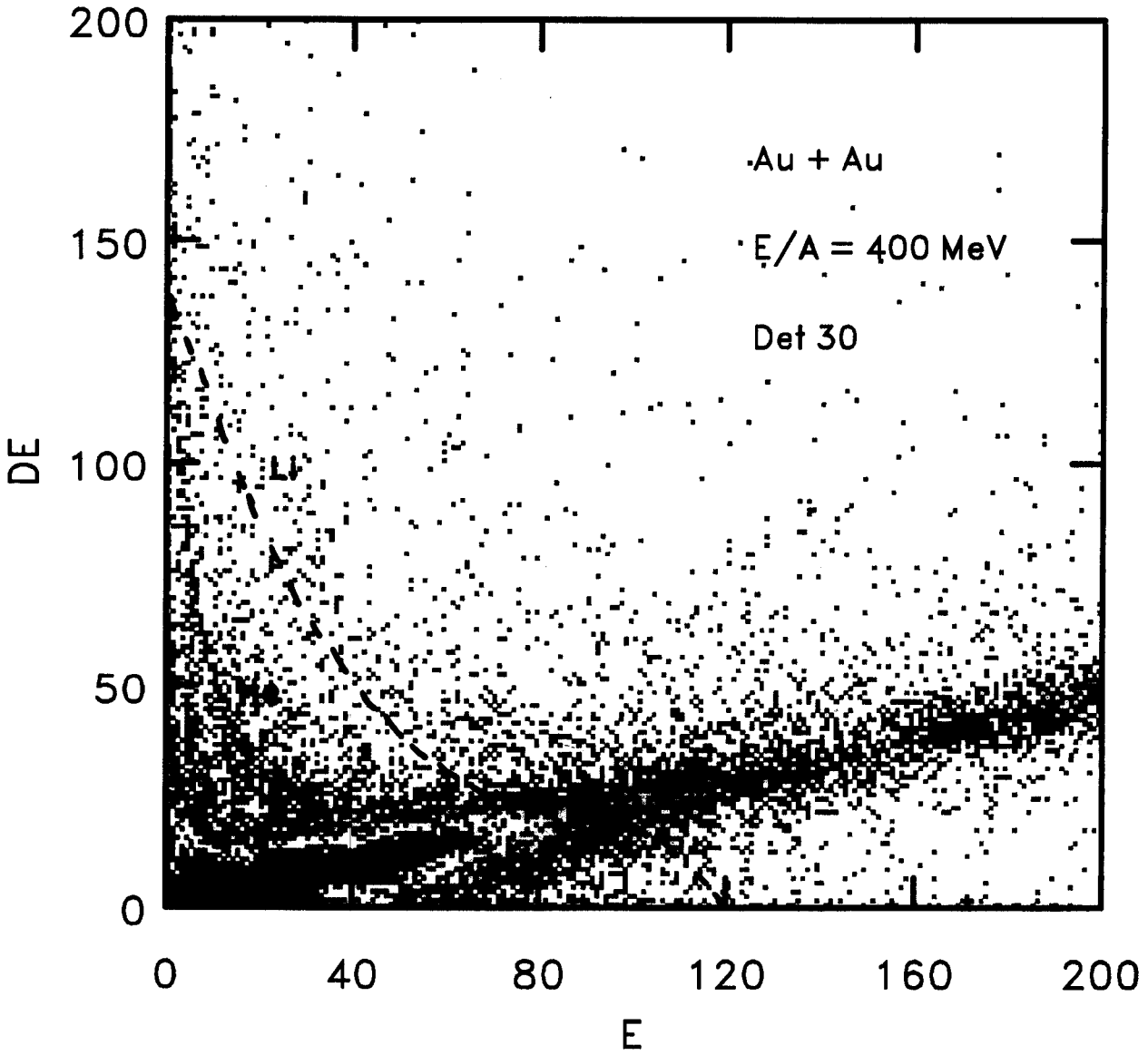

Figure 3.10 DE (signal of Si) versus E (signal of CsI) for the Catania hodoscope is plotted for detector 30 at E/A = 400 MeV collisions.

3.4 Particle Identification of the Aladin ToF Wall

Each of the plastic scintillators of the ToF wall were read out by two PM tubes at the ends of the scintillator. The sum of the two signals from the PM tubes is proportional to the light output of the scintillators; the light output is proportional to the square of the charge by the Bethe Bloch equation and roughly inversely proportional to the square of the velocities of the detected particles. The flight time of these particles could also be measured with a resolution of 160 ps if a start scintillator is put into the beam line. Unfortunately, such a start detector could not be used in this experiment because it would be thicker than the target. Therefore, the time of arrival of Hydrogen and Helium particles in the Miniball was used to generate a start signal, given an overall of resolution of 500 ps. In Fig. 3.11, the resulting flight time is plotted versus the light output of particles detected in the front 100 scintillators of the ToF wall. Particle identification was achieved in this 2-D spectrum by gating on the indicated charge lines. Similar methods were applied to both the front and back ToF walls. A tracking procedure was applied to avoid double counting the particles which were detected in more than one scintillator.

The ratio of the two PM signals from each scintillator gave the vertical position of detected particles with a position resolution of about 1 cm. Despite knowing the positions of particles detected in the ToF wall, the polar and azimuthal angles of the detected particle could not be accurately determined without knowing the trajectories. Therefore, the possible trajectories were reconstructed using the flight time, the x and y positions, and the charge of detected particles, assuming masses consistent with simulated isotope distributions which reproduced the isotope distribution measured in previous experiments with the Aladin spectrometer. This allowed approximate polar and azimuthal angle reconstruction. The acceptance of the Aladin spectrometer was modeled via GEANT simulations, and this acceptance was incorporated into the filter routine.

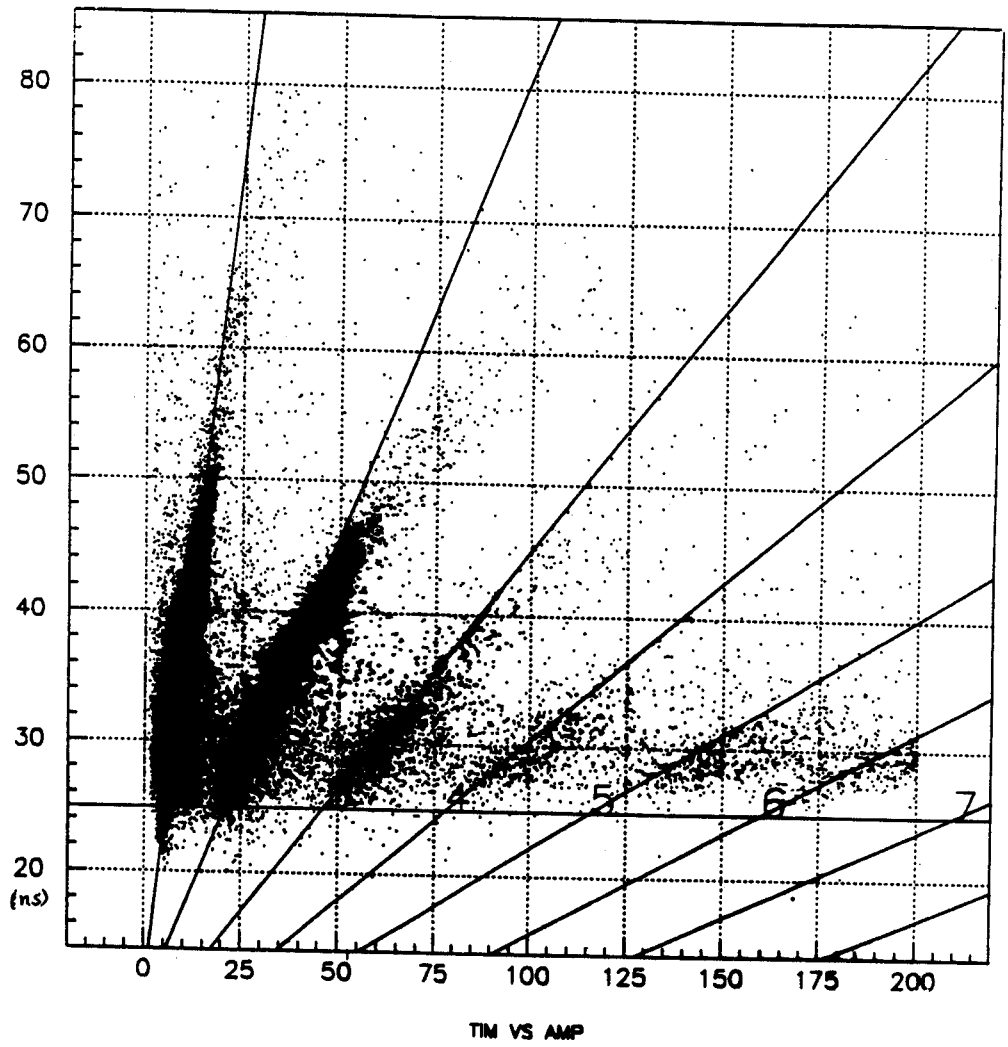

Figure 3.11 The flight time is plotted versus the light output of particles detected in the front 100 scintillators of the ToF wall which are used for the particle identification. The charge lines are indicated by the straight lines.

Chapter 4

Experimental Results and Model Comparisons

In this chapter, the principal experimental results of the dissertation are presented. Since little can be learned about the thermodynamics of a nuclear collision without knowing something about the impact parameter of the collision, this chapter begins with a description of techniques used for impact parameter selection. This is followed by experimental evidence for the onset of nuclear vaporization in central collisions. At the highest incident energy, the complimentary nature of the experimental setup allows one to extrapolate to a "threshold-less" setup. Such an extrapolation is presented in Section 4.3. The final sections of this chapter addresses the experimental information regarding the dynamics of the multifragment breakup.

4.1 Reaction filters: Impact Parameter Selection

Information about the impact parameter has been obtained via measurements of the total charge particle multiplicity N_c [Kim 91, Phai 92], the total transverse kinetic energy E_t [Wils 90, Tsan 91, Phai 93], the total charge Z_{bound} contained in bound remnants of the projectile [Hube 91], and the participant proton multiplicity [Doss 85, Gust 88].

In the present work, the total charged particle multiplicity N_c includes all the charged particles detected by the Miniball/Miniwall array, even if they were not identified. Heavy fragments stopped in the scintillator foils are included in N_c. Multiple hits in a single detector module are counted as single hits, even if they can be clearly identified as double hits (such as double hits by two α-particles which can give rise to a single particle identification line). The left panel of Fig. 4.1.1 shows the normalized charged particle multiplicity distribution detected in the Miniball/wall array for E/A = 100, 250 and 400 MeV. Similar to other measurements [Phai 92], the normalized probability distributions exhibit a rather structureless plateau and a near-exponential fall-off at the highest multiplicities. The probability where one observes the exponential fall-off increases from N_c = 55 to 75 as the beam energy is increased from E/A=100 to 400 MeV.

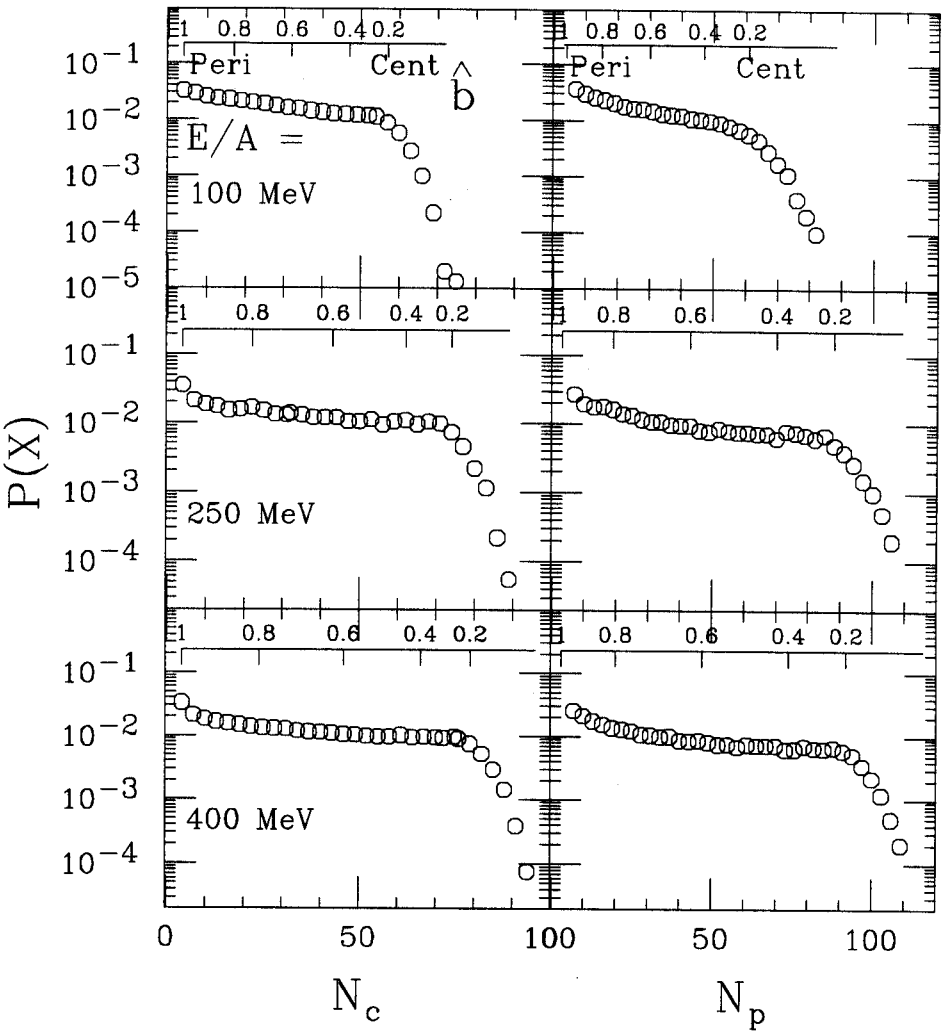

Fig. 4.1.1 Normalized probability distributions for the charged particle multiplicity N_c (left side), and the participant proton multiplicity N_p (right side) for E/A=100, 250 and 400 MeV. The reduced impact parameters $\hat{b}$ are indicated at the top of each panel.

The participant proton multiplicity N_p is defined as the sum of the true proton multiplicity and the number of participant protons bound in light Hydrogen and Helium isotopes. In the present work, the participant proton multiplicity is calculated from the yields of these particles detected at $E_{lab}/A > 15$ MeV in the Miniball/Miniwall. Normalized probability distributions for N_p, shown in the right hand panel of Fig. 4.1.1, are very similar to the distributions for N_c.

Z_{bound} is defined in this experiment as the sum of the charges of fragments with $Z \geq 2$ detected in the forward Aladin spectrometer [Hube 91]; most of these particles are emitted from the projectile spectators. Z_{bound} depends on the disassembly of the projectile spectator which will be strongly influenced by the energy deposited in the projectile spectator nucleus during the initial stage of the reaction [Ogil 91, Hube 91]. The normalized probability distributions for Z_{bound} at the three energies are plotted in the right hand panel of Figure 4.1.2. The probability distribution is nearly constant before dropping off exponentially above $Z_{bound} > 70$. For reactions at E/A = 400 MeV, the Aladin detection efficiency for fragments emitted within its angular acceptance and with $Z > 3$ and $y > 0.5$ y_{beam}, is nearly 100%. For E/A=100 MeV, on the other hand, the detection efficiency in the Aladin spectrometer for heavy ions of $Z > 40$ rapidly vanishes, because such fragments may stop in the 50 mg/cm^2 Kevlar entrance foils of the MUSIC chamber. Thus, Z_{bound} data at E/A = 100 MeV does not provide useful impact parameter information. The statistics of the measurements at E/A = 250 MeV are insufficient to determine the suitability of the Z_{bound} data for impact parameter determination.

Most of the detected particles move at much less than the speed of light; therefore, the total transverse kinetic energy E_t is calculated nonrelativistically [Phai 93].

$$E_t = \sum_i E_i \sin^2 \theta_i = \sum_i \frac{(p_i \sin \theta_i)^2}{2m_i} \qquad (4.1.1)$$

Here m_i, E_i, p_i and θ_i denote the rest mass, kinetic energy, momentum, and polar angle of the i^{th} emitted particle in the laboratory frame. For particles that punch-through the CsI crystals, there are no energy calibrations. Thus E_t does not include any of the punch through particles. The normalized probability distributions for E_t at E/A = 100, 250 and

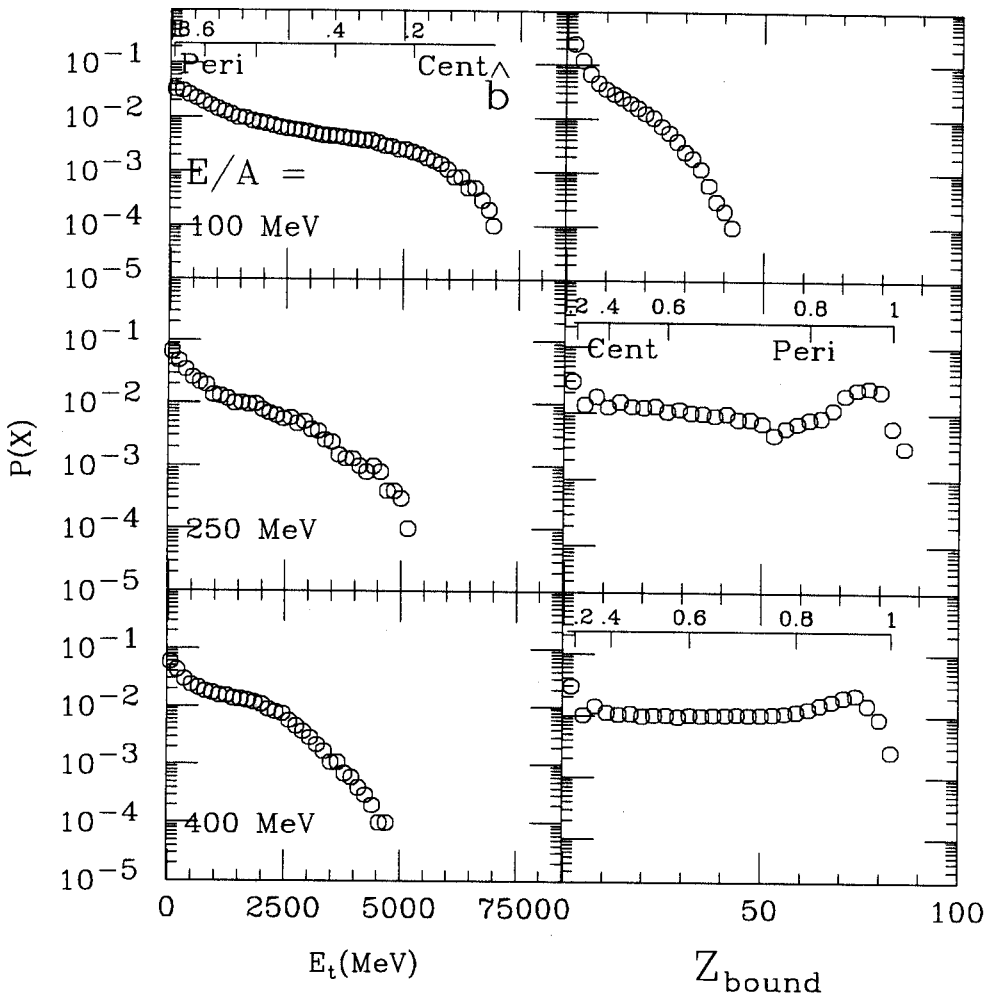

Fig. 4.1.2 Normalized probability distributions for the transverse kinetic energy E_t (left side) and the sum of bound charges Z_{bound} (right side) for E/A=100, 250 and 400 MeV. The reduced impact parameters $\hat{b}$ are indicated at the top of each panel when they can be reasonably assigned.

400 MeV are shown in the left hand panels of Figure 4.1.2. Since light particles punching through the CsI can not be included in E_t, the suitability of the current detection configuration for reconstructing the impact parameter using E_t at E/A = 250 and 400 MeV is questionable.

To establish an impact parameter scale at these incident energies, the geometrical prescription proposed by Cavata [Cava 90] has been adopted. For each quantity, N_c, E_t, Z_{bound} and N_p, we assume a monatomic dependence upon the impact parameter and define the reduced impact parameter scale via

$$\hat{b}(X) = \frac{b(X)}{b_{max}} = \left[\int_X^{\infty} P(X')dX'\right]^{1/2} / \left[\int_{X(b_{max})}^{\infty} P(X')dX'\right]^{1/2} \qquad (4.1.2)$$

where $X = N_c$, E_t and N_p , and

$$\hat{b}(X) = \frac{b(X)}{b_{max}} = \left[\int_0^{X} P(X')dX'\right]^{1/2} / \left[\int_0^{X(b_{max})} P(X')dX'\right]^{1/2} \qquad (4.1.3)$$

For impact parameter selection using Z_{bound}, P(X') is the normalized probability distribution for the measured quantity and b_{max} is a maximum impact parameter at which the detected charged particles multiplicity equals the minimum bias threshold. For this set of experiment $b = b_{max}$ at $\langle N_C \rangle = 4$. The corresponding $\hat{b}$ scales are shown near the top of each normalized probability distribution plotted in Figure 4.1.1-2. Neglecting fluctuations, the reduced impact parameter scale ranges from $\hat{b} = 1$ for glancing collisions to $\hat{b} = 0$ for head-on collisions.

The quantitative relationship between the reduced impact parameters $\hat{b}(x)$ and the measured observable X where X= N_c, Et, Z_{bound} and N_p, is shown in Figure 4.1.3 for three incident energies, E/A = 100 (dotted lines), 250 (dashed lines), and 400 MeV (solid lines). As punch-through particles were not included in E_t, only data for E/A=100 MeV is shown in the lower left panel. Due to a low detection efficiency in the ToF wall at E/A = 100 MeV and problems with statistics at E/A=250 MeV, only the data for E/A=400 MeV is shown in the lower right panel. Based on the acceptance of the device, one expects N_c, N_p and Z_{bound} to provide reasonable impact parameter information at E/A = 400 MeV, and N_c,

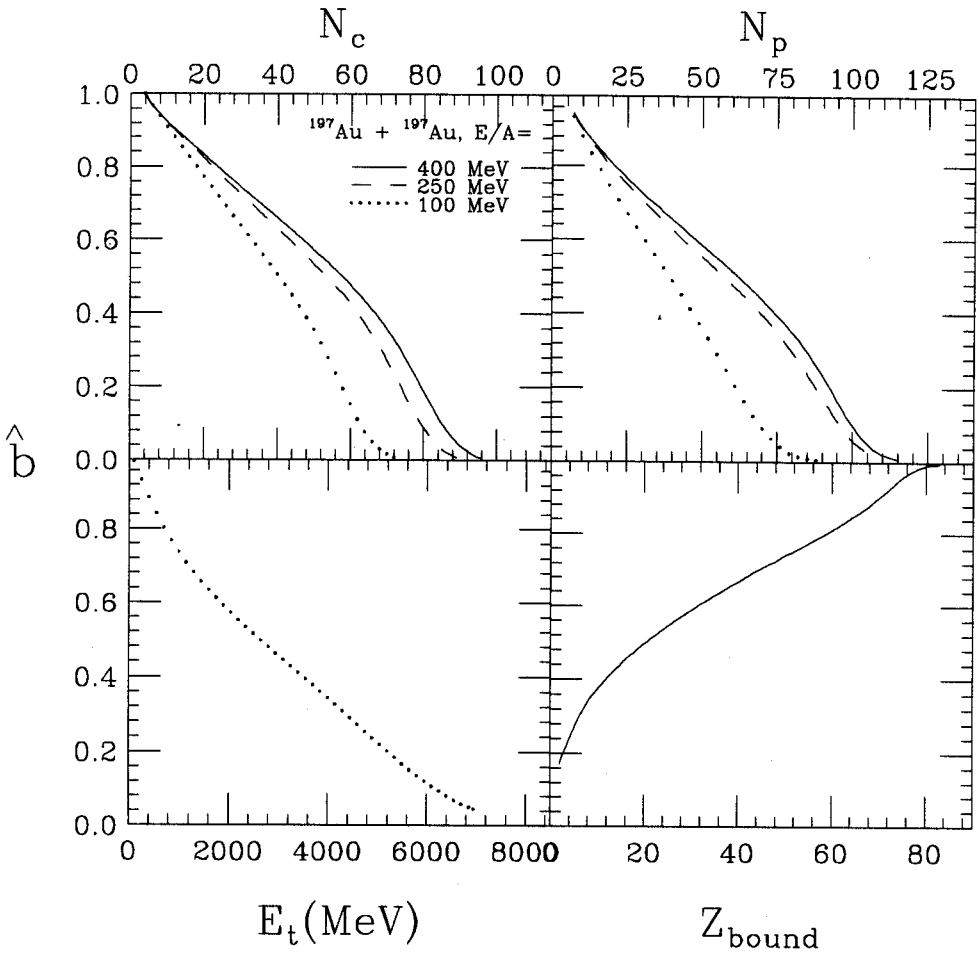

Fig. 4.1.3 Reduced impact parameters $\hat{b}$ extracted from the measured observables X = N_c, N_p, E_t and Z_{bound} by using Eq. 4.1.2-3. Each panel shows the relationship between the extracted variable X and $\hat{b}$; the dotted, dashed and solid curves represent the relations extracted at E/A=100, 250 and 400 MeV respectively.

N_p and E_t to provided reasonable information at E/A = 100 MeV. For E/A = 250 MeV, N_c and N_p are the experimental observables available for constructing the impact parameter.

Figure 4.1.4 shows the measured correlation between the impact parameters deduced from those observable at the two extreme incident energies, E/A = 100 and 400 MeV, where adequate statistics were available. As expected, N_c is strongly correlated to N_p for both incident energies. N_c is correlated to E_t for E/A = 100 MeV. It is a general fact that N_c is anti-correlated with Z_{bound} for E/A = 400 MeV collisions; N_c is correlated to the multiplicity of particles emitted from either the target spectator or the participant region, while Z_{bound} reflects survive bound protons of the projectile spectator residue. Previous comparisons of these different observables by Phair et al. [Phai 92, Phai 93] suggest a close relationship between the various impact parameter scales with significant deviations occurring mainly at small and large impact parameters. A significant loss in sensitivity is also expected whenever the eventwise fluctuations at fixed impact parameters exceed the variations of the mean value of the relevant observables with the impact parameter. For simplicity, we chose the reduced impact parameter constructed from N_c as the primary source of the impact parameter selection for the current data analyses. A two-dimensional cut on two different impact parameter gates has not been used to place more restrictive gates on the event selection, even though that might lead to greater precision in the impact parameter selection.

Using theoretical calculations and folding in the experimental acceptance, the normalized probability distributions for the charge particle multiplicity can be used to test the reduced impact parameters that were experimentally assigned. For this purpose, we analyzed QMD molecular dynamics model calculations as if they were data, and compared the impact parameters deduced from the charged particle multiplicity to the actual impact parameters where calculations were performed. The upper panel in Figure 4.1.5 shows the impact parameter dependence of the mean charged particle multiplicity. The lower panel compares the deduced and actual impact parameters. Typical FWHM deviations of about 1 fm between the actual and deduced impact parameters are observed, indicating that reasonably

accurate impact parameter selector can be achieved using N_c as the relevant observable.

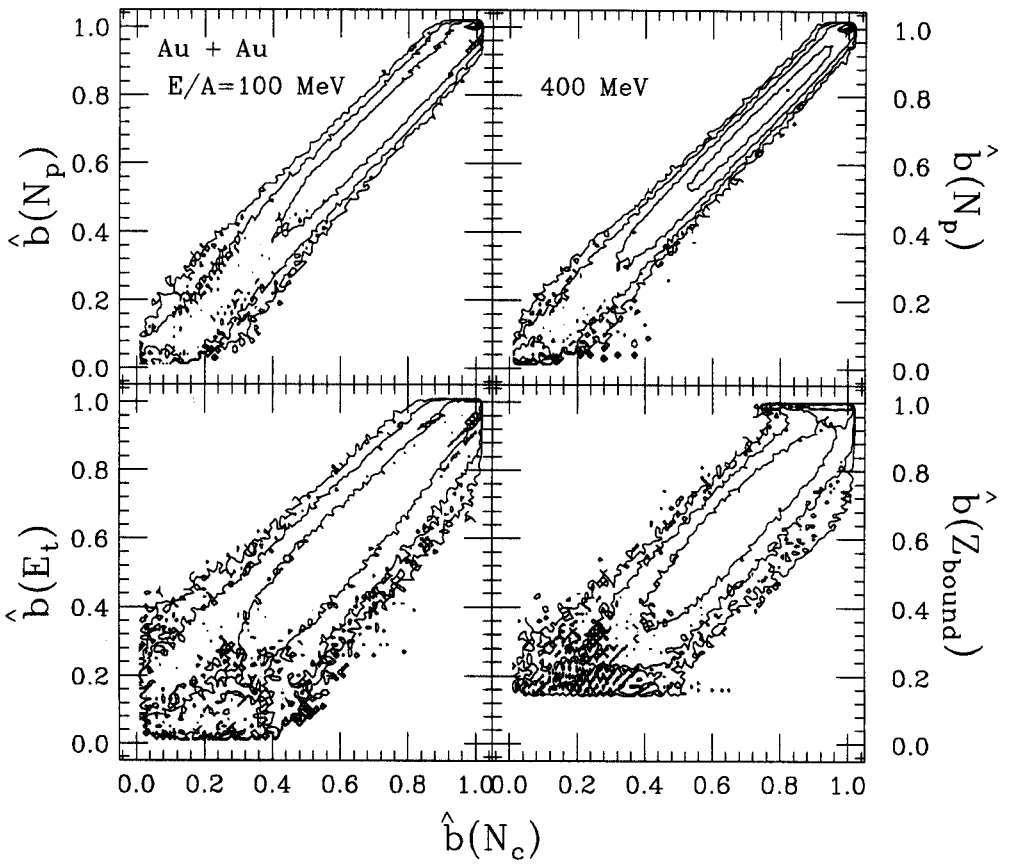

Fig. 4.1.4 Correlation between the reduced impact parameters reconstructed from the charged particle multiplicity N_c , transverse kinetic energy E_t, participant proton multiplicity N_p, and the sum charge of spectator nucleon Z_{bound} for E/A=100 and 400 MeV. Adjacent contours differ by a factors of 5.

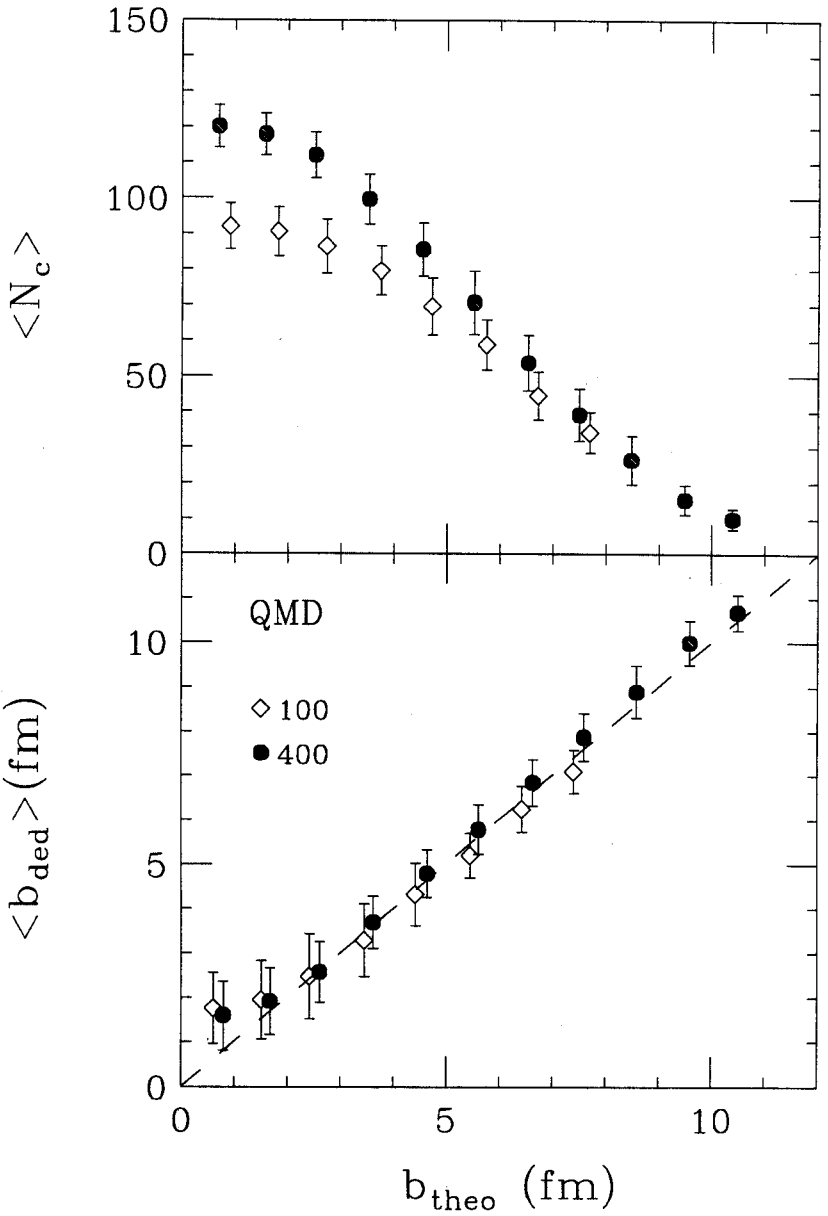

Fig 4.1.5 Mean charge particle multiplicities $<N_c>$ obtained from the QMD model and filtered through the experimental acceptance at E/A = 100 and 400 MeV are shown in the top panel. The mean deduced impact parameter $<b_{ded}>$ are plotted in bottom panel. The b_{theo} is the impact parameter of which the QMD calculations were performed.

4.2 Onset of Nuclear Vaporization at $^{197}Au + ^{197}Au$ collisions

The incident energy dependence of multifragmentation in central collisions was explored for $^{36}Ar + ^{197}Au$ collisions between E/A = 35 and 110 MeV [deSo 91]. These investigations reveal fragment multiplicities which increase monotonically with incident energy. Over a broader range of incident energies, however, models such as the Quantum Molecular Dynamics model (QMD) predict a maximum in the fragment multiplicity for central collisions with symmetric system at energies of the order of 100 A MeV [Peil 89], and decreasing multiplicity thereafter, consistent with the onset of nuclear vaporization [Cser 86, Bert 83]. Until recently [Peas 94, Tsan 93], the availability of data to test such predictions was very limited. Measurements of central Au + Au collisions at E/A = 150 and 200 MeV [Doss 87, Alar 92] exhibited multifragmentation, but did not measure the incident energy dependence of the phenomenon. Measurements of multifragmentation in peripheral collisions at higher incident energies [Ogil 91, Hube 92] suggested declining fragment multiplicities with increasing impact parameters, but the measurement lacked sufficient phase space coverage to draw definitive conclusions about the central collisions.

Figure 4.2.1 shows the correlation between $\langle N_{IMF} \rangle$ the mean IMF multiplicity measured in the combined array and N_c the total charge particle multiplicity detected in the Miniball/Miniwall array at the three incident energies. The observed dependence of $\langle N_{IMF} \rangle$ upon N_c reflects the dependence of both quantities upon the impact parameter.

Figure 4.2.2 shows the mean IMF multiplicities as a function of the reduced impact parameter $\hat{b}$, obtained using Eq. 4.1.2 for $X = N_c$. At E/A = 100 MeV, $\langle N_{IMF} \rangle$ is the largest for small impact parameters, consistent with increased multifragmentation for collisions with increased compression and excitation energy. With increasing incident energy, the multiplicities observed in central collisions decrease, however, reflecting the onset of nuclear vaporization.

To demonstrate that the decreasing IMF multiplicities observed in central collisions at E/A = 400 MeV did not arise from detection inefficiencies of the experimental apparatus, the mean total charge , $\langle Z_{tot} \rangle$, is shown in Fig. 4.2.3 for the two extreme incident energies. At both incident energies, the measured mean total charge is a monotonic function of the charged particle multiplicity. The windows of the MUSIC ion

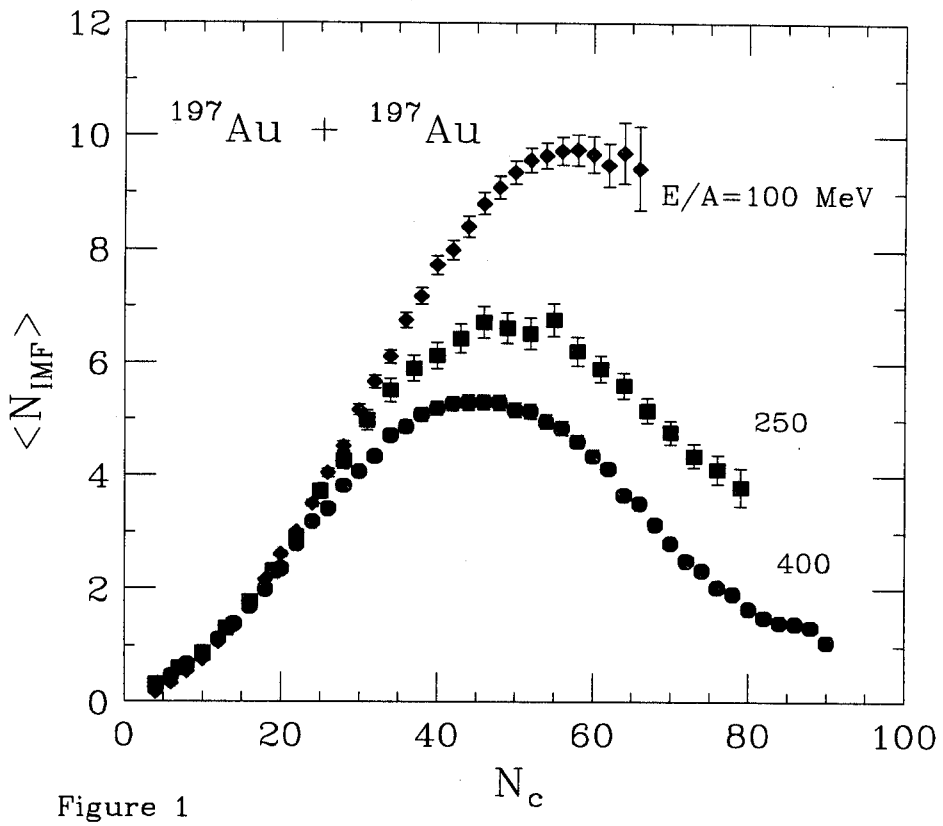

Figure 1

Fig. 4.2.1 Correlation between $<N_{IMF}>$ the observed mean fragment multiplicity and N_c the observed multiplicity of charged particles detected in the Miniball/wall. The measured quantities have not been corrected for the energy and angle dependent detection efficiency of the experimental apparatus.

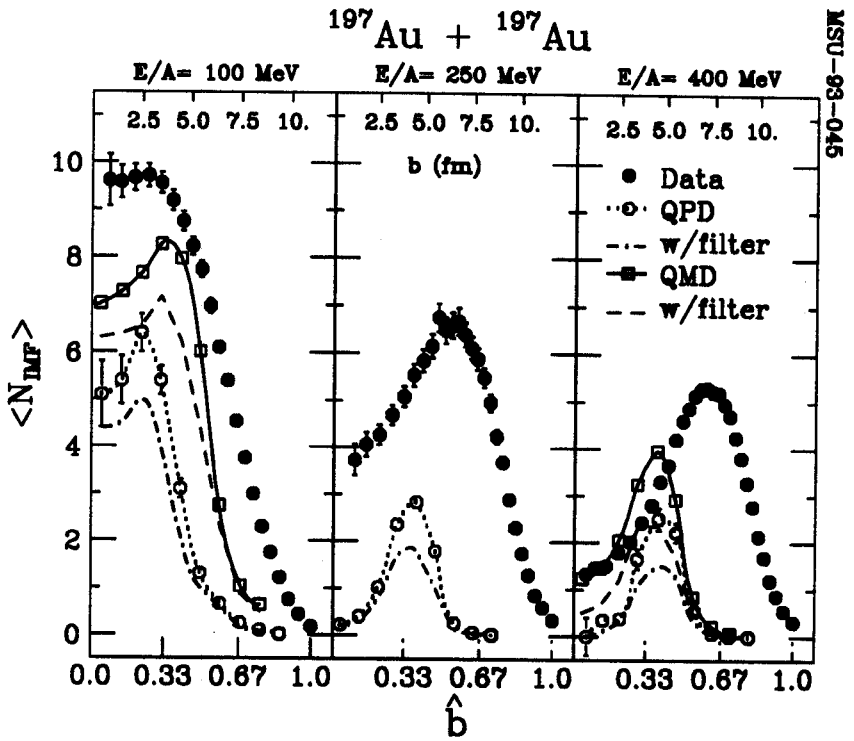

Fig. 4.2.2 The measured impact parameter dependence of the mean fragment multiplicity is shown by the solid points. The open circles and open squares depict the unfiltered predictions of the QPD and QMD models, respectively. The dash-dotted and dashed lines depict the QPD and QMD calculations, filtered through the experimental acceptance.

chamber in the Aladin spectrometer cause a loss in the detection efficiency at E/A = 100 MeV for beam velocity particles emitted to $\theta_{lab} < 10°$. A loss of efficiency also occurs for heavy target-like residues which do not penetrate the scintillator foils of the phoswich Miniball/Miniwall detectors and therefore are not identified. Both effects combine to cause a significantly reduced detection efficiency for peripheral collisions at E/A = 100 Mev. In contrast, the Aladin spectrometer is quite efficient in detecting the beam velocity particles at E/A = 400 MeV, and the mean total detected charge $\langle Z_{tot} \rangle$ is nearly constant as a function of N_c at about 102 (≈65% of the total charge). More details of this detection inefficiency will be described in Section 4.3.

Since $\langle Z_{tot} \rangle$ is nearly independent of the impact parameters, the decrease in IMF production, observed in central collisions at E/A = 400 MeV, is not principally caused by detection inefficiency. Thus, for $^{197}Au + ^{197}Au$ collisions at incident energies significantly above E/A = 100 MeV, the fragment multiplicities in the central collisions decrease with incident energy, consistent with the onset of vaporization in systems that are too highly excited to produce significant numbers of fragments. Multifragmentation is especially suppressed for the overheated systems produced in central collisions at E/A = 400 MeV. For the more weakly excited systems produced in more peripheral collisions, multifragmentation persists, and large fragment multiplicities, e.g., $\langle N_{IMF} \rangle \approx$ 5-6 for $\hat{b} \approx$ 0.67 at E/A= 400 MeV, are observed.

Over much of the incident energy domain spanned in this data analysis, both multifragmentation and collective flow have been successfully modeled for central collisions via microscopic molecular dynamics models [Peil 89, Boal 88, Peil 92]. It is interesting to explore whether such models can also describe the decline of multifragmentation in central collisions. The open squares in Fig. 4.2.2 are the IMF multiplicities predicted by the quantum molecular dynamics (QMD) model of Ref. [Peil 92]. The open circles in Fig. 4.2.2 are the IMF multiplicities predicted by the quasi-particle dynamics (QPD) models in Ref. [Boal 88]. Both calculations were plotted as a function of the reduced impact parameter $\hat{b} = b/b_{max}$, where b_{max} was determined from QPD calculations according to the requirement $\langle N_C(b_{max}) \rangle_{observed} = 4$. This yielded $b_{max} =$

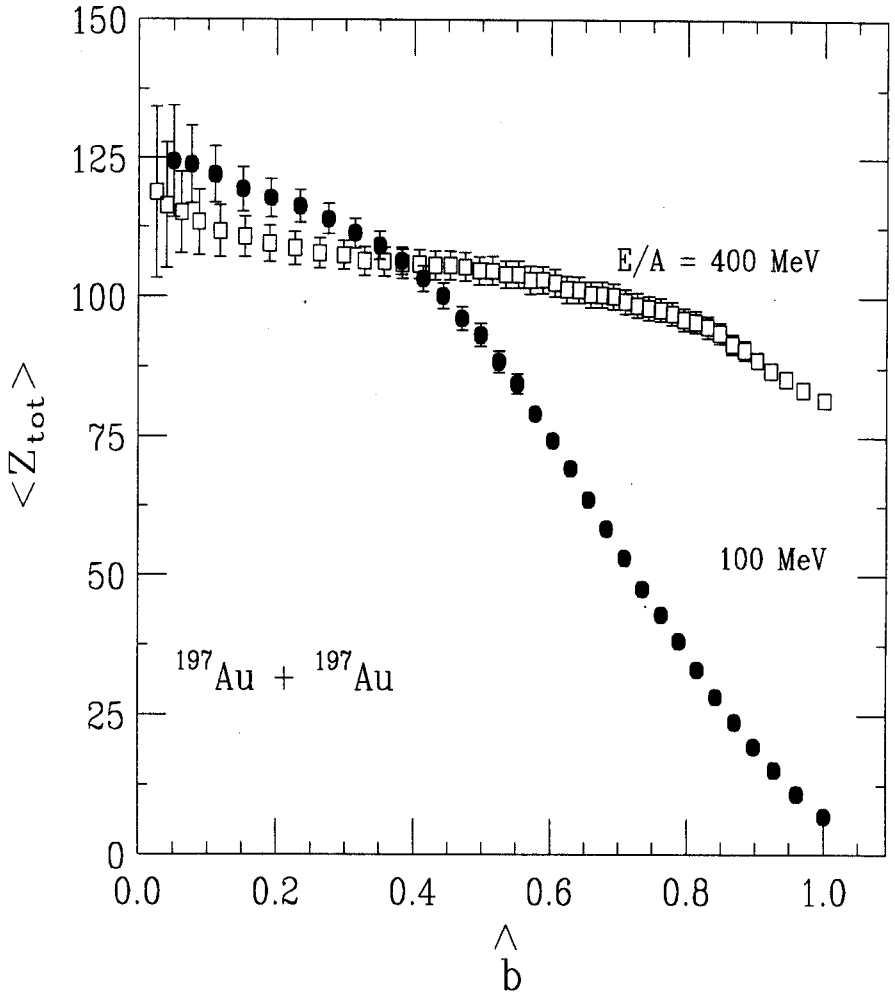

Fig. 4.2.3 The mean total charge of all detected particles as a function of the reduced impact parameter for E/A=100 and 400 MeV. The reduced impact parameter is reconstructed from the charge particle multiplicity using Eq.4.1.2.

11.1, 11.7 and 11.9 fm at E/A= 100, 250, and 400 MeV, respectively. The actual impact parameters used in the calculations are given at the top of Figure 4.2.2. Both models predict enhanced fragment multiplicities for central collisions at E/A = 100 MeV. However, the models underpredict the measured peak IMF multiplicities, and underestimate the shift in the peak fragment multiplicity to large impact parameters with incident energy. These discrepancies are even larger when the calculations are corrected (filtered) for the detection efficiency; filtered calculations are indicated by the dash and dash-dotted lines in Figure 4.2.2.

Previously observed failures of the QMD and QPD calculations to reproduce larger IMF multiplicity observed at lower incident energy [deSo 91, Bowm 91, Tsan 93] and large impact parameters [Ogil 91] have been attributed to an inadequate treatment of statistical fluctuations that lead to the decay of highly excited reaction residues [Lync 92]. Such residues are produced at $b \geq 4$ fm in the present QMD and QPD simulations, but are predicted to decay primarily by nucleon emission [Peil 92], not by fragment emission as predicted by statistical models [Frie 90, Cser 86, Lync 87, Bond 85, Botv 87, Gros 86]. The suppression of statistical fragment emission in QMD and QPD calculations is not fully understood, but it may be related to the classical heat capacities [Peil 92, Lync 92, Boal 89], the suppression of Fermi motion [Peil 92], the insufficient collective motions [Bond 94], or the neglect of quantum fluctuations within the hot residual nuclei [Peil 91], as modeled therein.

To illustrate such statistical decay effects, we have taken the mass and excitation energies of fragments produced in the QMD and QPD calculations as the initial conditions for statistical model calculations, using two different statistical models which both predict a multifragment decay of sufficiently hot residues at the low density [Frie 90, Bond 85, Botv 87]. For the QMD model, the decays of all fragments with $A > 4$ were calculated via the statistical multifragmentation model (SMM) of Ref. [Bond 85, Botv 87], which contains a "cracking" phase transition at low density. Input excitation energies and masses for the SMM calculations were taken from the QMD calculations at an elapsed reaction time of 200 fm/c. For the QPD model, the decays of bound fragments with $A > 20$ were calculated via the expanding evaporative source (EES) model of Ref. [Frie 90],

which describes the evaporative decay of a hot residue expanding self-consistently under its own thermal pressure. Here, the residue properties are evaluated within 10 fm/c after the separation of the hot projectile and target-like residues.

The open squares and the circles in Figure 4.2.4(b) are the predictions from the hybrid QMD-SMM and QPD-EES models, respectively, without correction for the detection efficiency of the experimental apparatus. The dashed curve shows the QMD-SMM predictions after the efficiency corrections for the experimental apparatus were applied. Including the statistical decay of heavy residues increases the peak values for $\langle N_{IMF} \rangle$ in both models to $\langle N_{IMF} \rangle \approx 7\text{-}9$ for E/A = 400 MeV, and moves the peak to larger impact parameters, consistent with experimental observations. Both hybrid models underpredict the IMF multiplicity at the small impact parameters. This reduction is even more evident in the QMD-SMM model predictions at E/A=100 MeV (see Fig. 4.2.4(a)). For such collisions, IMF's are either produced by the QMD model in insufficient quantities, or are too highly excited to survive the SMM statistical decay in numbers consistent with the experimental observations.

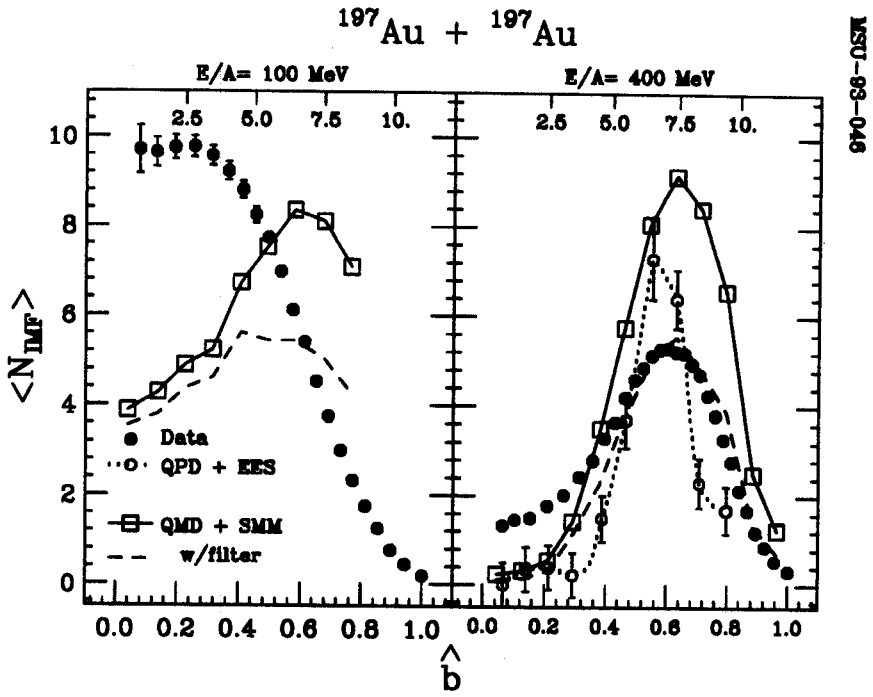

Fig. 4.2.4 Comparisons with hybrid model calculations at E/A=100 and 400 MeV. The solid points depict the data. The open circles and open squares depict the unfiltered predictions of the QPD-EES and QMD-SMM models, respectively. The dashed lines depict the QMD-SMM hybrid model calculations, filtered through the experimental acceptance. The impact parameter scales are identical to those given in Fig.4.2.1.

4.3 Detection Efficiency Correction at E/A = 400 MeV

Fragments emitted from the participant region in collisions at E/A = 250 and 400 MeV can have energies far higher than those energies where fragments penetrate through the CsI(Tl) crystals of the Miniball/wall array. Such fragments and light particles which "punch" through the Miniball/wall detectors are often indistinguishable. Similar problems occur for particles which "punch" through the CsI(Tl) crystals of the Catania hodoscope. The resulting inefficiency for detection of IMFs makes it difficult to precisely assess the fragment yields in the regime of nuclear vaporization attained in central collisions at E/A = 400 MeV. For this reaction, efficiency corrections to the fragment yields may be performed using the mass symmetry of the Au + Au system and the wide acceptance of the detection array used in this experiment.

Figure 4.3.1 shows the measured rapidity-transverse momentum distribution $\frac{dP}{dydp_t}$ for Lithium fragments emitted at E/A = 400 MeV and reduced impact parameters in the range $0.43 < \hat{b} \leq 0.75$, where the maximum multiplicity of IMFs is measured. Experimental data is shown for the Miniball and ToF wall, where both the energies and the yields of Lithium ions could be measured with a significant and well understood efficiency. For reference, the boundaries of the angular and energy acceptances of the Miniball, Miniwall, Catania hodoscope, and ToF wall are indicated by the individual lines in Figure 4.3.1. Note that the boundary between the Catania hodoscope and Aladin spectrometer, represented by the cross hatched region in the figure, does not correspond to a fixed value of θ_{lab}. The acceptance of low energy ions in the Miniball is strongly influenced near the $y_{norm} = 0$ by energy loss in the target. The acceptance of low energy ions at the $y_{norm} < 0.3$ in the Aladin spectrometer is also low because such ions can be stopped in the front window of the TP-MUSIC detector or bent away from the ToF wall by the Aladin dipole magnet.

These detection inefficiencies can be carefully examined to obtain efficiency corrected IMF yields. Since there is mass symmetry in the entrance channel, values for $\frac{dP}{dydp_t}$ at a rapidity y in the center of momentum (c.m.) system is a reflection of the "mirror" distribution at -y. For example, the distribution for fragments detected but not

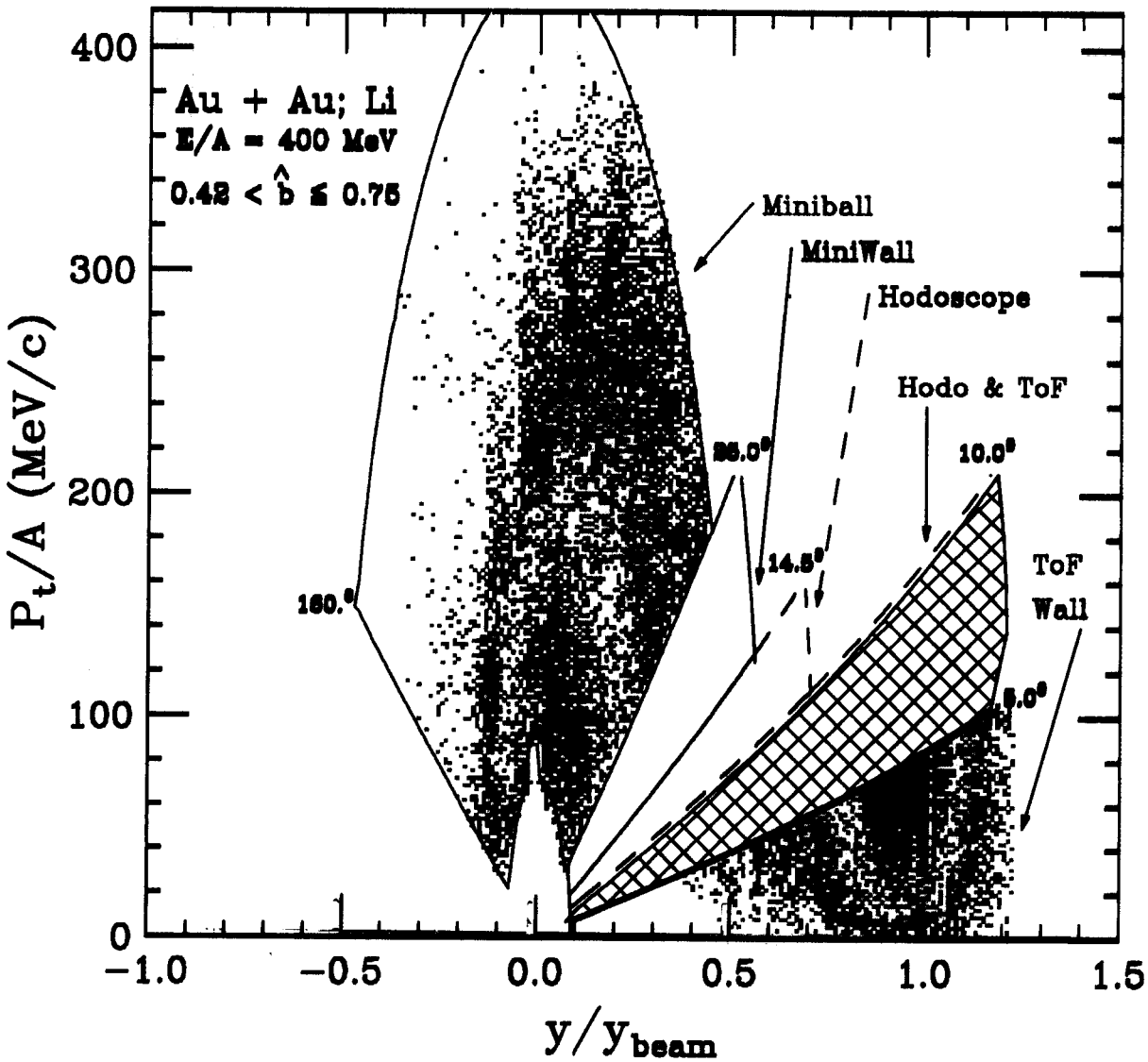

Figure 4.3.1 The y-P_t scattered distributions for Li ions at near mid-central collisions are plotted as a function of normalized rapidity y/y_{beam} (y_{norm}). The distributions at the polar angles $5^{\circ} \leq |\theta_{lab}| \leq 25^{\circ}$ are not included where energy calibrations were lacking. The distributions are also strongly shielded by the target at the target-rapidities. Also, the IMFs with small P_t and $y_{norm} < .5$ will not be detected by the ToF wall.

calibrated at positive rapidities in the Catania array can be determined from the distribution measured by the Miniball array. Low energy fragments stopped in the target can be determined from the distribution measured with the ToF wall. Near the c.m. rapidity, however, there is a gap in the acceptance of the array. Emission into this region was estimated by methods described below.

Reconstruction of the Emission Pattern

Corrections for the inefficiency of the experimental array were assessed by simulating the fragment emission patterns and projecting them upon the experimental acceptance. In the limit of a "two step" model for peripheral collisions, where fragments are emitted via the statistical decay of a hot prefragment, the p_t distributions of emitted fragments are approximately independent of rapidity. This suggests a factorization ansatz $\frac{dP}{dydp_t} = P_1(p_t) \cdot P_2(y)$, where P_1 can be determined at rapidity values where the experimental acceptance is relatively complete, and P_2 must be determined from the measured dependence upon rapidity, as described below.

Assuming the central limit theorem is applicable, P_1 was calculated by assuming Gaussian distributions in p_x and p_y. The Box-Muller method [Pres 86] was used to generate Gaussian distributed values for p_x and p_y. It works as follows: If x_1 and x_2 are random numbers with a joint probability distribution $P(x_1, x_2)$, and y_1 and y_2 are each functions of x_1 and x_2, then the joint probability distribution for y_1 and y_2 is

$$P(y_1, y_2)\, dy_1 dy_2 = P(x_1, x_2) \left| \frac{\partial(x_1, x_2)}{\partial(y_1, y_2)} \right| dy_1 dy_2 \qquad (4.3.1)$$

where $\left| \partial(x_1, x_2) / \partial(y_1, y_2) \right|$ is the Jacobian determinant for the coordinate transformation $x_1, x_2 \Rightarrow y_1, y_2$. To obtain any arbitrary probability distribution $P(y_1, y_2)$ starting from a given probability distribution $P(x_1, x_2)$, it suffices to find the appropriate coordinate transformation that gives the correct Jacobian determinant. In this case, one wants to

obtain the two-dimension Gaussian (normal) distribution

$$P(y_1,y_2)dy_1dy_2 = \frac{1}{2\pi\sigma_1\sigma_2} e^{-y_1^2/2\sigma_1^2} e^{-y_2^2/2\sigma_2^2} dy_1dy_2 \quad . \tag{4.3.2}$$

starting from the unit random number distribution,

$$P(x_1, x_2) = 1 \qquad \text{for } 0 < x_i \leq 1;\ i= 1, 2 \tag{4.3.3}$$
$$= 0 \qquad \text{otherwise.}$$

By direction substitution, it can be shown that the transformation,

$$y_1 / \sigma_1 = \sqrt{-2\ln x_1}\cos(2\pi x_2) \tag{4.3.4}$$

$$y_2 / \sigma_2 = \sqrt{-2\ln x_1}\sin(2\pi x_2) \tag{4.3.5}$$

satisfies Eq. 4.3.1. Physically, $2\pi x_2$ corresponds to the angle between y_1 and y_2 (p_x and p_y in our case), and x_1 comes from a mapping of the angle integrated Gaussian distribution for p_t onto a unit probability distribution in x_1, where $x_1 = 0$ corresponds to $p_t = \infty$, and $x_1 = 1$ corresponds to $p_t = 0$. In cases where speed is of essential importance, it is sometimes useful to define additional random variables v_1 and v_2 as the coordinate and abscissa of the random points inside the unit circle. Then, the sum of their squares, $R \equiv v_1^2 + v_2^2$ can be used for x_1, and $\sin(2\pi x_2)$ and $\cos(2\pi x_2)$ are given by $v_1 / \sqrt{R}$ and $v_2 / \sqrt{R}$, respectively.

The choice of independent width parameters σ_x and σ_y allows for a two component fit to the angle integrated p_t distribution, as well as the ability to describe possible anisotropies in the experimental azimuthal distributions about the beam axis. The result of a simulation with two different width parameters σ_x and σ_y is shown in Figure 4.3.2. The individual p_x and p_y distributions are shown in the two bottom panels in the figure. The total p_t distribution is shown in the top panel. Even with 10^5 events, these simulations closely follow the corresponding Gaussian distributions calculated analytically (solid lines). Thus, the Box-Muller transformation method provides for efficient and accurate Gaussian random number generation.

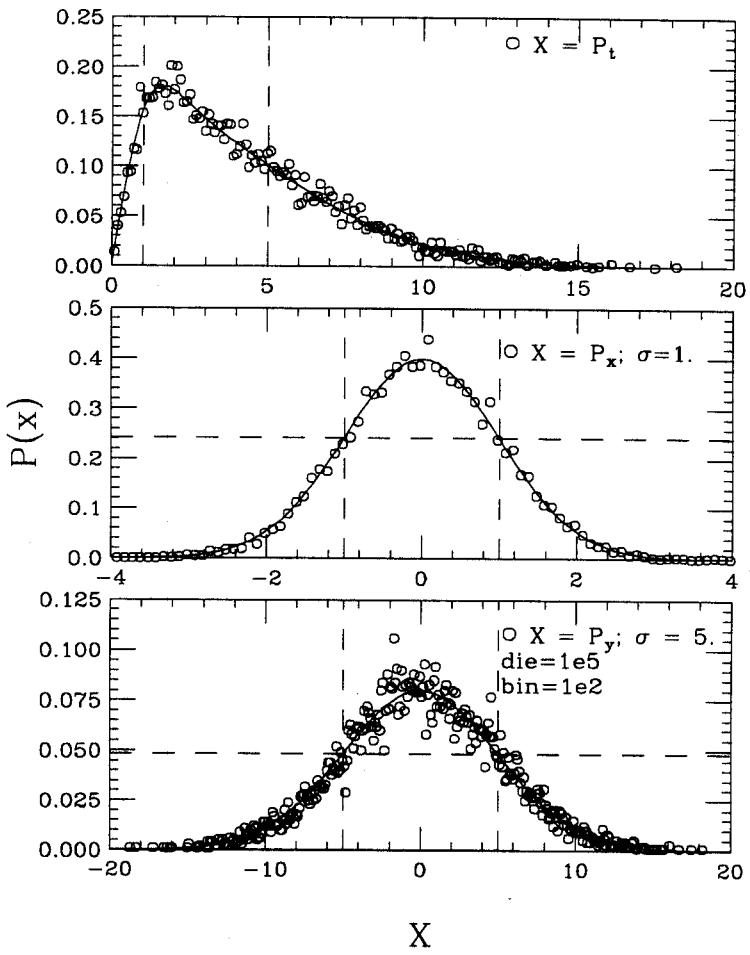

Figure 4.3.2 The Gaussian sources obtained from the Box-Muller method with different variances in x and y directions are plotted as open circles in the two bottom panels. The vertically dashed lines indicate the width of the σs. The total transverse moment distribution is plotted as the open circles in the top panel with the vertical dashed lines indicating the σs in the x and y directions. The solid lines in all the panels are calculated analytically.

Experimental y-P_t Cross Sections

Experimental rapidity-transverse momentum distributions obtained by using only the data from the well calibrated Miniball and ToF devices. Angles between 5° to 10° in the ToF wall were not used, because one could not obtain the full azimuthal distribution at these polar angles. Smooth rapidity and transverse momentum distributions were created by randomly reassigning the emission angles of particles detected in specific detector of the Miniball to spread them uniformly over the solid angle of that detector. Furthermore, a correction factor is applied for each polar angle in the Miniball, to compensate for the loss of efficiency that occurs whenever there are detectors in the Miniball that malfunction.

The spectra at the projectile and target rapidity were combined to compensate for the deficiencies of each and thereby obtain a uniform and wide dynamic range p_t spectrum. The distributions in the Miniball at low p_t were replaced by distributions measured in the ToF wall at $y_{norm} > 0.5$ and $\theta_{lab} < 5°$ [Kund 94], to avoid complications due to the nonlinear response in the CsI(Tl) detectors in the Miniball at low energies. This provided continuous p_t distribution at target rapidities ranging from $p_t \approx 0$ up to the "punch through" points where particles penetrate through the CsI(Tl) detectors of the Miniball. This distribution can be reflected about the c.m. rapidity to obtain the corresponding distributions near the projectile rapidity. The combined distribution for Lithium particles emitted at E/A = 400 MeV and peripheral impact parameters $.67 < \hat{b} \leq .78$, is shown in the left panel in Figure 4.3.3. It should be noted that this distribution indicates only those portions of the experimental acceptance where accurate energy determinations could be made. The experimental fragment multiplicity distributions in Fig. 4.2.1 also included the yields of many fragments at mid-rapidity, $y_{norm} \approx 0.5$, for which accurate energy calibrations were not available.

At both peripheral and mid-central collisions, projectile- and target-like spectator sources dominate the observed IMF distributions. The measured distributions were modeled using the factorization ansatz $\frac{dP}{dydp_t} = P_1(p_t) \cdot P_2(y)$, where

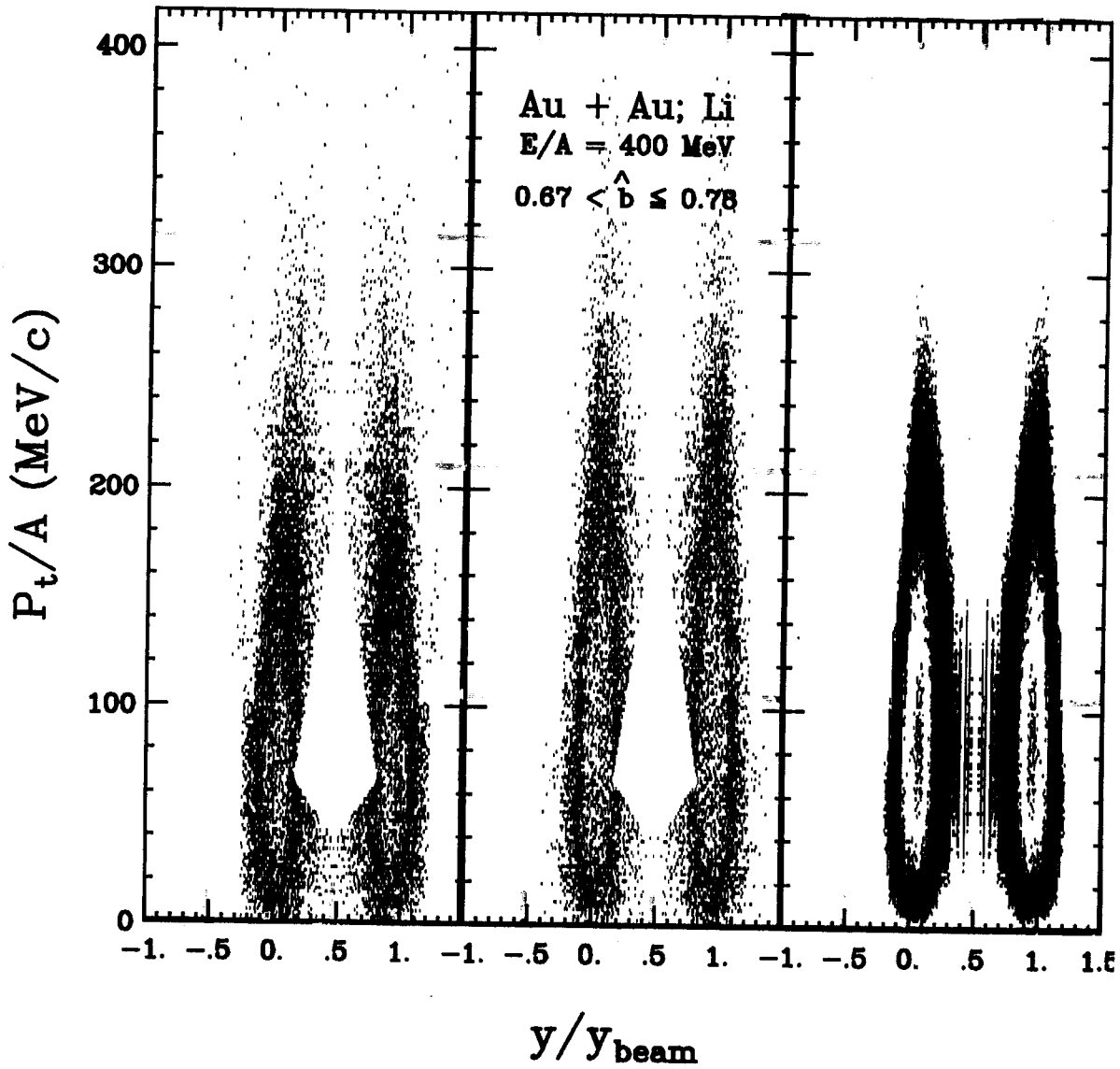

Figure 4.3.3 The distribution of Li fragments as a function of y and p_t are plotted for events with impact parameters of $.67 < \hat{b} \leq .78$. The experimental cross sections are plotted in left panel. The simulation with the detection acceptance correction is plotted in middle panel. The simulation without the experimental acceptance cut is shown in the right panel.

$$P_1(p_t) = P_x(p_x) \cdot P_y(p_y) = \frac{1}{\sigma_x \sigma_y} e^{-(p_x^2/2\sigma_x^2 + p_y^2/2\sigma_y^2)} \quad (4.3.6)$$

and σ_x and σ_y are determined at the values of $.19 \leq y_{norm} \leq .29$ where the coverage in p_t is nearly complete from threshold to the punch-through points. The resulting distributions are somewhat wider than those observed at the $y_{norm} \leq .19$, but that was irrelevant because the coverage was complete at smaller y_{norm} values. Measured transverse momentum distributions of those modeled using Eq. 4.3.6 and corrected for the experimental acceptance, are plotted for different rapidity bins as the solid points and dashed lines in Figure 4.3.4. Here, $P_2(y)$ was determined by requiring the same number of simulated counts in each rapidity bin, as observed in the experimental data. Applying this procedure at all measured rapidities, one obtains the values for $P_2(y)$ shown in Figure 4.3.5. The correction for the experimental acceptance can be obtained by comparing those simulations with the acceptance corrections to those without the corrections. Calculations without the acceptance correction are shown by the solid lines in Figure 4.3.4. Similarly, Figure 4.3.3 compares the simulations with (center panel) and without (right panel) acceptance corrections to the measured $\frac{dP}{dydp_t}$ distribution for peripheral collisions at $.67 < \hat{b} \leq .78$ and E/A = 400 MeV.

Contributions to the measured yield at central rapidities $y_{norm} \approx 0.5$ at large impact parameters were determined by comparing simulated to measured distributions at smaller p_t. This provided a lower limit for the fragment yields. The low acceptance for the experimental array at mid-rapidities has the consequence of large uncertainties in the deduced contributions at mid-rapidities, however. At large impact parameters, the yields at mid-rapidity are comparatively small and the interpolation leads to relatively small uncertainties as shown in Fig.4.3.4. At small impact parameters, this method can be applied. Its accuracy is more uncertain because it inadequately constrains the interpolation to mid-rapidities of the yields measured accurately at both larger and smaller rapidities, and because these mid-rapidity yields are such a large fraction of the total yield for these central collisions.

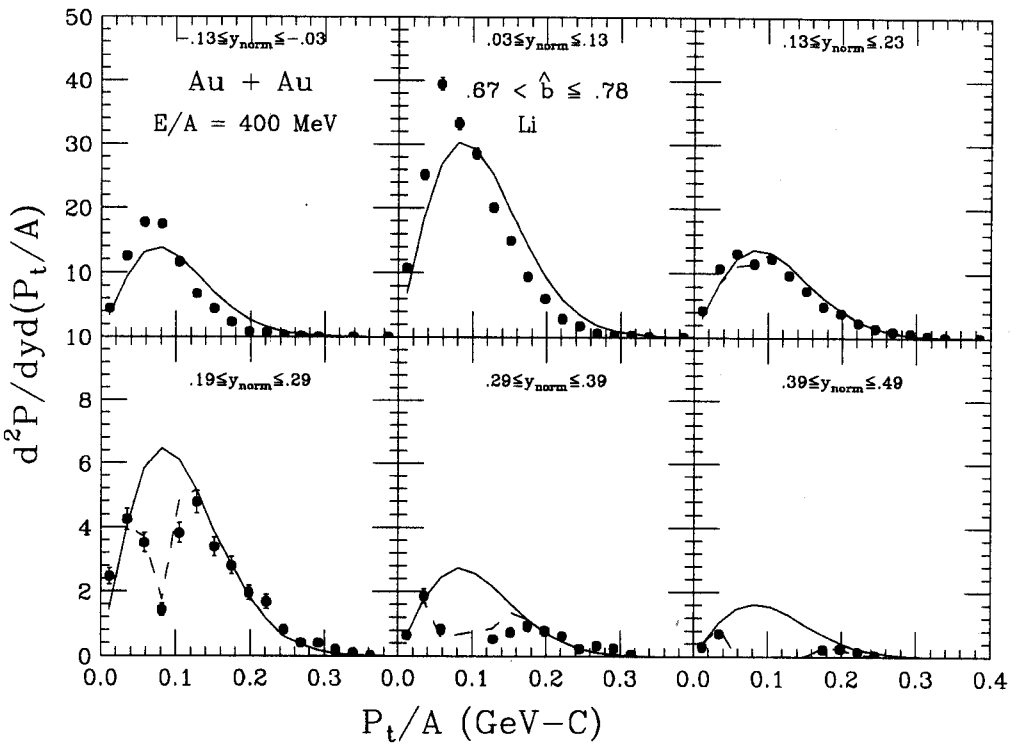

Figure 4.3.4 The transverse momentum cross sections of Li fragments are plotted as solid circles for the data at the impact parameter of $.67 < \hat{b} \leq .78$. The dashed lines are the simulations filtered through the acceptance cut. The solid lines are the results without the acceptance cut.

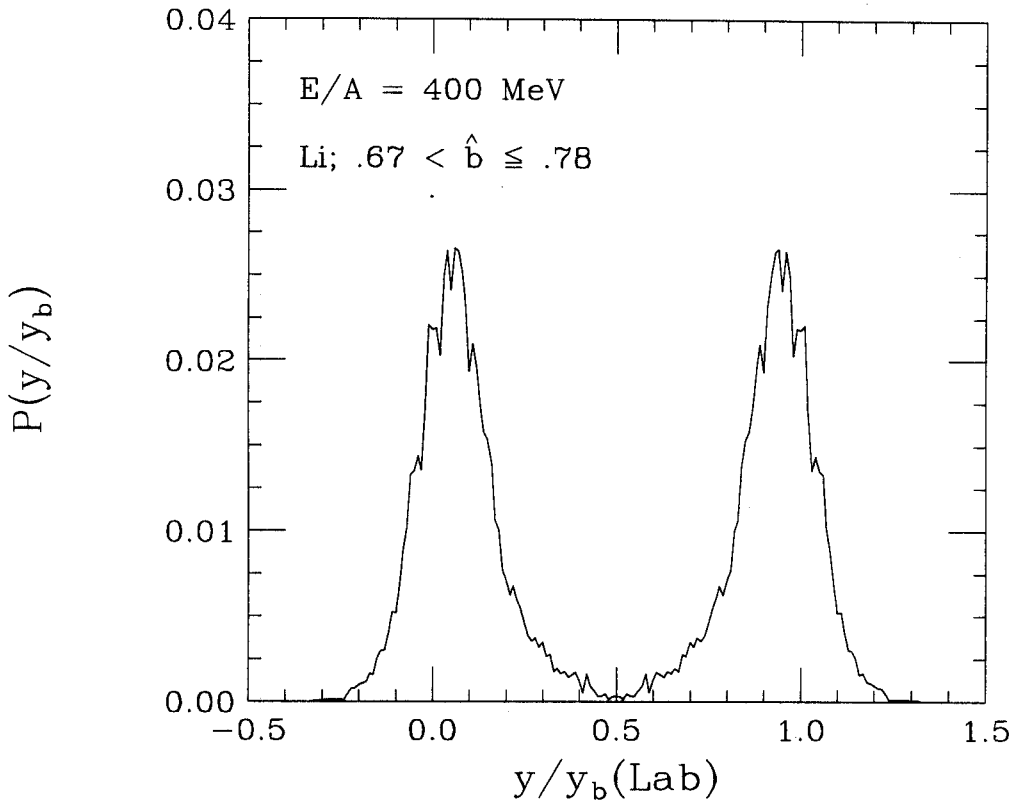

Figure 4.3.5 The extracted probability distribution was plotted as a function of normalized rapidity for Li fragments at impact parameters $.67 < \hat{b} \leq .78$. This probability distribution was folded into the final simulations of the transverse momentum-rapidity distribution.

For efficiency determination at smaller impact parameters, an alternative extrapolation to mid-rapidity was obtained by using the parameterization of a single participant source. In this procedure, the contributions from the spectators are obtained at y_{norm} less than .19 and contributions at y_{norm} greater than .19 are determined from the decay of a single participant source centered at mid-rapidity given by

$$\frac{dN_{part}}{dp_t dy} = \text{const. } P(p_t)\, e^{-(p_z^2/2mT)} \frac{dp_z}{dy}, \qquad (4.3.8)$$

Here, T represents the temperature of the source emitting the fragment. $P(p_t)$ is the probability distribution given by Eq. 4.3.6 where the width σ_y and the ratio of σ_x/σ_y are determined by fitting the $\frac{dP}{dydp_t}$ distribution at laboratory values of the rapidity $y_{norm} \approx$ 0.19-0.29 where the contributions are dominated by the participant source. By assuming that the distribution along P_z to be governed by an effective temperature determined from the P_t distribution of $y_{norm} \approx 0.19$-0.29, a temperature T = 210 MeV was assigned and the yields evaluated according Eq. 4.3.8.

The largest yields extrapolated from this thermal source with T = 150 and 210 MeV were used to provide an upper limit of estimation of the fragment yields. The Miniball/Miniwall gates are drawn rather tightly about the Z = 3 lines to exclude the α particles. This combined with nonlinearities in the Miniball/Miniwall energy calibrations may conspired to reduce the yield in the Miniball at law energies. To provide an upper limit for potential losses of low energy fragments in the Miniball, an upper limit of 50% loss in IMF yields at E/A = 7 MeV was assumed. The filtered simulations for this upper limit are plotted as doted lines in Figures 4.3.6 for central collisions with . The unfiltered simulations are plotted as the dotdashed lines. Since energy spectra are not available for the Miniball detectors beyond Z = 10, simulations were only performed up to Z = 10. For charges from Z = 11 to 30, the correction to the fragment yield is taken from the correction factor for Z =10.

To see how well this simulation reproduces the fragment yields presented in section 4.2, the mean numbers of detected IMFs in the various devices are plotted as a function of the reduced impact parameter in the upper panel of Figure 4.3.7. The vertical

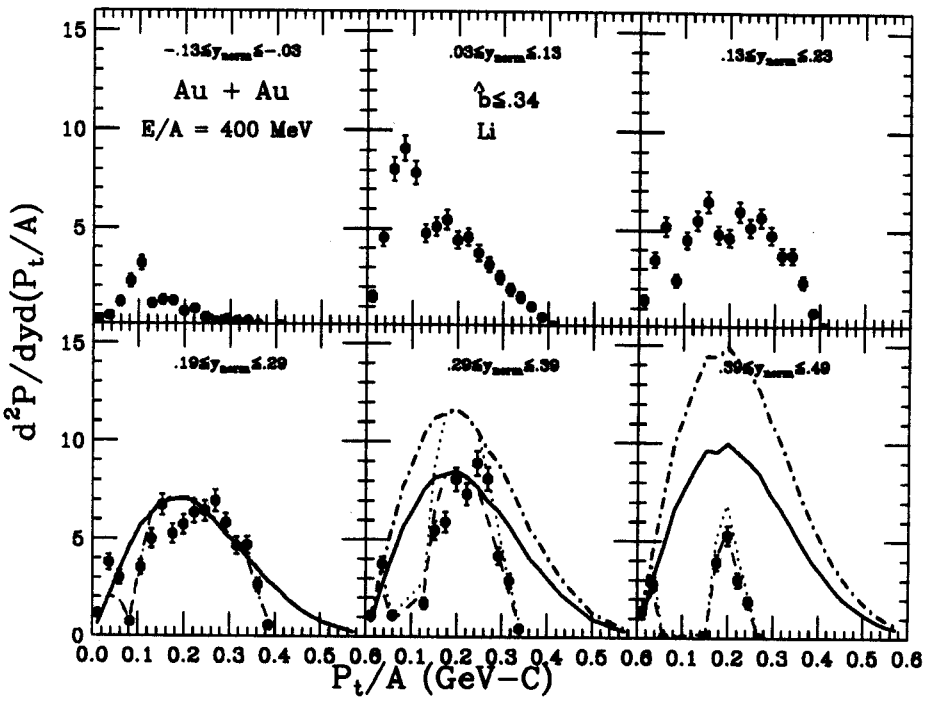

Figure 4.3.6 The transverse momentum distribution for Li fragments are plotted as the solid circles for the experimental data at impact parameters $\hat{b} \leq .34$. The dashed lines are the results of simulation which the filtered yields are normalized with the measured data at all rapidities. The dotted lines are the results of simulation for which the normalization was taking from the thermal source. The solid and dotdashed lines are the corresponding results without the experimental acceptance cut.

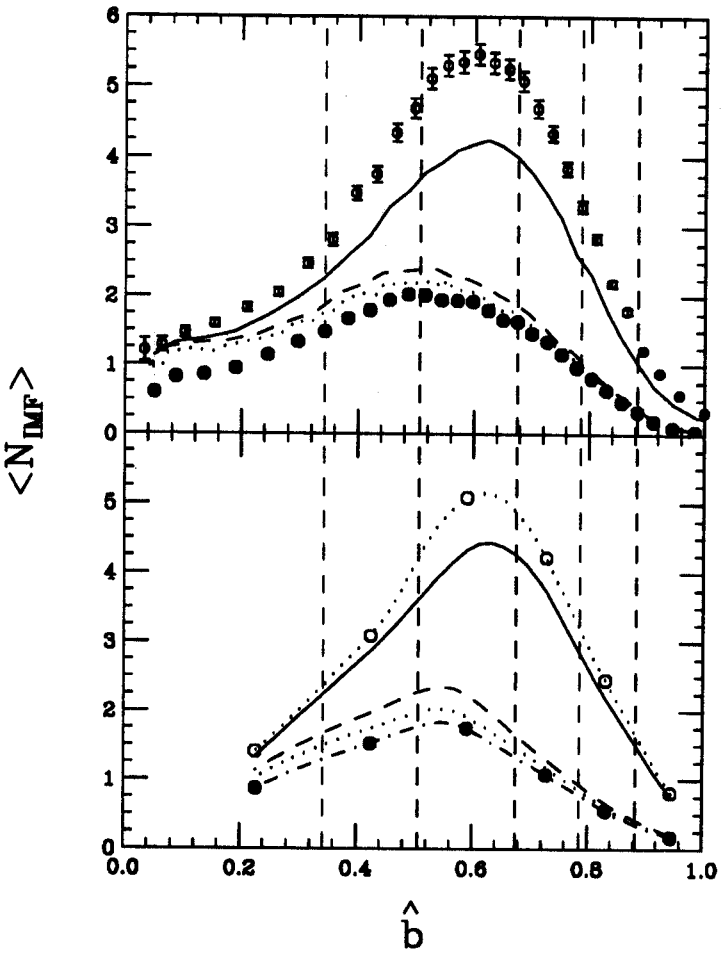

Figure 4.3.7 The measured mean IMFs as a function of the reduced impact parameter with the various device acceptances at E/A = 400 MeV. The solid circle points are the number of IMFs detected in the Miniball array only. The dot points are added with the Miniwall array. Adding in the Catania hodoscope is presented by the dashed line. The solid line further add in the IMFs detected with the polar angle $|\theta_{lab}| \leq 5^0$ in the ToF wall. The highest open circle points are the total number of detected IMFs within the combined devices. The vertical lines indicate the impact parameter ranges for the y-P_t simulations. The simulations filtered through the devices are plotted in bottom panel.

lines represent boundaries of impact parameter gates for the simulations. Within these boundaries, the efficiency was determined and interpolated linearly between the centroids of each gate. The corresponding simulated results are shown in the lower panel of the figure.

A comparison of the measured fragment multiplicities (solid points) to the efficiency corrected fragment yields (Bars) is provided in Figure 4.3.8. The bars are bounded at the lower part by the procedure where the filtered yield are normalized to the measured data at all rapidities. The upper limits of the bars are the upper limit of yields extracted as described in previous paragraph. The efficiency corrected multiplicities are about 50% larger than the ones measured for central collisions, and nearly a factor of two for mid impact parameter collisions, where they reach their maximum values. These simulations confirm that the observations of nuclear vaporization were not simply due to problems with the experimental acceptance at mid-rapidities.

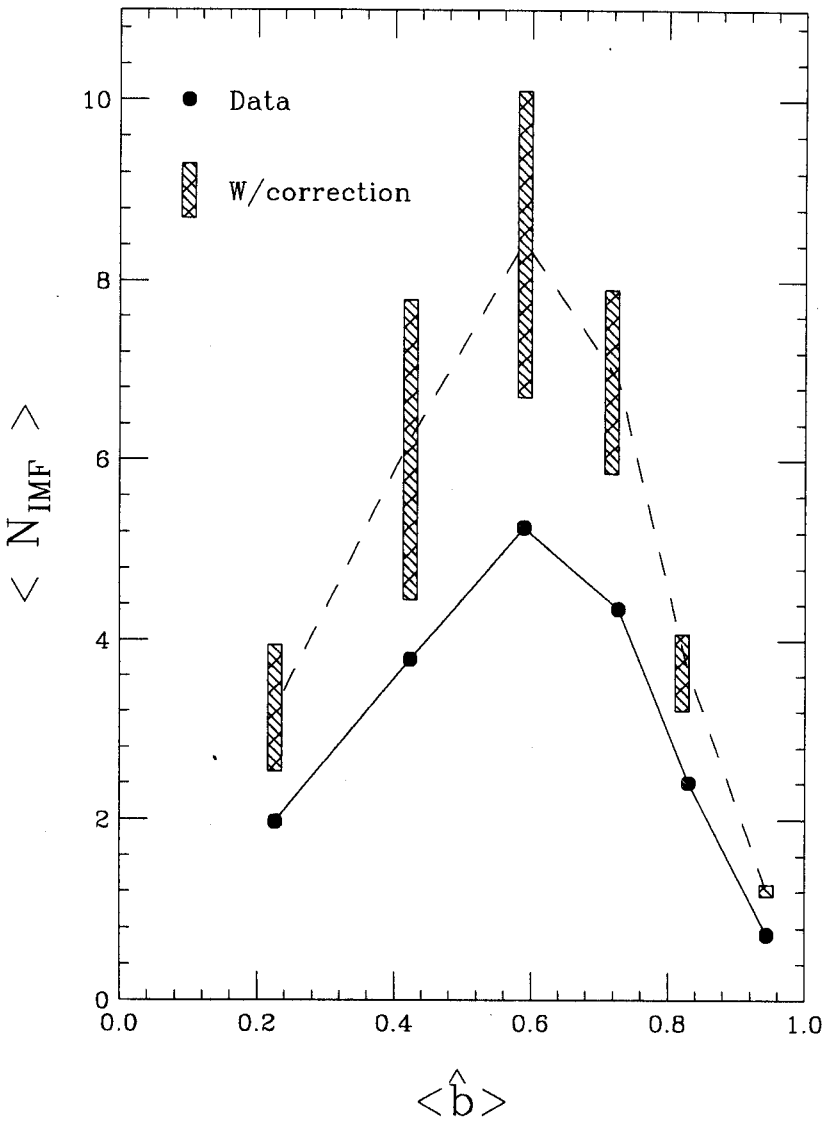

Figure 4.3.8 The mean number of IMFs was plotted as a function of the reduced impact parameters. The solid circles are the experimental measurements. The bars are the range of values determined by the efficient calculations. These bars reflect the range of efficiency corrected values that would be allowed considering the uncertainties of extrapolating into the region at mid-rapidity, where the array provided little energy information.

4.4 Reaction Dynamics

In this section, the mean transverse energies of emitted fragments are compared to the theoretical predictions. The impact parameter and incident energy dependence of the energy spectra and triple differential cross sections are compared to moving source calculations to search for evidence of collective motion, and determine the extent to which such collective motion influences the fragment observables. The details of the radial expansion will be discussed in the next section.

4.4.1 Transverse Energies of Emitted Fragments

Even though the mean number of the intermediate mass fragments (IMFs) (as a function of impact parameter) were not well-reproduced by the QMD or QPD calculations for these Au on Au collisions, it is still relevant to ask whether the collective and thermal motions predicted by these models are comparable to the experimental observations. Due to the large amounts of time needed to perform such calculations, it is very difficult to generate comprehensive comparisons to measured energy spectra. However, one can make quantitative comparisons to the experimental mean transverse energies defined by

$$< E_t >= \sum_i E_i \sin^2\theta_i \times P(E_i,\theta_i) / \sum_i P(E_i,\theta_i) \qquad (4.4.1)$$

where E_i, θ_i and $P(E_i, \theta_i)$ are the energy, the polar angle and the probability of the detected fragment. Collective and thermal motions contribute differently to the transverse energies; to first order, the thermal contributions reflect the local temperature and are independent of mass, while the collective contributions scale linearly with the fragment mass. The mean transverse energies for the emitted fragments were evaluated between $25.° \leq \theta_{lab} \leq 160.°$ where the phase space is covered by the Miniball detectors and good energy calibrations were obtained at all incident energies.

The measured mean transverse energies for α, Li and C fragments are plotted as a function of the reduced impact parameter in Fig. 4.4.1 for collisions at E/A = 100, 250 and 400 MeV. The error bars reflect a 8% systemic uncertainty in the energy calibration. At

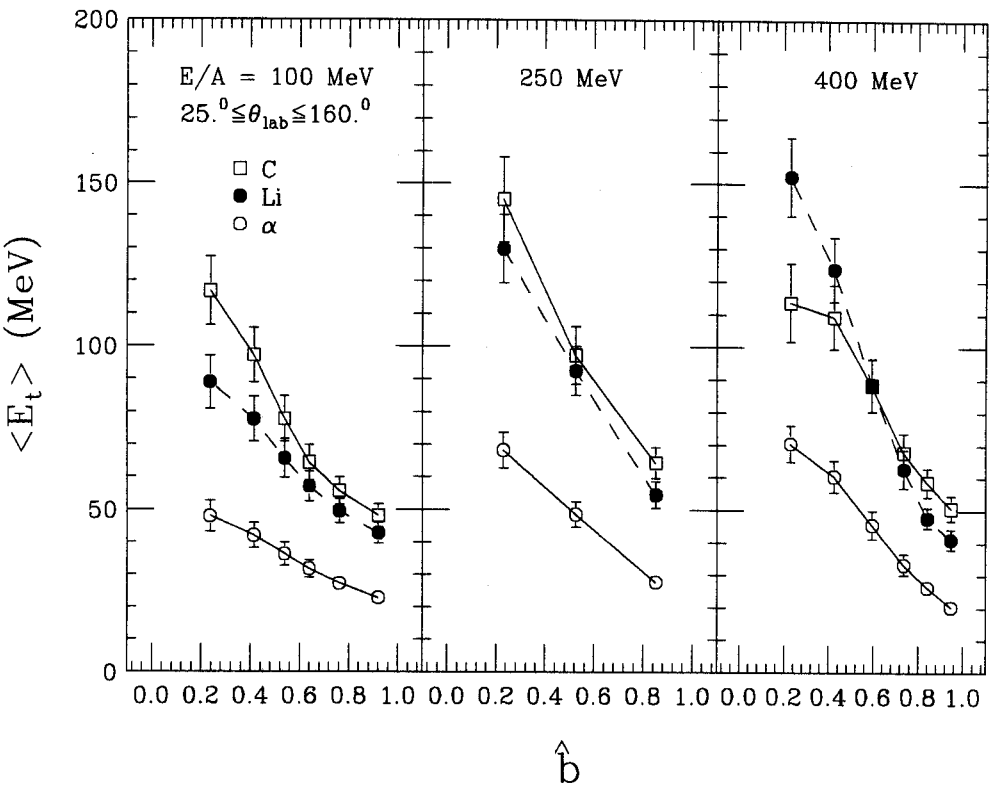

Figure 4.4.1 Mean transverse energies plotted as a function of the reduced impact parameters for α, Lithium, and Carbon fragments at $25° \leq \theta_{lab} \leq 160°$. The three panels correspond to the collisions at E/A = 100(left panel) , 250 (middle panel) and 400 (right panel) MeV.

small impact parameter, these error bars are enlarged to reflect the effects of coincidence summing which are estimated by adding randomly signals from different events according the observed single hit probabilities. The observed mean transverse energies for the emitted fragments generally increase with a decreasing impact parameter. Because many particles punch through the detectors, the E_t values for α particles can not increase as much as those of the heavier fragments with increasing centrality or incident energy or both. In general, heavier fragments display larger values of E_t, consistent with the existence of a significant collective motion in the system at breakup. The mean transverse energies of Carbon fragments in central collisions at E/A = 400 MeV are less than those for Lithium fragments suggesting that the heavier fragments do not participate as fully in the collective motion as the lighter fragments do.

To study the dependence on the mass of fragment in greater detail, the mean transverse energies are plotted as a function of the fragment charge in Fig. 4.4.2. Due to a lack of statistics from model calculations, comparisons with the QMD and QMD + SMM models are only shown for two impact parameter regions: $\hat{b} \leq 0.34$ (central, upper panels) and $0.45 \leq \hat{b} < 0.75$ (mid impact parameters, lower panels). This mid impact parameter range was chosen to bracket the impact parameter range corresponding to the maximum number of fragments produced in collisions at E/A = 400 MeV. The experimental data is plotted as open and closed circles respectively. The solid and dashed lines represent the QMD and QMD + SMM simulations which have been filtered through the experimental acceptance. The QMD calculations generally underpredict the mean transverse energies in these collisions, perhaps reflecting the absence of Fermi motion in the original projectile and target nuclei as modeled by the QMD model. By including the statistical decay of hot fragments and residues, as in QMD + SMM simulations, the mean fragment transverse energies are further reduced. As shown in Fig. 4.4.2, including the statistical decay of the spectator residues and hot fragments via the SMM model, the observed mean number of IMF's can be reproduced for these mid central collisions at E/A = 400 MeV. This might indicate that the IMFs were produced from the decay of the colder thermalized spectator [Kund 95, Möll 95]. However, the underpredictions of the mean transverse energies by

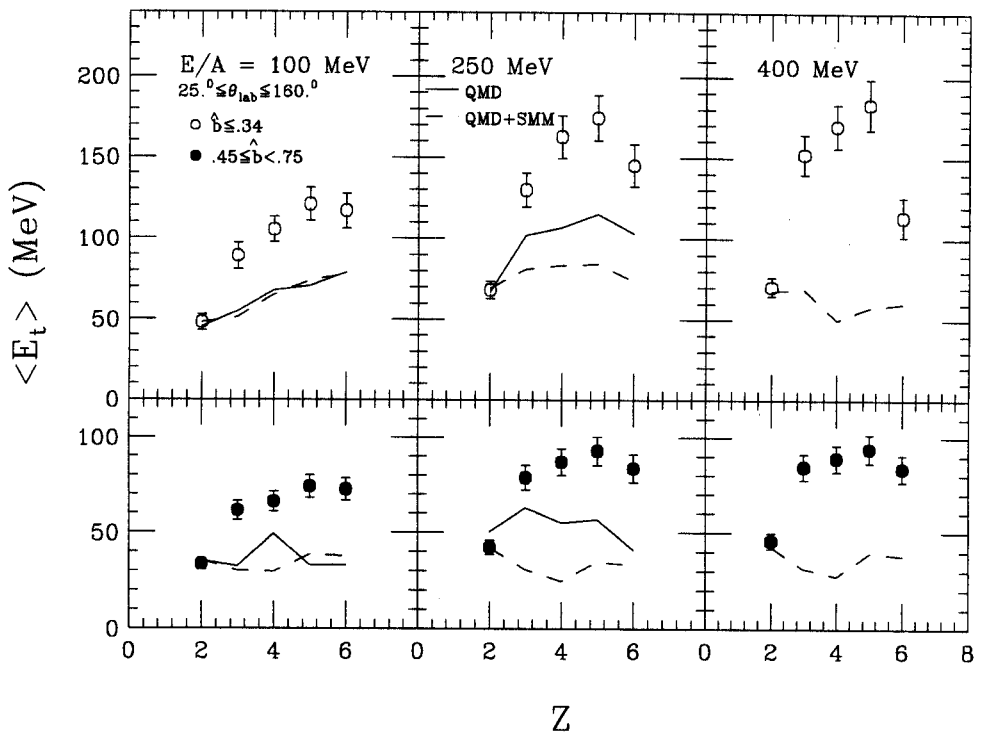

Figure 4.4.2 Mean transverse energies are plotted as a function of the fragment charge for $\hat{b} \leq 0.34$ (top panels) and $.45 \leq \hat{b} < .75$ (bottom panels) at E/A =100, 250 and 400 MeV incident energies. The QMD and QMD + SMM calculations, filtered through the experimental acceptance, are plotted as solid and dashed lines, respectively.

the QMD + SMM model indicates that many of the IMFs are not produced by the slow thermalized decay processes described by the SMM model. This discrepancy is largest for Z = 4 and decreases slightly by Z = 6. It has been reported that the energies of IMFs with Z > 10 are consistent with the thermal breakup of a projectile residue at a temperature of about 20 MeV [Lind 93]. How one reconciles these observations with the transverse energies in Fig. 4.4.2 is not clear at present.

4.4.2 Three-Moving-Source Model

With the failure of the QMD and QPD models which were specially developed to explain the dynamics of fragment emissions, it is appropriate to perform more systematic analyses of the fragment energy spectra and triple differential cross sections. For this purpose, schematic moving-source models [Chit 86, Phai 92, Bowm 92] are often useful. One often assume three sources: a projectile-like, a target-like and a mid-rapidity source. For example, three source parameterizations have been successfully used to describe mass asymmetric heavy ion collisions at low energies [Phai 92]. Assuming a mass symmetric entrance channel, and allowing for some transverse deflection of the projectile- and target-like spectators sources, one can write

$$\frac{d^2P}{dEd\Omega} = \sum_{i=1}^{3} \frac{d^2P_i}{dEd\Omega} = \frac{d^2P_1}{dEd\Omega} + \int_0^{2\pi} d\phi \sum_{i=2}^{3} \frac{d^2P_i}{dEd\Omega}(\vec{p}, \vec{v}_i, V_i), \qquad (4.4.2)$$

where each of these sources is centered at a velocity $\vec{v}_i$ and characterized by a temperature T_i. E and $\vec{p}$ denote the kinetic energy and momentum of the emitted particle, V_i denotes the effective Coulomb barrier of the ith source, and ϕ_R denotes the azimuthal angle of the reaction plane. Source 1 represents the participant and sources 2 and 3 represent the target and projectile-like spectators moving with a velocity $\vec{v}_i$ with both longitudinal and transverse components. The integration over ϕ_R is appropriate for analyses in which the reaction plane has not been defined.

In Eq. 4.4.2, $dP_i / dEd\Omega(\vec{p},0,V_i)$ is defined in the rest frame of the source ($\vec{v}_i \equiv 0$) by

$$\frac{dP_i}{dEd\Omega}(\vec{p},0,V_i) = a_i\Theta(E-V_i)(E+mc^2-V_i)$$

$$\times\sqrt{(E+mc^2-V_i)^2-m^2c^4}\times\exp(-\frac{E-V_i}{T_i}), \qquad (4.4.3)$$

and $dP_i / dEd\Omega(\vec{p},\vec{v}_i,V_i)$ is obtained from Eq. 4.4.3 by Lorentz transformation. In Eq. 4.4.3, a_i is a normalization constant, T_i is a temperature parameter, and $\Theta(E-V_i)$ is the unit step function. In the following analyses, the mass m is taken for simplicity from that of the most abundant natural isotope, e.g. A =11 for Boron. Because of the mass symmetry of the entrance channel, $\vec{v}_2 = -\vec{v}_3$, $a_3 = a_2$, and $T_3 = T_2$ are stringently required in the CM frame for the spectator sources.

4.4.3 Differential Cross Sections of Fragment

Energy Spectra of Fragments

To illustrate the impact parameter dependencies of the IMF energy spectra, the spectra of Lithium and Boron fragments were created for three different impact parameter bins at E/A = 100 MeV, as shown in Figure 4.4.3. The solid lines are the sum of contributions from the three sources, and the dashed lines are the contributions from the participant source alone. The corresponding parameters for the fits are listed in table 4.4.1. The cross sections at low energies are sensitive to the decay of the target-like residues formed in peripheral collisions, as shown in the top panels of each column. As the impact parameter is decreased, the spectra become flatter, reflecting larger yields at higher energies. This increased yield is due to a bigger contribution from the participant source. This source, however, is not well described by the fits at $\theta_{lab} \leq 45$ MeV and E/A > 40 MeV. Instead, they display a shoulder that is significantly underpredicted by the calculations. This shoulder is evidence for a collective expansion of the system which will be discussed in more detail in section 4.5.

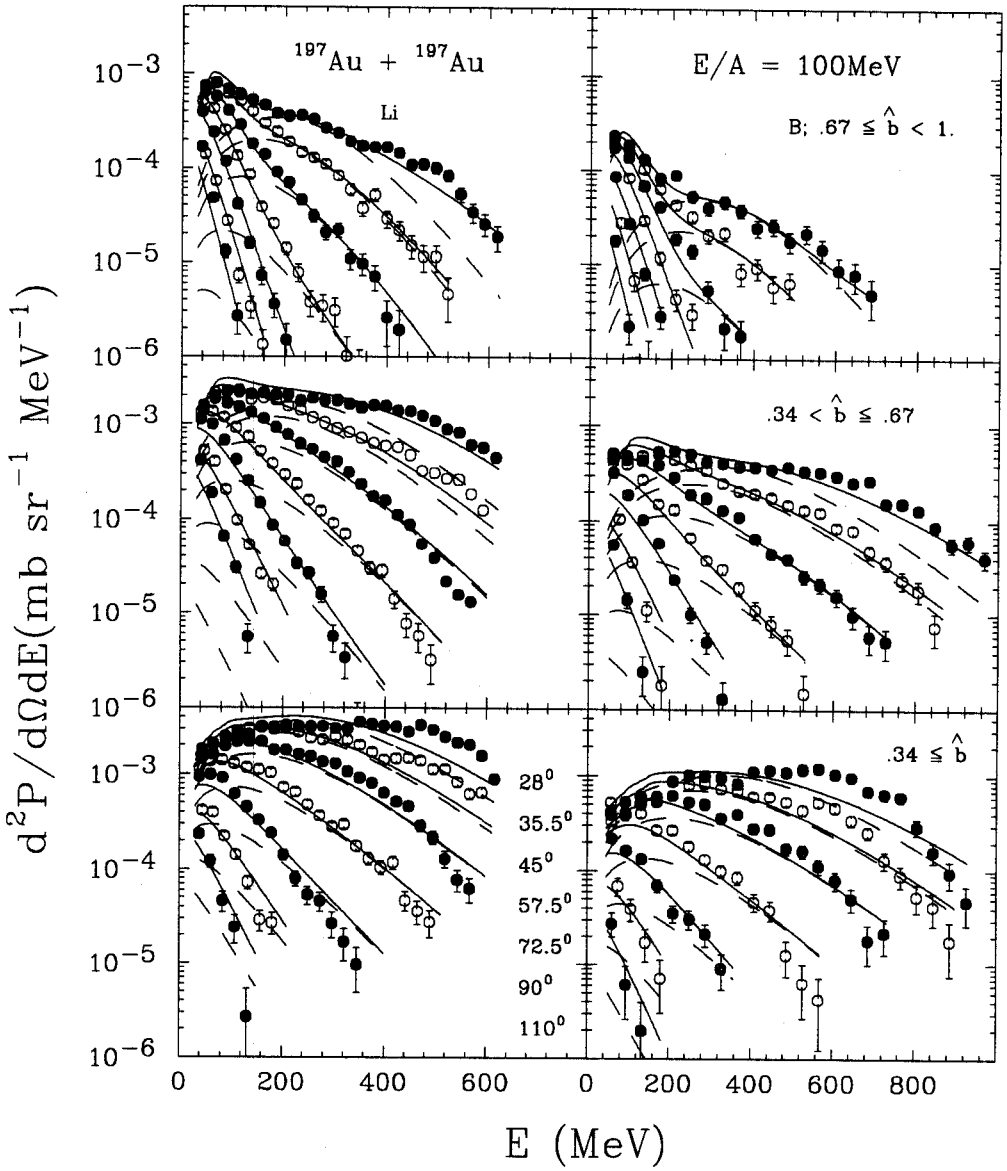

Figure 4.4.3 The energy spectra of Lithium and Boron emitted in the Au + Au collisions at E/A=100 MeV were plotted for θ_{lab}=28°, 35.5°, 45°, 57.5°, 72.5°, 90° and 110° for the peripheral (top panel), mid-central (middle panel) and central (bottom panel) collisions. The solid lines are the sum of contributions of three moving sources, and the dashed lines are the contributions from the participant source alone. The corresponding parameters are listed in Table 4.4.1.

Table 4.4.1 Parameters of three-source fits for the Lithium and Boron fragments at E/A=100 MeV and five-source fits for the Lithium and Beryllium fragments at E/A=400 MeV for different centralities listed in this table. (The units for a_i, T_i and V_i are MeV^{-3} sr^{-1}, MeV and MeV respectively.) Source 1 represents the participant source which moves with the velocity of the center of mass along the beam direction. Source 2 represents the decays of target-like and two projectile-like spectators which move with the v_x and v_z at the transverse and longitudinal directions in the center mass frame. Source 3 designates two sources with velocities midway between the center of mass and the spectator sources.

E/A	Z	$\hat{b}$	source	a_i	T_i	$v_{x,i}/c$	$v_{z,i}/c$	V_i	β_{exp}/c
100	Li	> .067	1	9.2E-11	31.9	0.	0.	22.1	-
			2	3.7E-10	20.6	.02	.155	9.12	-
	Li	.34-.67	1	3.5E-10	48.5	0.	0.	22.1	-
			2	5.9E-10	32.7	.02	.136	9.12	-
	Li	≤ .34	1	6.9E-10	58.7	0.	0.	22.1	-
			2	4.5E-10	29.6	.06	.132	9.12	-
100	B	> .067	1	6.6E-12	35.6	0.	0.	35.0	-
			2	5.2E-11	23.4	.02	.162	13.0	-
	B	.34-.67	1	3.6E-11	61.3	0.	0.	35.0	-
			2	7.6E-11	39.6	.02	.134	13.0	-
	B	≤ .34	1	9.1E-11	70.1	0.	0.	35.0	-
			2	6.5E-11	35.5	.06	.120	13.0	-
400	Li	> .067	1	5.8E-12	60.0	0.	0.	0.	.25
			2	1.2E-10	39.6	.03	.35	9.12	-
			3	2.5E-11	60.0	.015	.17	9.12	-
	Li	.43-.74	1	1.2E-10	60.0	0.	0.	0.	.25
			2	3.0E-10	53.4	.087	.35	9.12	-
			3	2.3E-11	60.0	.044	.17	9.12	-
	Li	≤ .34	1	6.8E-10	60.0	0.	0.	0.	.25
			2	2.2E-11	34.9	.15	.35	9.12	-
			3	2.2E-11	60.0	.08	.17	9.12	-
400	Be	> .067	1	1.8E-12	60.0	0.	0.	0.	.22
			2	3.9E-11	30.3	.06	.35	11.3	-
			3	1.7E-14	60.0	.03	.17	11.3	-
	Be	.43-.74	1	1.5E-11	60.0	.0	0.	0.	.25
			2	1.0E-10	49.1	.068	.35	11.3	-
			3	1.5E-13	60.0	.034	.17	11.3	-
	Be	≤ .34	1	7.9E-11	60.0	0.	0.	0.	.25
			2	3.1E-11	46.2	.10	.35	11.3	-
			3	3.3E-13	60.0	.05	.17	11.3	-

The energy spectra for Li and Be emitted in the Au + Au collisions at E/A = 400 MeV are shown in Figure 4.4.4 for three different reduced impact parameters. In contrast to those E/A = 100 MeV, the angular dependence of the energy spectra for peripheral and mid impact parameter collisions is weak; these spectra would overlap the most forward angles, 28°, 35.5° and 45°, if the energy spectra were not multiplied by factors of 8, 4, and 2 respectively. These overlapping spectra suggest a strong transverse source velocity. Such a hypothesis is explored below in conjunction with the triple differential cross section data. The solid and dashed lines are the best fits obtained with the spectators and participant component of a five moving model. Here, the source parameter involves a projectile- and target-like spectators source, a participant source moving with C.M. system and additional sources with velocities halfway between the participant and the spectator sources and a temperature sets equal to that of the participant source. For the participant source, a non-zero radial expansion velocity was assumed (see section 4.5), but it had no effect on the quality of the fits.

Triple Differential Cross Section of Emitted Fragment

To explore azimuthal angle dependence, the triple cross sections must be extracted. It requires determination of reaction plane for each event. Such reaction planes can be reconstructed with the transverse moment vector Q. [Dani 85] defined by :

$$\vec{Q} = \sum_i w_i \vec{P}_{\perp i}, \qquad (4.4.6)$$

with $w_i = +1$ (-1) for particles with rapidity $y > y_{cm}$ ($y < y_{cm}$). Only particles with well-calibrated energies were included in the reaction plane reconstruction, thus excluding particles emitted at $\theta_{lab} < 25°$. Since punch through particles did not have well-defined energies, they were also not included in the reaction plane reconstruction.

The component of the $\vec{Q}$ vector transverse to the beam axis is used to define the reaction plane, ϕ_R=0°. Due to a lack of statistics, only three broad azimuthal gates ($\phi = 0^0$-60^0, 60^0-120^0, 120^0-180^0) could be used to explore the triple differential cross-sections. The triple differential cross sections for the Lithium fragments, subject to a gate at the

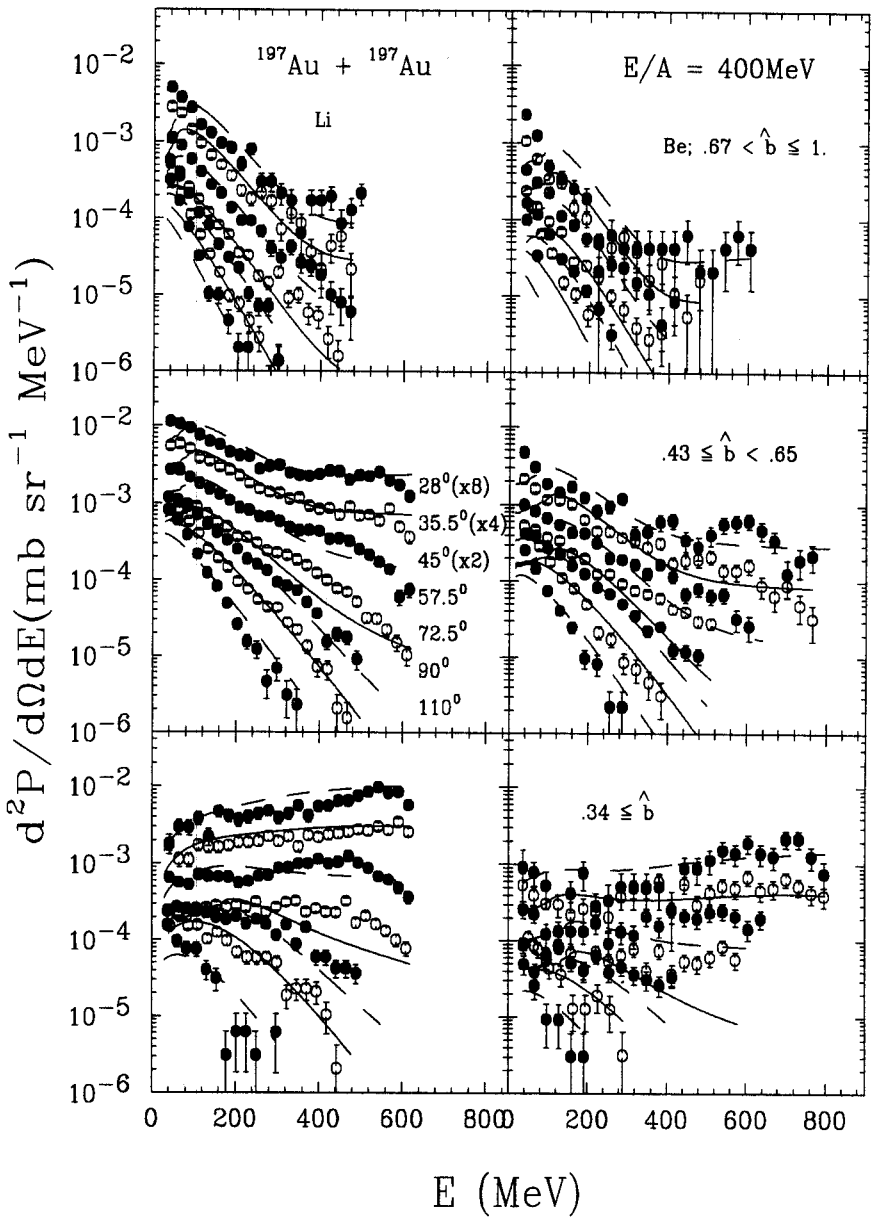

Figure 4.4.4 The energy spectra of Lithium and Beryllium fragments emitted in Au + Au collisions at E/A = 400 MeV. See the caption of Fig. 4.4.3 for details. The cross sections of θ_{lab}=28°, 35.5° and 45°are multiplied by factor of 8, 4, and 2 respectively. The corresponding parameters are listed in Table 4.4.1.

mid-impact parameters which brackets the maximum in the fragment multiplicity at E/A = 400 MeV, are plotted in Figure 4.4.5. Since the number of IMFs is small at $\theta_{lab} > 100^{\circ}$, the triple differential cross sections are only plotted for first six rings of the Miniball array. A strong enhancement of the differential cross-sections at $\phi = 120^0$-180^0 is observed. This enhancement increases with the particle energy and polar angle. This observation is consistent with a significant transverse flow [Gutb 89 a&b, Stöc 82, Bert 87, Kämp 93].

The corresponding parameters for the fits are listed in the table 4.4.2. The lines present the contributions from the target-like spectator. The triple differential cross sections for fragments with Z = 3, 4 and 5 can be reasonably well described by assuming that the target-like spectator has significant transverse velocity 0.08-0.05 and a temperature around 40-50 MeV (as listed in table 4.4.2). The heavier fragments move with a smaller transverse velocities, consistent with the trend displayed by the mean transverse energies as shown in the Fig. 4.4.1. The trends are shown in Fig. 4.4.5b. Recent analyses suggest that the spectra of heavier fragments emitted for this impact parameter range are relatively insensitive to incident energy, consistent with the assumption of limiting fragmentation. Also, show the temperature parameter for heavier fragments $7 < Z < 20$ extracted for Au + Pb collision at E/A = 600 MeV [Lind 93]. This comparison indicates that the lighter fragments are indeed more sensitive than the heavier fragments to the dynamics of the initial energy deposition to the spectator residue.

The corresponding triple differential cross sections for Lithium fragments emitted in central E/A = 100 MeV collisions are plotted in Fig. 4.4.6. The lines represent the sum of contributions of the three sources. The emission is relatively isotropic with respect to the azimuthal direction around the mid rapidity. The anisotropy of the emission patterns around the projectile and target rapidity at these collisions is much smaller than that observed at E/A = 400 MeV. The corresponding parameters of these triple differential cross section fits using the three source model are listed in the table 4.4.2.

Fig. 4.4.7 shows some of sensitivities of the fitting procedure to the transverse velocity of the spectator sources. The solid points in Fig 4.4.7 are obtained by allowing the longitudinal velocity and the temperature of spectator sources to be free fit

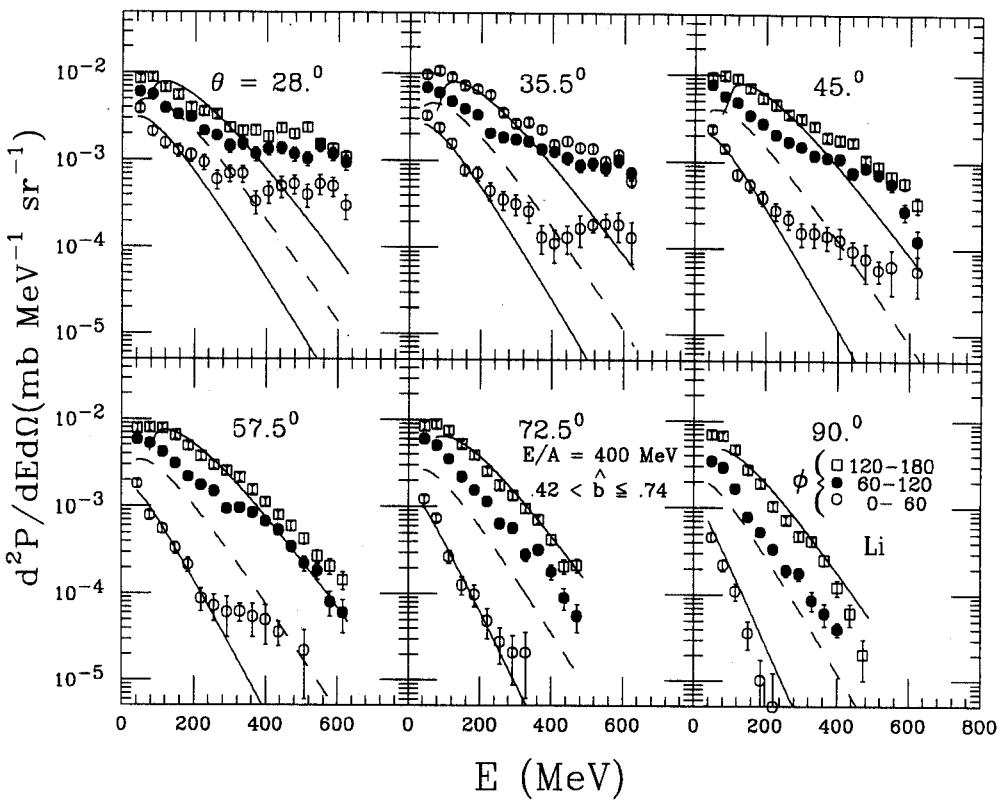

Figure 4.4.5 The triple differential cross sections of Lithium fragments emitted with the impact parameters $.42<\hat{b} \leq .74$ for Au + Au collisions at E/A = 400 MeV. Each panel represents the triple differential cross sections at each polar angle as indicated. The lines are the contributions of the target-like spectator.

Table 4.4.2 Parameters of moving-source fits to the triple differential cross sections for Lithium, Beryllium and Boron fragments at E/A= 400 and Lithium fragments at 100 MeV collisions. The units for a_i, T_i and V_i are Mev^{-3} sr^{-1}, MeV and MeV respectively.

E/A	b	Z	s	a_i	T_i	$v_{x,i}/c$	$v_{z,i}/c$	V_i	β_{exp}/c
400	.42-.74	Li	1	7.2E-11	60.	0.	0.	0.	.25
			2	6.6E-10	53.4	.087	0.35	9.2	0.
			3	5.2E-11	60.	.044	0.17	9.2	0
400	.42-.74	Be	1	2.8E-11	60.	0.	0.	0.	.25
			2	1.4E-10	49.1	.068	0.35	11.	0.
			3	4.0E-12	60.	.034	0.17	11.	0
400	.42-.74	B	1	1.0E-11	60.	0.	0.	0.	.25
			2	9.4E-11	44.1	.054	.35	13.	0
			3	4.6E-12	60.	.027	.17	13.	0.
100	.34	Li	1	6.3E-09	14.7	0.	0.	0.	.199
			2	2.8E-10	46.7	.6	.12	9.2	0.

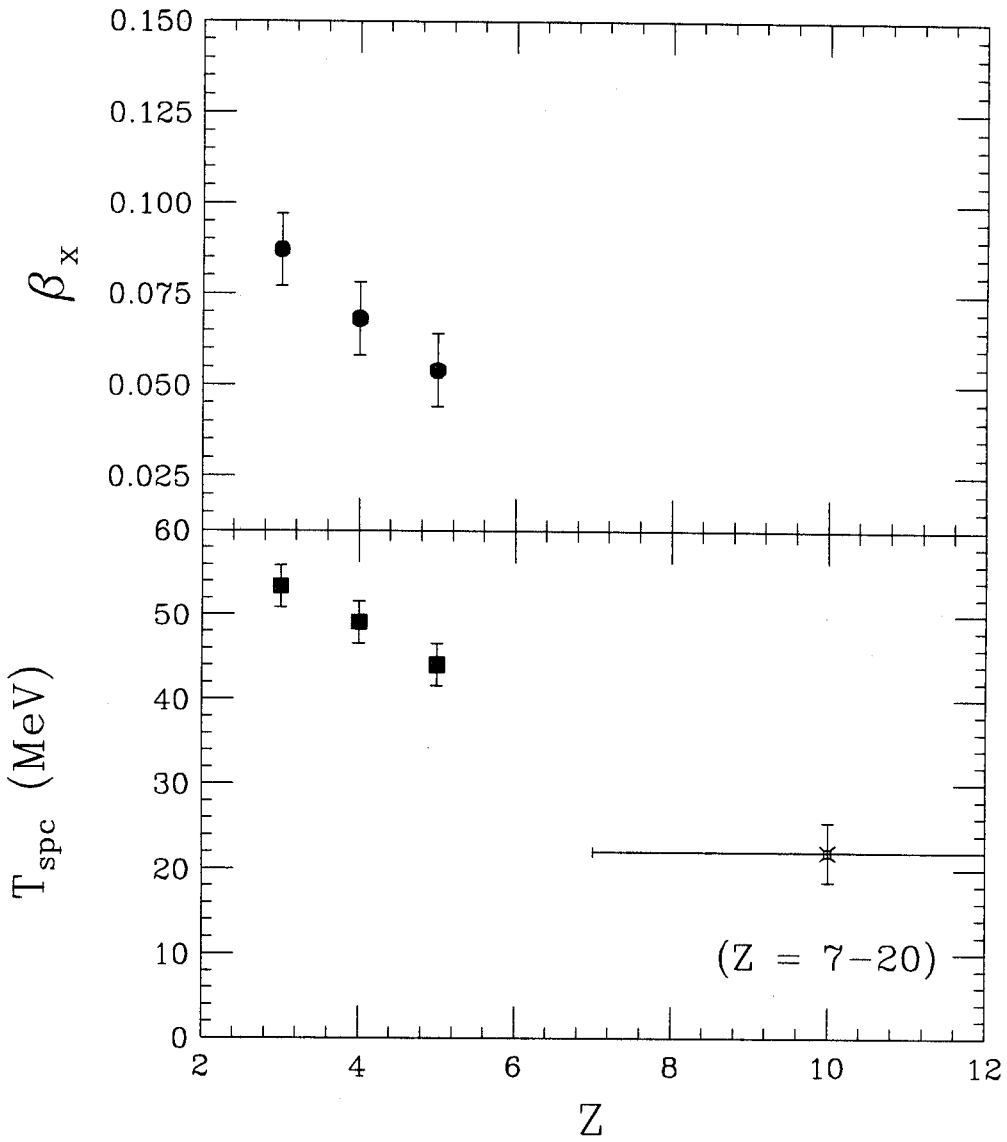

Figure 4.4.5b The transverse velocities of spectator source is obtained by fitting the triple differential cross sections of fragments emitted with the impact parameters $.42<\hat{b} \leq .74$ for Au + Au collisions at E/A = 400 MeV. The temperature of the spectators is plotted at bottom panel with the temperature of spectator extracted for the heavier fragments (Z=7-20) from the Au + Pb collisions at E/A = 600 MeV.

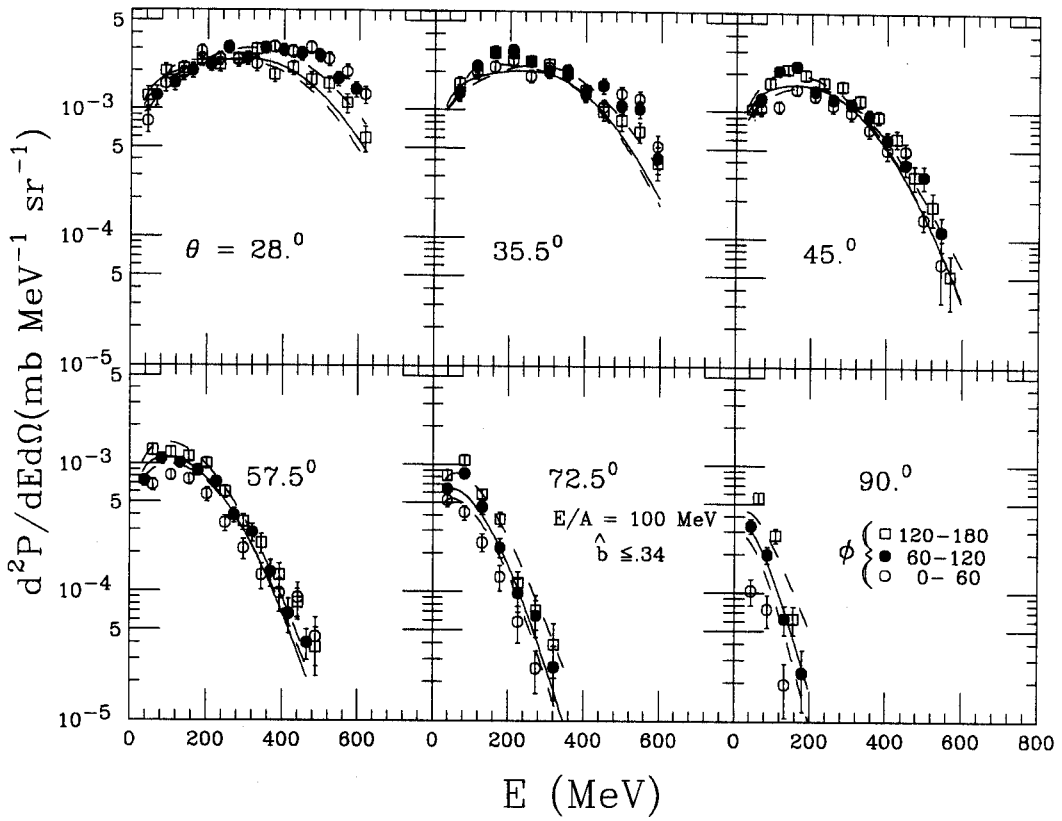

Figure 4.4.6 The triple differential cross sections of Lithium emitted at central collision of Au on Au collisions at E/A = 100 MeV. Each panel represents the triple differential cross sections at each polar angle as indicated. The lines were the sum of the contributions from three-moving-source model.

parameters. The open circles are obtained by fitting with constant longitudinal velocity and the open squares with a constant spectator temperature $T_{sp.}$ Here is a clear tradeoff between T_{spc} and the transverse velocity β_x of the spectator source that is shown in the middle panels of the Figure 4.4.7. Best fits for the Lithium and Boron fragments in central collisions at E/A = 100 MeV are obtained by assuming that spectator moves with a transverse velocity of about 0.06 c. With the range in β_x explored here, there is a very little change in the parameters of the participant source. Thus the radial expansion of the participant source described in Section 4.5 is not influenced by including the transverse velocity of the spectator sources.

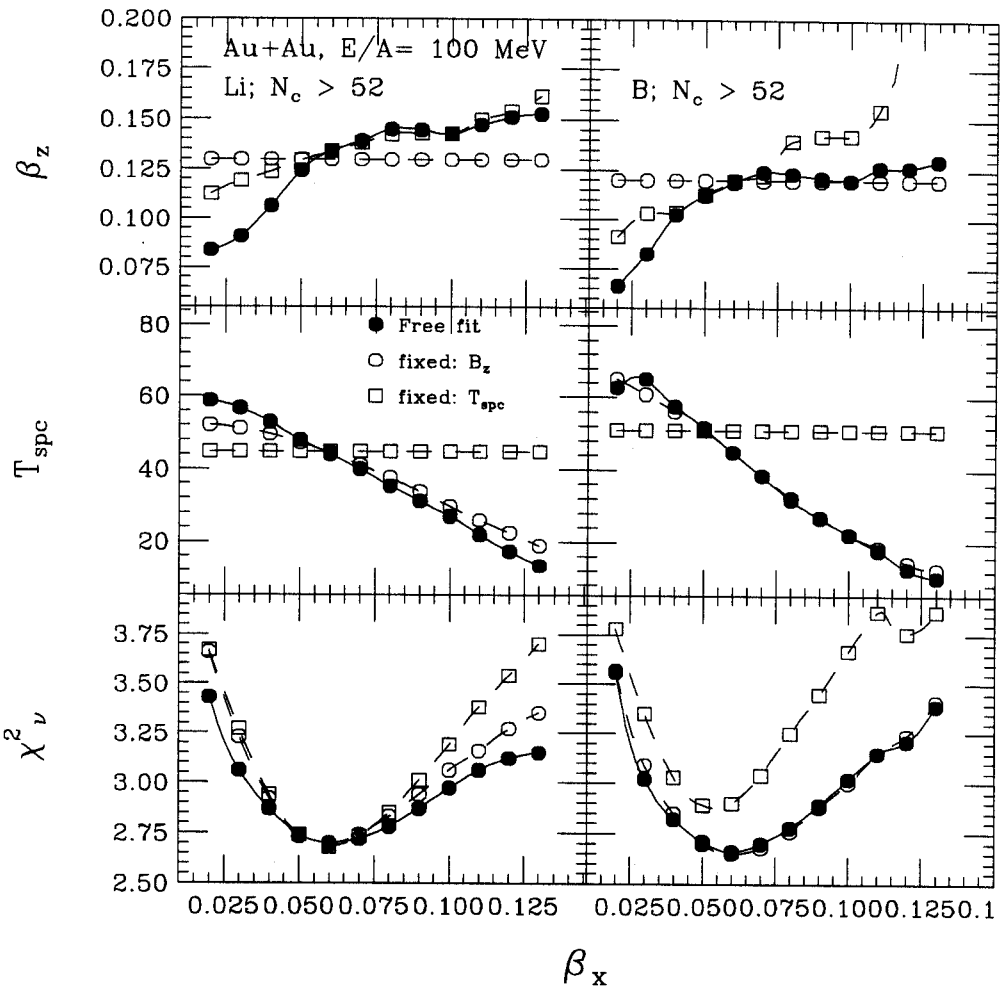

Figure 4.4.7 The temperature T_{spc} and the longitudinal velocity β_z of the fit for the triple cross sections of Lithium and Boron fragments at the central E/A = 100 MeV collisions, shown as a function of the transverse velocity β_x.

4.5 Collective Expansion in Central Collisions at E/A = 100 and 250 MeV

At E/A ≥ 100 MeV, dynamical models [Peil 89, Peil 92, Boal 88] predict that fragment multiplicities are strongly influenced by a rapid expansion from supranormal densities achieved early in the nuclear collision [Peil 89, Peil 92, Bond 94]. Experimental evidence now suggests a significant collective "radial" expansion [Jeon 94, Barz 91, Baur 93, deSo 93, Hsi 94]. This collective expansion may persist even to lower incident energies where transverse directed flow [Gutb 89 a&b, Gutb 90, Leif 93] vanishes [Ogil 90, West 93] due to cancellations between the attractive and repulsive deflections that result from the mean field attraction and nucleon-nucleon collisions, respectively. Like measurements of directed transverse flow [Gutb 89 a&b, Gutb 90, Leif 93], measurements of radial flow [Jeon 94, deSo 93, Hsi 94] can provide unique constraints on nuclear transport properties such as the in-medium nucleon- nucleon cross section [Dani 92].

Radial flow effects should be enhanced for central collisions [Dani 92]; therefore a gate on the reduced impact parameter, $\hat{b} = b/b_{max} \leq 0.33$ was imposed in the data analysis discussed in this section. If the contribution from radial flow are large, one would expect this to be manifested in the energy spectra of the emitted fragments. The solid lines in the upper panel in Fig. 4.5.1 indicate the best fits to the energy spectra for B^{11} fragments at E/A = 100 MeV, assuming three relativistic Maxwellian distributions [Laud 80], as described in Section 4.4. Contributions from the participant source (dashed lines) dominate fits at the forward angles $\theta_{lab} = 35.5°$ and 45°. The projectile- and target-like spectator sources contribute strongly at the backward angles and for very high energies at forward angles, but not at $28° \leq \theta_{lab} \leq 57.5°$ for 400 MeV $\leq E_{lab} \leq$ 700 MeV, where the shapes of the measured spectra are very poorly described by these thermal source fits. Similar difficulties are encountered for the energy spectra of other IMFs with $2 \leq Z_f \leq 6$, as shown in the left panels of Fig. 4.5.2. The corresponding parameters of these fits without radial expansion are given in Table 4.5.1 (type I) for all of the fragments. These temperatures are higher than expected from systematics of asymmetrical systems. From such systematics, one expects a temperature of about 16 MeV [Jack 83, Chen 88, Gelb 87], consistent with a Fermi gas system with thermal energy E/A ≈ 25 MeV, comparable

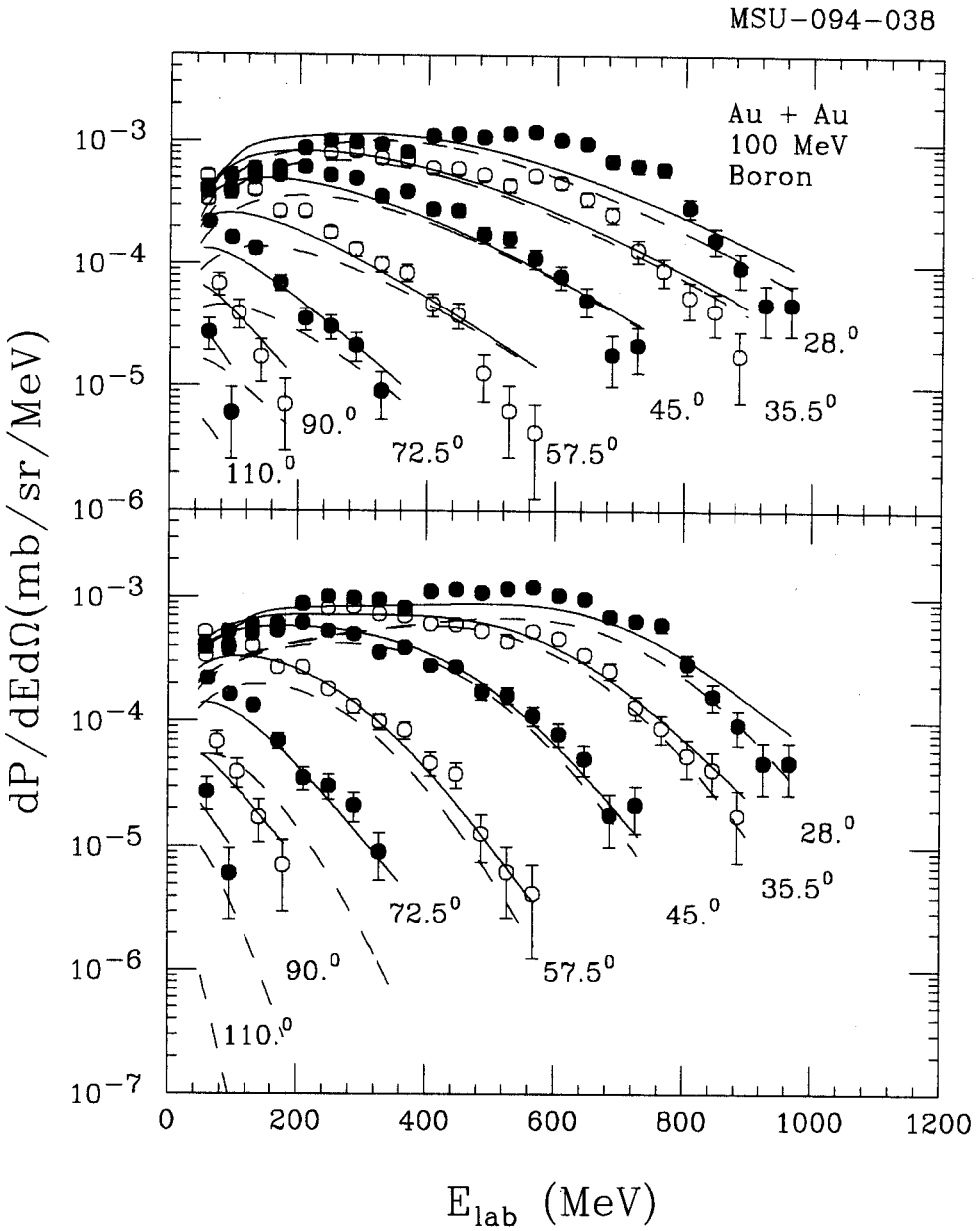

Figure 4.5.1 Comparisons of the energy spectra for Boron fragments emitted to θ_{lab} = 28.0°, 35.5°, 45.0°, 57.5°, 72.5°, 90.° and 110.° (solid and open points), with corresponding moving source fits. Upper panel: The solid lines correspond to the fits obtained with Eq. 4.4.2 and no radial expansion. Lower panel: The solid lines correspond to fits obtained with Eq. 4.4.2 and 4.4.5, incorporating a radial expansion. The dashed lines in both panels correspond to the respective contributions from the participant sources only.

Table 4.5.1 Parameters of three-moving-source fits for fragments with Z = 2 to 6 in central collisions at E/A=100 MeV. (Fits 1 and 2 are without and with expansion, respectively, and the units for a_i, T_i and V_i are MeV^{-3} sr^{-1}, MeV and MeV respectively.) The source 1 represents the participant source which moves with the velocity of center mass along the beam direction. The source 2 represents the target-like or projectile-like spectator sources which move with velocities v_x and v_z in the transverse and longitudinal directions in the center of mass frame. The Coulomb energies of the emitted fragments were estimated and added to the fragment energies without changing the direction of the emitted fragments.

Z	fit	source	a_i	T_i	$v_{x,i}/c$	$v_{y,i}/c$	V_i	β_{exp}/c
He	1	1	1.2E-08	37.4	0.	0.	15.1	0.
		2	1.0E-08	12.76	.06	.167	6.6	0
	2	1	2.4E-08	23.5	0.	0.	0.	.129
		2	1.1E-08	14.3	.06	.159	6.6	0.
Li	1	1	6.9E-10	58.7	0.	0.	22.1	0.
		2	4.5E-10	29.6	.06	.132	9.12	0.
	2	1	4.3E-09	17.6	0.	0.	0.	.178
		2	5.6E-10	27.6	.06	.131	9.21	0.
Be	1	1	1.1E-10	73.9	0.	0.	28.6	0.
		2	1.0E-10	45.8	.06	.107	11.3	0
	2	1	1.5E-09	13.9	0.	0.	0.	.172
		2	8.3E-11	46.6	.06	.117	11.3	0.
B	1	1	9.1E-11	70.1	0.	0.	35.0	0.
		2	6.5E-11	35.5	.06	.120	13.0	0.
	2	1	8.9E-10	16.6	0.	0.	0.	.153
		2	5.8E-11	35.3	.06	.120	13.0	0.
C	1	1	4.0E-11	64.6	0.	0.	41.2	0.
		2	7.1E-10	39.1	.06	.096	14.1	0.
	2	1	5.5E-10	12.8	0.	0.	0.	.144
		2	6.6E-11	37.9	.06	.099	14.2	0

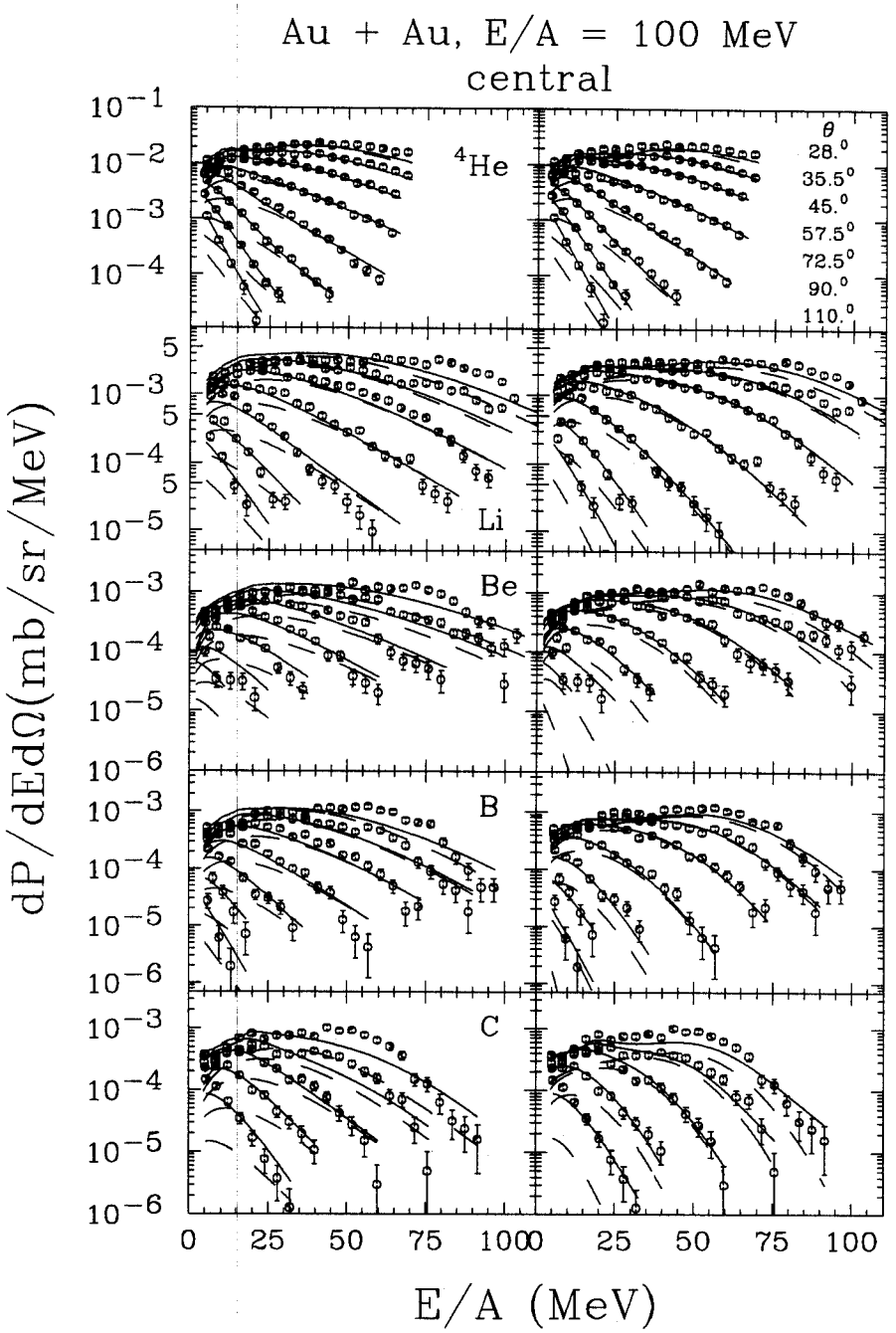

Figure 4.5.2 Comparisons of the energy spectra for fragments with Z =2 to 6. (See Fig. 4.5.1.) Left panels: The solid lines correspond to fits obtained with Eq. 4.4.2 and no radial expansion. Right panels: the solid lines correspond to fits obtained with Eq. 4.4.2 and 4.4.5, incorporating a radial expansion. The dashed lines in both panels correspond to the respective contributions from the participant sources only.

to the total kinetic energy per nucleon in the c.m. system. This discrepancy suggests that there is a significant enhancement in the apparent temperature due to some form of collective motion.

As discussed in Section 4.4, the triple differential cross sections for the central collisions at E/A = 100 MeV show that contributions from the directed transverse collective flow are negligible at mid-rapidity. Instead, transport model calculations predict the existence of a radial expansion at breakup. To explore this idea within a moving source parameterization, a self similar radial expansion, $\vec{v}_i(\vec{r}) = c\beta_{exp}\vec{r} / R_s$, of a spherical participant source (i = 1 in Eq. 4.4.2) was assumed which attains its maximum velocity $c\beta_{exp}$ at the surface $r = R_s$. The velocities of the individual particles were assumed to be thermally distributed with temperature T_i about the local radial expansion velocity. Coulomb expansion after breakup was modeled in the limit of large β_{exp}, i.e., particles with charge Z_f, emitted from a source with charge Z_s, were assumed to gain a kinetic energy

$$\Delta E_{Coul}(r) = Z_f(Z_s - Z_f)e^2r^2 / R_s^3 \qquad (4.4.4)$$

without changing direction. In the CM frame, one obtains

$$\frac{dP_1}{dEd\Omega} = \frac{3}{4\pi R_s^3}\int_0^{R_s} r^2 dr \int d\Omega_r \int dE'$$

$$\times \frac{dP_1}{dE' d\Omega}(\vec{p}', \vec{v}(\vec{r}), 0) \times \delta(E' - E + \Delta E_{Coul}(r)) \qquad (4.4.5)$$

The total energy spectrum is obtained by inserting Eq. 4.4.5 into Eq. 4.4.2 as the participant source.

The best fits, assuming $Z_s = 118$ and $R_s = 11.1$ fm for Boron fragments, are shown by the solid lines in the lower panel of Fig. 4.5.1; the inclusion of collective expansion changes the curvatures of the calculations so as to accurately follow the curvatures of the energy spectra at $28° \le \theta_{lab} \le 57.5°$, where the participant source dominates. Similar curvatures of the energy spectra for fragments Z = 2 to 6 are shown in the right panels of Fig. 4.5.2.

The extracted value for the expansion velocity β_{exp} depends on the temperature T_{mid}, the total charge and size of the participant source. Setting $R_S = 11.1$ fm and $Z_S = 118$, the sensitivity of the expansion velocity to the temperature of the mid-rapidity source (T_{mid}) is shown in Fig. 4.5.3. Here the radial expansion velocity and the chi squares (χ^2_v) of the fits are plotted as a functions of T_{mid} for Li and B fragments. A minimum chi square around $T_{mid} = 15$-18 MeV is observed. Throughout this minimum, the radial expansion velocities of the participant source decrease with increasing T_{mid}, as shown in the top panel of the Figure 4.5.3. The extracted values of β_{exp} are not very sensitive to the temperature of the participant source, changing by about ± 10% for 5 MeV ≤ T_1 ≤ 20 MeV, where reasonable fits were obtained. For $T_{mid} > 30$ MeV for which fits dictate a smaller radial expansion velocity, the curvatures of the energy spectra were not well described.

Both β_{exp} and Coulomb expansion dynamics have a similar influence on the energy spectra. The source size can be related to the breakup density by $\rho_B \sim \rho_0 \bullet (7.4 \text{ fm}/R_S)^3$, where ρ_0 is the normal nuclear matter density. Here, 7.4 fm is the radius of the participant source with $Z_S = 118$ at normal nuclear matter density. In this estimation, a charge of $Z_{spec} = 20$ is assumed to be taken away by each spectator residue. Figure 4.5.4. shows the dependence of the T_{mid} and β_{exp} on the ρ_B / ρ_0. For a fixed $T_{mid} = 15$ MeV, the β_{exp} and T_{mid} values obtained from the fit are shown by the solid circles in the bottom and middle panels of Fig. 4.5.4 respectively. The corresponding χ^2_v values are shown in the top panel. Since smaller contributions from the Coulomb energy to the energy spectra occur at smaller ρ_B / ρ_0, and can be partly compensated by requiring larger contributions from the collective energy, these is the monotonically decreasing β_{exp} dependence on ρ_B / ρ_0 as shown in the bottom panel of Fig. 4.5.4. There is no clear χ^2_v minimum in the density dependence. Similar conclusions are obtained by allowing both the density parameter and the temperature of the source in the fits to vary freely, fits as indicated by the open points in the figures. Over the range $0.1 \le \rho_B / \rho_0 \le 0.3$, there is a ± 5% change in the best value of β_{exp}. Energy spectra alone do not provide sufficient information to determine the breakup

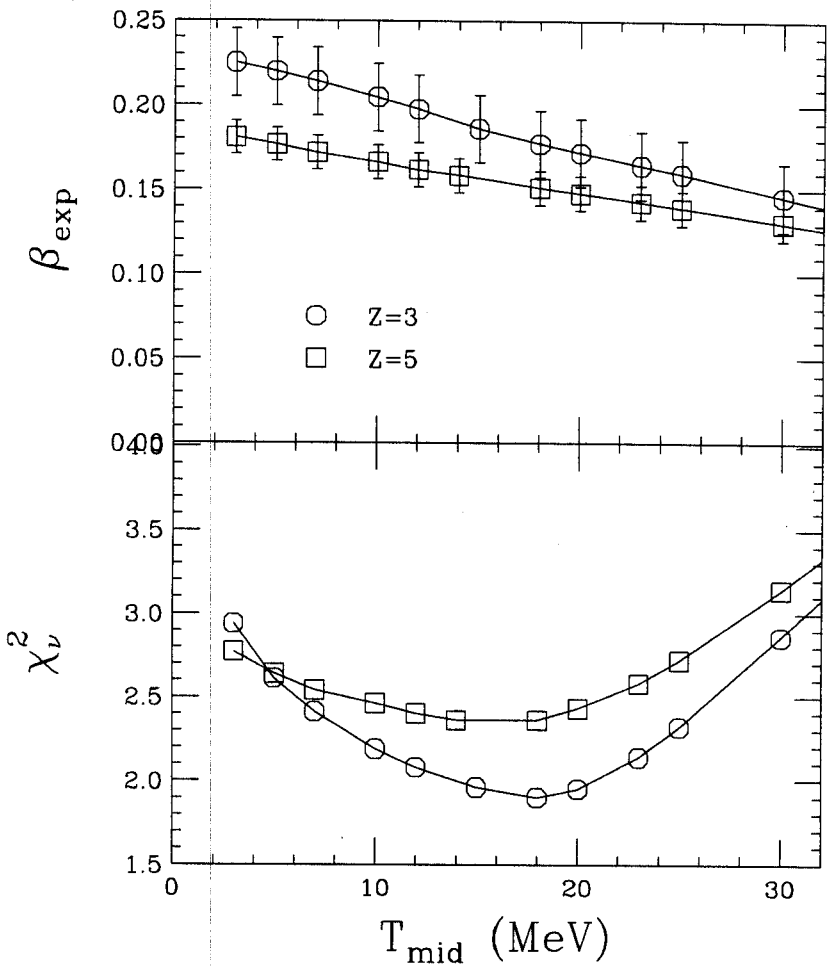

Figure 4.5.3 The relation between the chi square χ^2_ν from fitting the energy spectra and the temperature of the participant source is plotted at the bottom panel for Lithium and Boron fragments. The corresponding relationship between T_{mid} and the radial expansion velocity of the participant source is shown in the top panel.

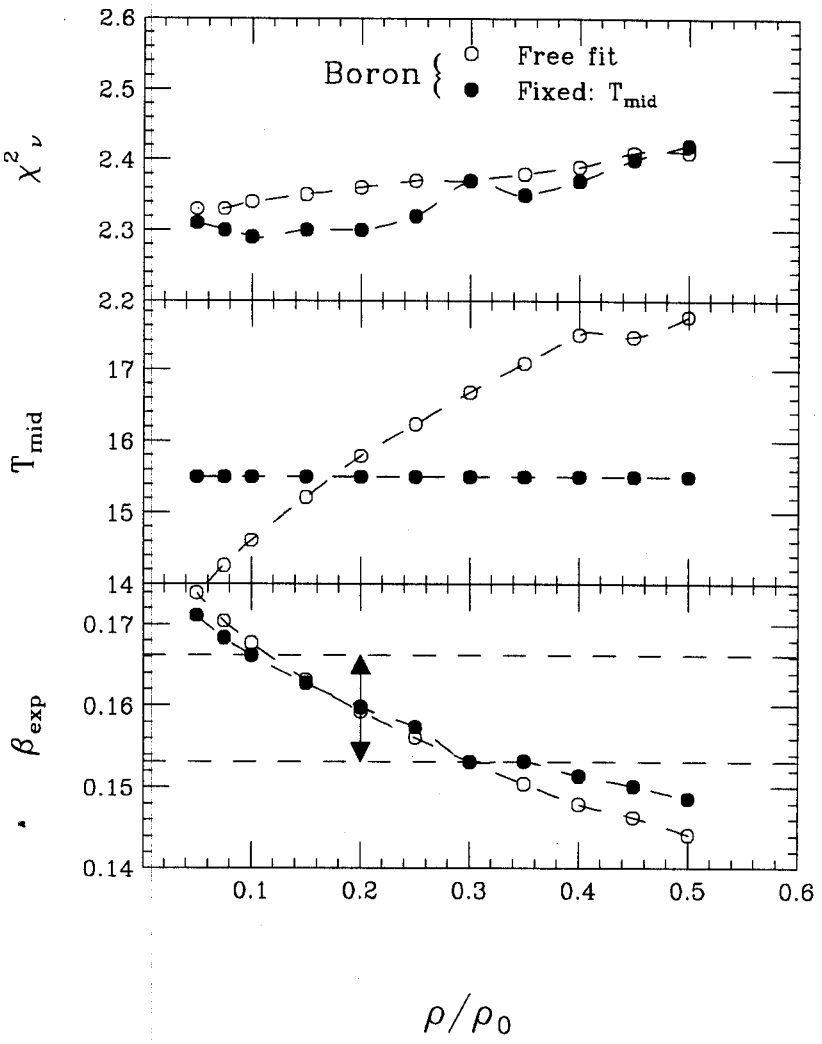

Figure 4.5.4 Best fit values for the radial velocity are plotted at the bottom panel as a function of the assumed breakup density of the participant source. The solid points are the best fit values for a fixed temperature of the participant source and the open points are the best fit values allowing the temperature of the participant source vary as a free parameter. The best values of the radial velocity vary by about 5% as the density values from ρ_0 = 0.3 to ρ_0 = 0.1 of normal density. χ^2_ν values from the fits and the participant temperature T_{mid} are plotted in the top and middle panels respectively.

density. Additional information such as fragment-fragment correlation functions may be needed [Kim 89, Kämp 93].

When the fitting procedure described above is applied to other fragments, similar values of β_{exp} for the different Z_f's are extracted (left panel, Fig. 4.5.5) for fixed T_{mid} = 15 MeV (solid points), as when T_{mid} is varied freely (open points). However, there is a systematic decrease of β_{exp} with Z_f, suggesting that heavier fragments may not participate as fully as the lighter fragments in the collective expansion. Such an effect could arise if heavier fragments originated from the more dense central regions of the expanding system. Values for β_{exp} are not significantly changed by making a more restrictive gate, $\hat{b} < 0.16$, on the impact parameter.

Radial Expansion for the Central Collisions at E/A = 100 MeV

Since β_{exp} and the Coulomb expansion have a similar influence on emitted fragments in the fitting, the mean total radial collective energy, defined by

$$< E_r >= \frac{3}{5}\left[\frac{1}{2}mc^2\beta_{exp}^2 + Z_f(Z_s - Z_f)e^2 / R_s\right] \qquad (4.5.1)$$

is considerably less sensitive to ρ_B . The values for $< E_r >$ are shown as solid points in the right panel of Figure 4.5.5. Here, $< E_r >$ increases with mass (charge) but not linearly as expected for a uniform participation of these fragments in the radial expansion. The radial energies for heavier fragments with $Z_f \geq 5$ increase less than one would expect if a linear dependence were followed.

To further support these conclusions, the energy spectra in the total CM frame at $\theta_{c.m.} = 90^0$ are shown in Fig. 4.5.6 for Z_f = 2-6. The total fit and participant source contributions are represented by the solid and dashed lines, respectively. Assuming a temperature T_{mid} = 15 MeV, the mean radial collective energy was independently estimated by integrating these spectra and then subtracting the mean thermal kinetic energy of a Maxwell gas, i.e.

$$< E_r >=< E > -\frac{3}{2}T_{mid} \qquad (4.5.2)$$

These estimates for $< E_r >$ (open squares, right panel of Fig. 4.5.5) are somewhat smaller than the fitted values for the participant source (solid points), reflecting additional low energy spectral contributions from the spectator sources. Differences between the solid and open points provide indications of the systematic uncertainties in extracting mean radial kinetic energies for the only participant source.

Energy spectra for IMFs produced in central Au on Au collisions at E/A=100 MeV indicate large radial collective expansion velocities at breakup. The radial expansion energies, E_r/A = 8.3-13.5 MeV, decrease with the fragment charge, but are relatively insensitive to assumptions about the density of the system at breakup and the contributions from the transverse flow or from the breakup of projectile and target spectator matter.

Radial Expansion for the Central Collisions at E/A=250 MeV

Center of mass energy spectra at $\theta_{c.m.} = 90°$ are shown in Figure 4.5.7. Due to the lack of statistics in this data set, comprehensive analyses similar to that at E/A = 100 MeV could not be performed. The three-moving-source model was used to fit these energy spectra for Z = 2 to 4 (due to the lack of statistics for the higher charges). As shown in Table 4.5.2, fits to the center of mass energy spectra at 90° do not unambiguously choose the participant temperature and the values for T_{mid} (best fit) vary widely with Z. The extracted β_{exp} are listed in Table 4.5.2 for the best fit and for a fixed participant source temperature of T_{mid} = 30 MeV, assuming $\rho/\rho = 0.3$. The values of radial expansion energies E_r/A for the fits assuming T_{mid} = 30 MeV also given.

To better estimate the temperature of participant source, the mean center of mass energy, $<E_{c.m.}>$ is plotted in open squares in Fig. 4.5.8 at $\theta_{c.m.} = 90°$ energy spectra for E/A=250. For comparison, the corresponding data at E/A = 100 MeV is plotted as the open circles as well. Assuming the thermal energies of the detected fragments are charge independent and that the radial energies are proportional to the mass of fragments, a linear fit to the data for Z = 2-4 at E/A = 250 MeV was obtained, consistent with a thermal energy of 45 MeV, corresponding to a temperature of 30 MeV. The extracted temperature is close to the systematic of Refs. [Chit 83] and [Gelb 88]. Using T_{mid} = 30 MeV, the values of E_r/A have been obtained. These values are given in the last column in

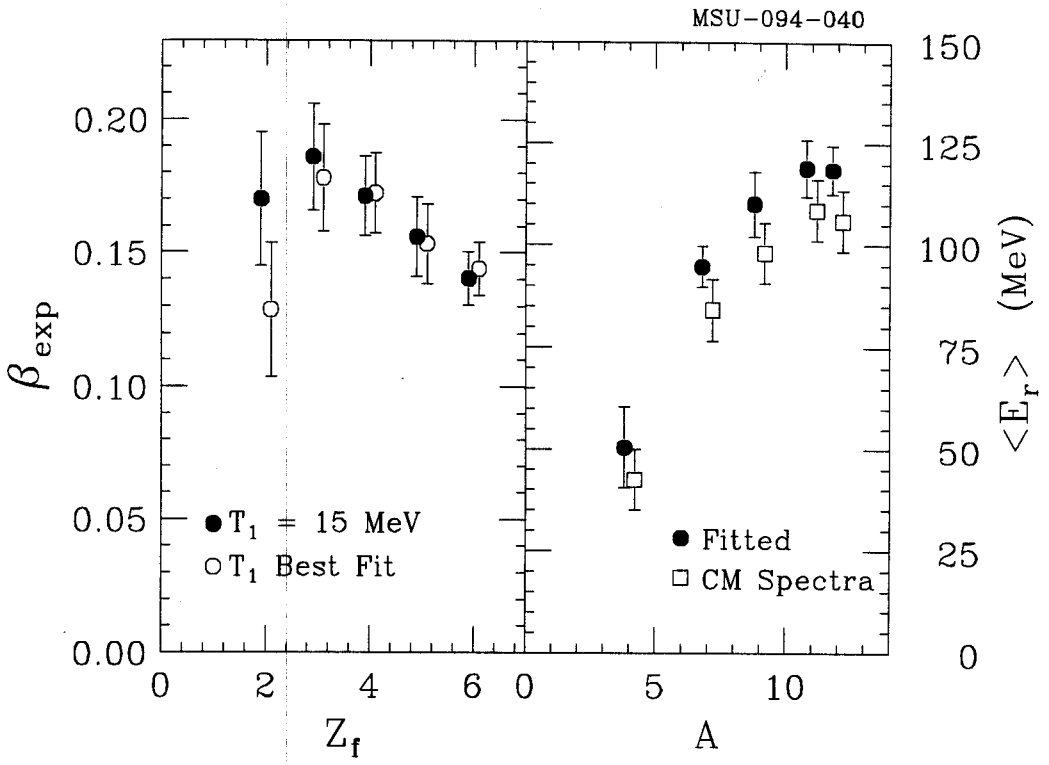

Figure 4.5.5 Left panel: The open points correspond to the best fit values for the radial expansion velocities as a function of the fragment charge. The solid points are the corresponding values obtained when T_{mid} is constrained to be 15 MeV. Right panel: The solid points depict the dependence on the fragment mass of the mean radial collective energy $<E_r>$ extracted from the fits upon the fragment mass. The open squares depict the corresponding values extracted from the energy spectra of the center mass frame at 90^0, assuming T_{mid} = 15 MeV. Both values are plotted at the mass of the most abundant natural isotope.

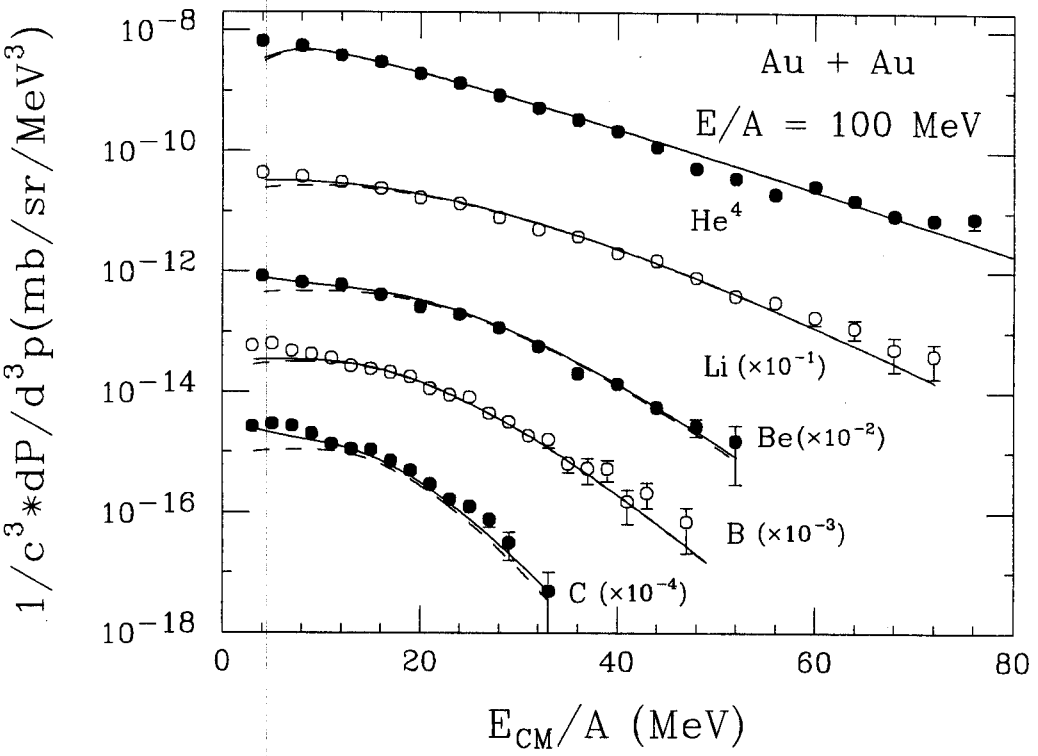

Figure 4.5.6 Energy spectra in the center of mass frame for various fragments detected at $80° \leq \theta_{cm} \leq 110°$ in the central collisions at E/A = 100 MeV. The solid lines correspond to the three source fit, assuming a radial expansion. The dashed lines depict the participant source alone.

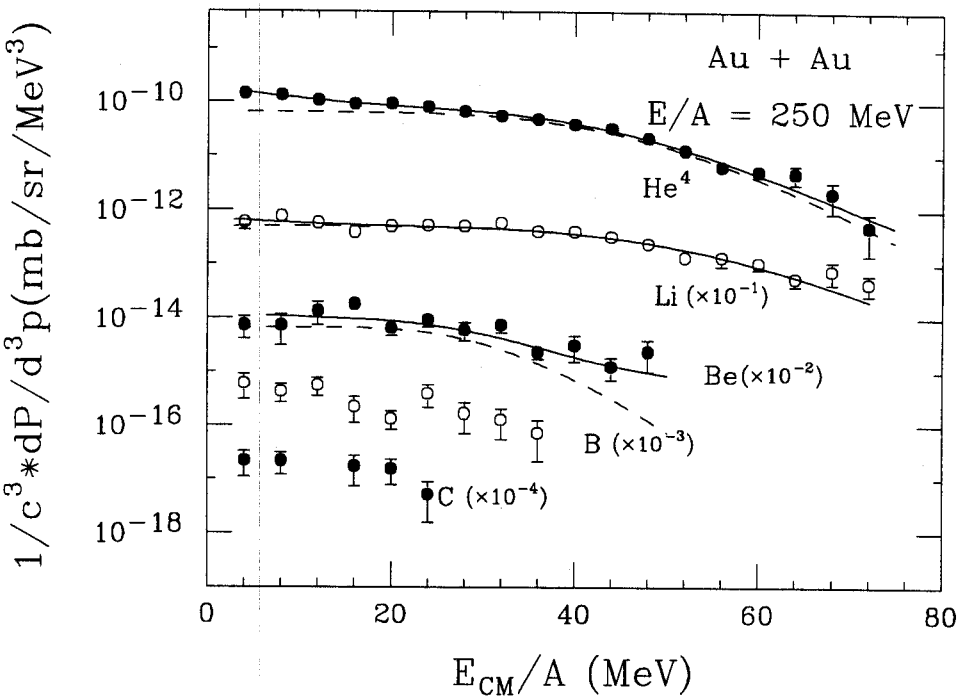

Figure 4.5.7 Energy spectra are plotted in the center of mass frame for various fragments detected at $80° \leq \theta_{cm} \leq 110°$ in central E/A = 250 MeV collisions. The solid lines correspond to the three source fit, assuming a radial expansion. The dashed lines depict the participant source alone.

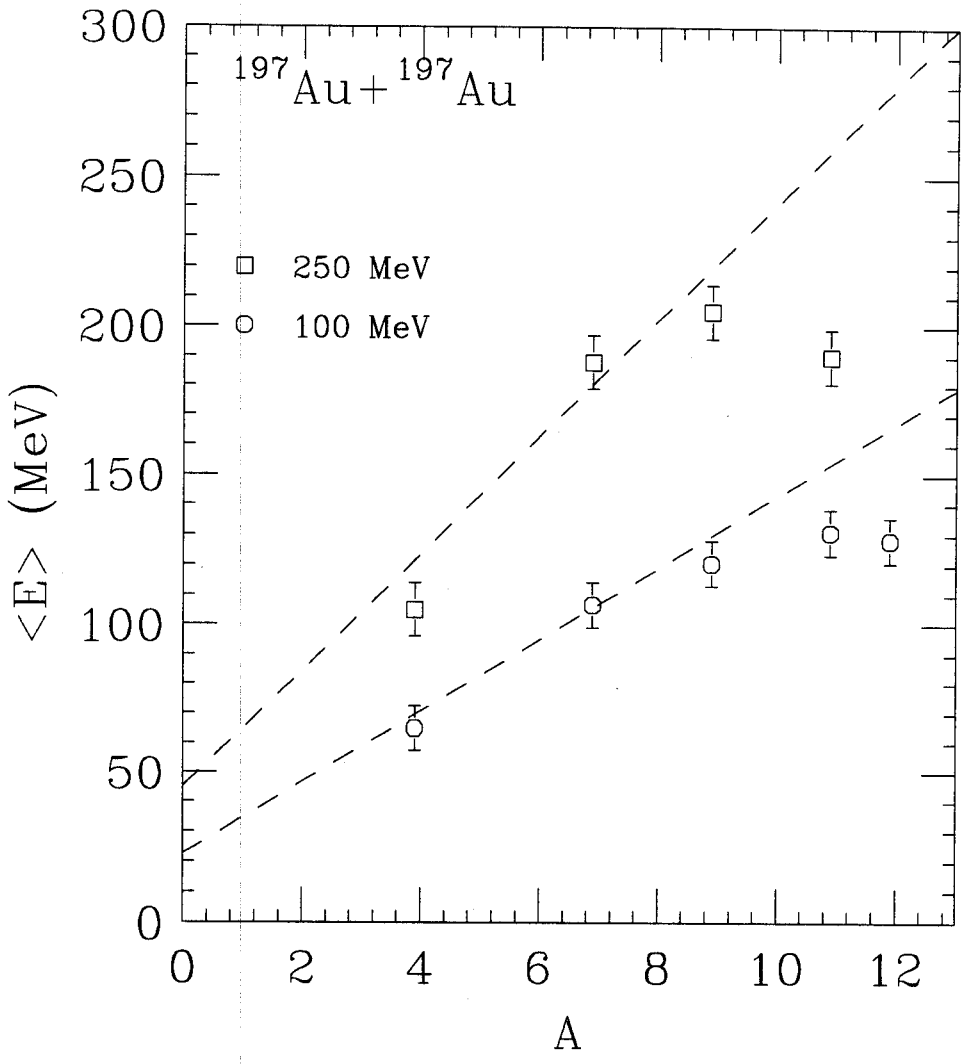

Figure 4.5.8 Measured mean energies are plotted as a function of the fragment mass at $80° \leq \theta_{cm} \leq 110°$ of the incident energies E/A=100 and 250 MeV. The dashed lines indicate linear fits of the mean energies.

Table 4.5.2. Very much same method was applied at E/A = 100 MeV to obtain the open squares in right panel of Fig. 4.5.5. Here, we fit the three lightest charges to obtained the thermal energy 22.5 MeV is corresponding to a temperature 15 MeV, and the radial energies consistent with our previous extraction of radial energies.

Table 4.5.2 The parameter of fits for the central collisions of $\theta_{c.m.} = 90°$ energy spectra at E/A=250 MeV.

Z	T_{mid}(best fit) MeV	β_{exp} (best fit)	β_{exp} (T_{mid}=30 MeV)	E_r fits (T_{mid}=30 MeV)	E_r spectrum (T_{mid}=30MeV)
^{4}He	6.2	.267	.190	59	60
^{7}Li	13.9	.267	.254	153	143
^{9}Be	18.7	.195	.187	126	157

The collective radial energies of Lithium and Boron fragments extracted in the present work at E/A = 100 and 250 MeV are plotted in Figure 4.5.9. For reference, we also show data points measured at E/A = 150 MeV [Jeon 94] with the GSI 4π phase I detectors. In the analysis at E/A = 150 MeV, energy spectra at $\theta_{c.m.} \approx 45°$ were measured and compared to the statistical model, FREESCO, to estimate the thermal, Coulomb and collective radial energy contributions to the mean fragment kinetic energy. The lower limits of bars at E/A = 150 MeV are obtained by subtracting Coulomb and thermal contributions out of the mean kinetic energy. The upper limits of bars include Coulomb energy by assuming the temperature of system equal 20 MeV.

Recently, multifragment disintegrations have also been measured for central ^{197}Au + ^{197}Au collisions at E/A = 35 MeV. These fragments are found to be emitted predominantly at the low center of mass energies, about E/A ~ 5 MeV, consistent with a Coulomb dominated breakup of a single source [Dago 93]. When the latter measurements are placed into global content, it is clear that onset of radial expansion occurs at incident

energies somewhere between E/A = 35 and 100 MeV. At E/A ≥ 100 MeV, the extracted collective energy appears to be approximately one third to one half of the incident kinetic energy per nucleon in the CM frame. This reduces the available excitation energy for thermal motion.

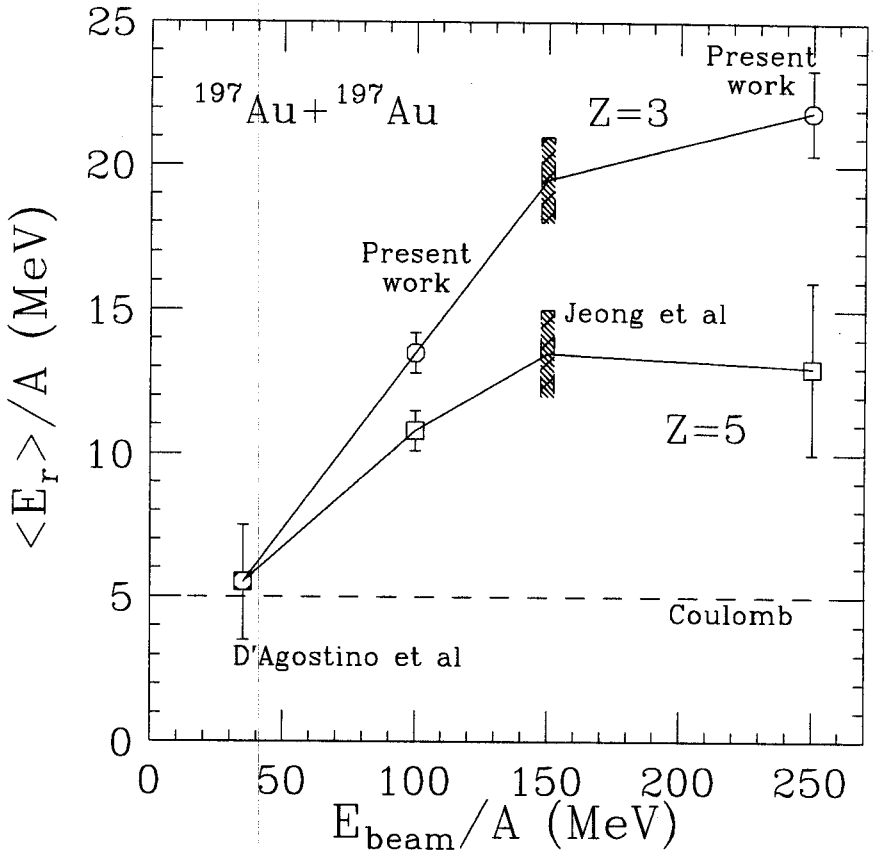

Figure 4.5.9 Mean radial energies per nucleon for Lithium and Boron fragments are plotted as a function of incident energy.

Chapter 5

Summary

Multifragmentation has been measured for $^{197}Au + ^{197}Au$ collisions at E/A = 100, 250 and 400 MeV collisions. The mean fragment multiplicity increases monotonically with the charged particle multiplicity at E/A = 100 MeV. For central collisions at E/A = 100 MeV, an average number of nearly 10 intermediate mass fragments is detected, about 50 % larger than the largest fragment multiplicities in the Ar + Au and Xe + Au reactions [Bowm 91, Phai 92]. The mean number of IMF multiplicities are reduced to less than 2 for central collisions at E/A = 400 MeV before any correction for detection efficiency, and the peak IMF multiplicity is shifted to the larger impact parameters. To perform quantitative corrections for the experimental detection efficiencies, the experimental distributions in rapidity-momentum phase space were simulated and the symmetry of the system was exploited to extrapolate to the poorly measured regions of the phase space. After correction for the efficiency, the mean number of IMFs increases to about 3 for the central collisions and about 8.5 at the peak IMF multiplicity. This further confirms the observations of nuclear vaporization in central Au + Au collisions.

Microscopic dynamical models generally underestimate fragment yields and predict an incorrect impact parameter dependence for IMF multiplicity at the highest incident energy. The description of peripheral collisions at E/A = 400 MeV can be improved by including statistical decay, via the SMM or EES models of the bound residues produced at $b \geq 4$ fm in the molecular dynamics simulations. At the same time, however, the number of IMFs are significantly reduced in the central collisions at E/A = 100 MeV by the decay of excited fragments within the SMM model. Thus, fragments are either produced in insufficient quantities or are too highly excited to survive the statistical decay in quantities consistent with experimental observations.

Both the fragment mean transverse energies and the kinetic energy spectra are strongly dependent on the mass of fragments, indicating a significant collective motion within the fragmenting system. In central collisions at E/A = 100 MeV, this motion is largely radial; in mid-central collisions at E/A = 400 MeV, there are significant transverse collective velocities. To extract a quantitative value for the radial collective expansion velocity at E/A = 100 MeV, moving-sources analyses were performed. These analyses are consistent with the radial expansion energies per nucleon of E/A at 8.3-13.5 MeV, about one-third to one-half of the incident kinetic energy per nucleon. The radial energies of the emitted fragments decrease with the fragment charge, but are relatively insensitive to the assumptions about the density of the system at breakup. Similar results are obtained from the averages of the fragment energy spectra at E/A = 150 [Jeon 94] and 250 MeV. At both E/A = 100 and 250 MeV, the radial expansion energies decrease with the charge of fragment, suggesting that all fragments do not equally participant in the collective expansion. The transverse energies per nucleon of the emitted fragments from the breakup of projectile and target spectator matters also decrease with the fragment charge in mid-central E/A = 400 MeV collisions. Both these transverse energies and the triple differential cross sections indicate the heavier fragments leave the system at the later stages in the multifragment breakup.

Despite the significant findings in this dissertation, many of the principal objectives of investigating multifragmentation have not been achieved. There is still no definitive determination of the thermodynamic parameters relevant to the liquid-gas phase transition. These prospects still lie ahead. The principal achievements of this work are the delineation of the initial conditions where the mixed phase final states relevant to this bulk phase transition may be achieved. Many current and future investigations are, and will be, focused upon the interpretation of multifragment decays in central collisions at incident energies less than 100A MeV, where this process is fully developed and the prospects for future investigations are very exciting.

List of References

[Aich 88] J. Aichelin et al., Phys. Rev. **C37**, 2451 (1988).

[Alar 86] J.Alarja et al., Nucl. Inst.and Meth. **A242**, 352 (1986).

[Alar 92] J. P. Alard et al, Phys. Rev. Lett. **69**, 889 (1992).

[Aldi 89] The ALADIN collaboration, Nachrichten GSI 02-89 of GSI at Darmstadt Germany 1988 (Unpublished).

[Bade 82] A. Baden et al., Nucl. Inst. and Meth. **A203**, 189 (1982).

[Batk 92] G. Batko et al., Nucl. Phys. **A536**, 786 (1992).

[Barz 91] H.W. Barz et al., Nucl. Phys. **A531**, 453 (1991).

[Baue 85] W. Bauer et al., Phys. Lett. **B150**, 53 (1985).

[Baue 93] W. Bauer et al., Phys. Rev. **C47**, R1838 (1993).

[Baug 93] E. Bauge et al., Phys. Rev. Lett. **70**, 3705 (1993).

[Bauh 85] W. Bauhoff et al., Phys. Rev. **C32**, 1915 (1985).

[Bere 92] M. Berenguer et al., J. Phys. **G18**, 655 (1992).

[Bert 83] G. Bertsch and P. J. Siemens, Phys. Lett. **B126**, 9 (1983).

[Bert 87] G.F. Bertsch et al., Phys. Lettt. **B189**, 384 (1987).

[Birk 64] J.B. Birks, *The theory and Practice of Scintillation counting,* P.2 (Pergamon Press, New York, 1964).

[Blum 91] Y. Blumenfeld et al., Phys. Rev. Lett. **66**, 576 (1991).

[Boal 83] D.H. Boal, Phys. Rev. **C28**, 2568 (1983).

[Boal 88a] D.H. Boal and J. N. Glosli, Phys. Rev **C37**, 91(1988).

[Boal 88b] D.H. Boal and J.N. Glosli, Phys. Rev. **C38**, 1870 (1988).

[Boal 90] D.H. Boal and James N. Glosli, Phys. Rev **C42**, R502 (1990).

[Bogo 62] N. N. Bogoliubov, *Studies in Stastical Mechanics*, J. de Boer and G.E. Uhlenbeck Eds., **Vol. 1** (North-Holland, Amsterdam 1962). The BBGKY stands for Bogoliubov-Born-Green-Kirkwood-Yvon.

[Bond 82] J.P. Bondorf et al., Nucl. Phys. **A387**, 25c (1981).

[Bond 85a] J.P. Bondorf et al., Nucl. Phys. **A444**, 321 (1985).

[Bond 85b] J.P. Bondorf et al., Nucl. Phys. **A444**, 460 (1985).

[Bond 94] J.P. Bondorf et al., Phys. Rev. Lett. **73**, 628 (1994).

[Bord 93] B. Borderie et al., Phys. Lett. **B302**, 15 (1993).

[Botv 87] A.S. Botvina et al., Nucl. Phys. **A475,** 663 (1987).

[Botv 90] A.S. Botvina et al., Nucl. Phys. **A507,** 649 (1990).

[Botv 93] A.S. Botvina et al., Z. Phys. **A345,** 297 (1993).

[Boug 87] R. Bougault et al., Phys. Rev. **C36**, 830 (1987).

[Boug 89] R. Bougault et al., Proceeding of the Symposium on Nuclear Dynamics and Nuclear Disassembly, P.193 (1989).

[Bowm 91] D.R. Bowman et al., Phys. Rev. Lett. **67**, 1527 (1991).

[Bowm 92] D.R. Bowman et al., Phys. Rev. **C46**, 1834 (1992).

[Bowm 93] D.R. Bowman et al., Phys. Rev. Lett. **70**, 3534 (1993).

[Buja 85] A. Bujak, et. al., Phys. Rev. **C32**, 620 (1985).

[Cava 90] C. Cavata et al., Phys. Rev. **C42**, 1760 (1990).

[Cebr 90] D. Cebra et al., Phys. Rev. Lett. **64**, 2246, (1990).

[Chen 88] Z. Chen and C.K. Gelbke, Phys. Rev. **C38**, 2630 (1988).

[Chit 83] C. B. Chitwood et al., Phys. Lett. **B131**, 289 (1983).

[Chit 86] C.B. Chitwood et al., Phys. Rev. **C34**, 858 (1986).

[Colo 92] N. Colonna et al., Nucl. Inst. and Meth. **A321**, 529 (1992).

[Cser 86] L. P. Csernai and Kapusta, Phys. Rep. **131**, 223 (1986), and references therein.

[Cuss 85] Y. Cusson et al., Phys. Rev. Lett. **55**, 2786 (1985).

[Dani 85] P. Danielewicz and G. Odynice, Phys. Lett. **B157**, 146 (1985).

[Dani 88] P. Danielewicz et al., Phys. Rev. **C38**, 120 (1988).

[Dani 91] P. Danielewicz and G.F. Bertsch, Nucl. Phys. **A553**,712 (1991).

[Dani 92] Pawel Danielewicz and Qiubao Pan, Phys. Rev. **C46**, 2004 (1992).

[deSo 90] R.T. De Souza et al., Nucl. Instr. and Meth. **A295**, 109 (1990).

[deSo 91] R. T. de Souza et al., Phys. Lett. **B268**, 6 (1991).

[deSo 93] R.T. De Souza et al., Phys. Lett. **B300**, 29 (1993).

[Dors 88] C. Dorso and J. Randrup, Phys. Lett. **B215**, 611 (1988).

[Doss 85] K.G.R. Doss et al., Phys. Rev. **C32**, 116 (1985).

[Doss 87] K.G.R. Doss, et al., Phys. Rev. Lett. **59**, 2720 (1987).

[Fai 82] G. Fai and J. Randrup, J. Nucl. Phys. **A381**, 557 (1982).

[Feld 90] H. Feldmeier et al., Nucl. Phys. **A515**, 147 (1990).

[Finn 82] J.E. Finn, et al., Phys. Rev. Lett. **49**,1321 (1982).

[Fox 93] D. Fox et al., Phys. Rev. **C47**, R421 (1993).

[Frie 83a] W.A. Friedman and W.G. Lynch, Phys. Rev. **C28**, 16 (1983).

[Frie 83b] W.A. Friedman and W.G. Lynch, Phys. Rev. **C28**, 950 (1983).

[Frie 90] W.A. Friedman et al., Phys. Rev. **C42**, 667(1990).

[Gelb 87] C.K. Gelbke and D. H. Boal, Prog. in Part. and Nucl. Phys **19**, 33 (1987).

[Gobb 93] A. Gobb et al., Nucl. Inst. and Meth. **A324**, 156 (1993).

[Gong 88] W.G. Gong et al., Nucl. Inst. and Meth. **A268**, 352 (1988).

[Goul 69] F.S. Goulding and D.A. Landis, "Recent Advances in Particle Identifier at Berkeley," in *Semiconductor Nuclear-Particle Detectors and Circuits*, Publication 1593, National Academy of Sciences, Washington, DC, P 757 (1969).

[Gros 82] D.H.E. Gross et al., Z. Phys. **A309**, 41 (1982).

[Gros 86] D.H.E. Gross et al., Phys. Rev. Lett. **56**, 1544 (1986).

[Gros 90] D.H.E. Gross et al., Rep. Prog. Phys. **53**, 605 (1990), and Refs therein.

[Gutb 89a] H.H. Gutbrod et al., Rep. Prog. Phys. **52**, 1267 (1989).

[Gutb 89b] H.H. Gutbrod et al., Phys. Lett. **B216**, 267 (1989).

[Gutb 90] H.H. Gutbrod et al., Phys. Rev. **C42**, 640 (1990).

[Gust 88] H. Å Gustafsson et al., Modern Physics Letter A, Vol. **3**, No. **14**, 1323 (1988).

[Haus 52] W. Hauseer and H. Feshbech, Phys. Rev. **87**, 366 (1952).

[Hirs 84] A.S. Hirsch, et al., Phys. Rev. **C29**, 508 (1984).

[Hori 91] Hisashi Horiuchi, Nucl. Phys. **A522**, 257 (1991).

[Hsi 94] W. C. Hsi et al., Phys. Rev. Lett. **73**, 3367 (1994).

[Hube 91] J. Hubele et al., Z. Phys. **A340**, 263 (1991).

[Hube 92] J. Hubele et al., Phys. Rev. **C46**, R1577 (1992).

[Huan 63] Kerson Hunag, *Statistical Mechanics*, p69, John Wiley & Sons Inc, 1963.

[Jeon 94] S.G. Jeong et al., Phys. Rev Lett. **72**, 3468 (1994).

[Kämp 93] B. Kämpfer et al., Phys. Rev. **C48**, R995 (1993).

[Kean 94] D. Keane et al., Preprint LBL-36370, September 1994.

[Kim 89] Y.D. Kim et al., Phys. Rev. Lett. **63**, 494 (1989).

[Kim 91] Y.D. Kim, PhD Thesis, Michigan State University, 1991.

[Kim 92] Y.D. Kim et al., Phys. Rev. **C45**, 338 (1992).

[Knol 79] Glenn F. Knoll, Chapter 10, *Radiation Detection and Measurement*, John Wiley & Son Inc.(1979).

[Koch 91] V. Koch et al., Nucl. Phys. **A532**, 317 (1991).

[Kund 94] G.J. Kunde PhD thesis, Unversity Frankfort 1994.

[Kund 95] G.J. Kunde et al., Phys. Rev. Lett. **74**, 38 (1995).

[Land 80] L.D. Landau and E.M. Lifshitz, *Statistical Physics* (Pegammon Press, New York, 1980), 3rd ed..

[Leif 93] Y. Leifels et al., Phys. Rev. Lett. **71**, 963 (1993).

[Lenn 31] J.E. Lennard-Jones, Proc. Cambridge Phi. Soc. **27**, 469 (1931).

[Lind 93] V. Lindenstruth, GSI report, **GSI-93-18**, May, 1993.

[Lync 87] W. Lynch, Ann. Rev. Nucl. Part. Sci., **37**, 494 (1987), and references therein.

[Lync 92] Williams G. Lynch, Nucl. Phys. **A545**, 199c (1992).

[Mari 70] Jerry B. Marion, *Classical Dynamics,* p220 (Academic Press Inc. 1970).

[Mekj 77] A.Z. Mekjian, Phys. Rev. Lett. **38**, 640 (1977).

[More 75] L.G. Moretto, Nucl. Phys. **A247**, 211 (1975).

[Morr 78] D.J. Morrissey et al., Phys. Rev. **C18**, 1267 (1987).

[Müll 95] W.F.J Müller, J. Pochodzalla and W. Trautmann for ALADIN/LAND collaboration, GSI 03-95 (1995).

[Myer 82] W.D. Myers and W.J. Swiatecki, Ann. Rev. Nucl. Part. Sci. **32**, 309 (1982).

[Nord 28] L.W. Nordheim, Proc. Roy. Soc. **A49**, 689 (1928).

[Ogil 91] C.A. Ogilvie, et al., Phys. Rev. Lett. **67**, 1214 (1991).

[Peas 94] G.F. Peaslee et al., Phys. Rev. **C49**, R2271 (1994).

[Peil 89] G. Peilert et al., Phys. Rev. **C39**, 1402 (1989) and refrences therein.

[Peil 92] G. Peilert et al., Phys. Rev. **C46**, 1457 (1992).

[Phai 92] L. Phair et al., Nucl. Phys. **A548**, 489 (1992).

[Phai 93] L. Phair et al., Nucl. Phys. **A564**, 453 (1993)

[Pres 86] Williams H. Press, Brain P. Flannery, Saul A. Teukolsky and William T. Vttterling; Numerical Recipes The Art of Scientific Computing, Cambridge University Press 1989.

[Quin 59] A.R. Quinton et al., Phys. Rev. **115**, 886 (1959).

[Raci 95] G. Raciti; The full range of particle identification for the Catania hodoscope are achieved with the parameters of PID defined as $\log(DE) + .1*\log(E)^2 - .65*\log(E)$; DE is measured QDC channel from the Silicon and the E is the measured QDC channel from the CsI. A 2-D spectra with the PID and the log(E) are used to set the charged particle identification gates. The energy deposited into the Silicon were calibrated by a polynomial fit. The energy deposited in CsI were done by a power law approximation fit.

[Rand 81] J. Ranfrup and S.E. Koonin, Nucl. Phys. **A356**, 223 (1981).

[Sang 92] T. C. Sangster et al., Phys. Rev. **C46**, 1404 (1991).

[Schw 93] C. Schwarz et al., p.248, NSCL/MSU Annual Report 1993.

[Siem 79] Philip J. Siemens and Joseph I. Kapusta, Phys. Rev. Lett. **43**, 1486 (1979).

[Siem 83] P.J. Siemens, Nature **305**, 410 (1983).

[Slat 75] John. C. Slater, *Solid-State and Molecular Theory: A Scientific Biography*, P92-95, Wiley-Intersience Publication 1975.

[Stöc 80] H. Stöcker, J. Maruhn and W. Greiner, Phys. Rev. Lett. **44**, 725

(1980).

[Stöc 86] H. Stöcker and W. Greiner, Phys. Rep. **137**, 279(1986), and references therein.

[Stor 58] R.S. Storey et al., Proceedings of the Phys. Society **72**, 1 (1958).

[Troc 89] R. Trockel et al., Phys. Rev. **C39**, 729, 1989.

[Tsan 91] M.B. Tsang et al., Phys. Rev. **C44**, 2065 (1991).

[Tsan 93a] M.B. Tsang et al., Phys. Rev. **C47**, 2717 (1993).

[Tsan 93b] M. B. Tsang et al., Phys. Rev. Lett. **71**, 1502 (1993)

[Uehl 33] E.A. Uehling and G.E. Uhlenbeck, Phys. Rev. **43**, 552 (1933).

[Vrie 87] H. de Vries et al., Atomic data nd Nuclear data table **36**, 495 (1987).

[West 85] G. D. Westfall et al., Nucl. Inst. and Meth. **A238**, 347(1985).

[Wils 92] W.K. Wilson et al., Phys. Rev. **C45**, 738 (1992).

[Wang 95] S. Wang et al., Phys. Rev. Lett. **74**, 2646 (1995).

[Waps 77] A. H. Wapstra and K. Bos, Nucl. Data table **19**, 175; **20**, 1 (1977).

[Weis 37] V.F. Weisskopf, Phys. Rev. **52**, 295 (1937).

[Zhu 92] F. Zhu et al., Phys. lett. **B282**, 299 (1992).